Polyoxometalate Related Redox Flow Batteries

by

Jee Jay Chen

A dissertation submitted in partial fulfillment
of the requirements for the degree of
Doctor of Philosophy
(Chemical Engineering)
in The University of Michigan
2017

Doctoral Committee:

Professor Mark A. Barteau, Chair
Professor Mark Banaszak Holl
Professor Johannes Schwank
Professor Levi T. Thompson

Jee Jay James Chen

jjchenum@umich.edu

ORCID iD: 0000-0001-5191-314X

Dedication

To my parents, my family, and my girlfriend.

Acknowledgements

I would like to thank my advisor and mentor Prof. Mark A. Barteau for his kind support, patience, and mentorship. During these five years, I have grown a lot under the kind guidance of Prof. Barteau. I would also like to thank Prof. Thompson; Prof. Thompson has treated me like his own group member with his kind suggestions and advice. I would also like to extend my appreciation to the other members in my dissertation committee - Prof. Johannes Schwank and Mark Banaszak Holl - for their continued support.

I must also express my gratitude to both the Barteau research group and Thompson research group, for I am very lucky to have the chance to work with both groups. Specifically, I would like to thank Dr. Trent Silbaugh, Dr. Krista Hawthorne, Professor Emeritus Paul Rasmussen, Dr. Saemin Choi, Dr. Jason Siegel, Dr. Yuan Chen, Dr. Brian Wyvratt, Dr. Xingyi Yang, Dr. Shawn Eady, Dr. Jonathan Kucharyson, Dr. Abdul Djire, Dr. Tapiwa Mushove, Dr. Siu On Tung, Trenton Wilke, Xiaowen Zhao, Sydney Fisher, Winn Wen, Sarah Carl, Scott Johnson, Yixuan Chen and all other friends for all of their support.

There are too many people to list out whom I would like to thank since I could not have been able to finish my Ph.D. degree without their help and mental support.

Lastly, a few words of gratitude and appreciation to my family and my longtime girlfriend, Ariel Wang, for their 24 hours and 365 days support. Thank you all and I love you.

Table of Contents

List of Figures

List of Tables

List of Abbreviations

ACN	Acetonitrile
AEM	Anion Exchange Membrane
ANF	Aramid Nanofiber
BE	Bulk Electrolysis
CD	Charge/Discharge
CE	Coulombic Efficiency
CV	Cyclic Voltammetry
CEM	Cation Exchange Membrane
DMC	Dimethyl Carbonate
DMSO	Dimethyl Sulfoxide
EIS	Electrochemical Impedance Spectroscopy
EE	Energy Efficiency
e^-	Electron
F	Faraday’s Constant
FTIR	Fourier Transformed Infrared Spectroscopy
HPOM	Acid Form Polyoxometalate
ICM	Ion Conducting Membrane
IEM	Ion Exchange Membrane
LBL	Layer-by-layer
LIB	Lithium Ion Battery
LiTf	Lithium Trifluoromethanesulfonate
LiPOM	Lithium Form Polyoxometalate
$LiPF_6$	Lithium Hexafluorophosphate
n	Number of Electron Transferred
POM	Polyoxometalate

RFB	Redox Flow Battery
SoC	State of Charge
$TBABF_4$	Tetrabutylammonium Tetrafluoroborate
$TEABF_4$	Tetraethylammonium Tetrafluoroborate
TGA	Thermal Gravimetric Analysis
UV-Vis	Ultraviolet–Visible Spectroscopy
XRD	X-Ray Diffraction

Abstract

Scalable energy storage technologies are needed to integrate high levels of intermittent energy sources, such as wind and solar, into the grid. Redox Flow Batteries (RFBs), designed to store energy in chemical form known as the electrolyte, can help address the energy storage problem. However, most traditional RFBs are aqueous systems in which the cell voltage is limited by undesired water splitting. Non-aqueous RFBs could permit higher cell voltages by removing this limitation. One proposed non-aqueous RFB system is based on polyoxometalates (POMs). POMs have versatile, tunable properties and can undergo multi-electron redox reactions which may meet the requirements of high performance Redox Flow Batteries. This dissertation presents work investigating the electrochemical characteristics of the different combinations of Keggin-type polyoxometalates ($XM_mO_{40}^{n-}$). Effects of the counter cations, central heteroatoms, and framework metal atoms on the electrochemical characteristics were compared. The basic characteristics of POMs including FTIR, XRD, TGA and bulk electrolysis were examined and compared in this research in order to have a better understanding of Keggin-type polyoxometalates. With understanding of the influences of different Keggin-type polyoxometalates on the electrochemical characteristics, suitable lithium polyoxometalate salts were selected that can be used for non-aqueous Redox Flow Batteries in a static H cell. Conditions of POMs charge/discharge including membrane selection were determined there. The aramid nanofiber (ANF) membrane showed a high separation ability and low resistance, and was therefore selected as the test membrane for battery charge/discharge experiments. Additionally, the POMs were applied to different types of redox flow batteries with some of the results yielding high coulombic efficiency (~90%), reflecting the reversibility of polyoxometalate redox reactions. Different kinds of RFBs were compared in this research and the performance of a RFB with a high concentration (0.1 M $Li_3PMo_{12}O_{40}$) was also demonstrated to be successful, surpassing the concentration range of previous POM RFB studies in the literature. Last, an asymmetric POM RFB charge/discharge was demonstrated for the purpose of achieving a higher voltage window. Overall, these studies provide proof of concept for polyoxometalate applications in non-aqueous redox flow batteries.

Chapter 1

Introduction

1.1 Energy storage and Redox Flow battery

1.1.1 Introduction of Redox flow battery

The availability of cheap, reliable energy sources is essential in today's society, with ever-increasing demand as developing nations continue their economic progress. Renewable energy has seen growing interest from developed nations dependent on fossil fuel supply and concerns about the climate impacts of greenhouse gas emissions. Solar and wind power have become commercially viable and competitive with fossil fuels for electricity generation [1,2]. The supply of renewable energy is estimated to grow from 13% of total U.S. electricity generation in 2015 to approximately double that percentage in 2040 according to the U.S. Energy Information Administration Reference Case [3].

However, renewable energy is not consistently available all the time. Therefore, proper energy storage systems are needed. Common storage systems include mechanical storage, pumped-storage hydroelectricity, compressed air energy storage, gravitational potential energy storage with solid masses, thermal storage, etc. Large-scale integration of renewable energy sources presents new challenges, as most cannot produce energy on demand. One of the largest hurdles to large-scale implementation is therefore energy storage and delivery. Among battery technologies, redox flow batteries (RFBs) have gained interest over the past several decades, as their design allows for flexible layouts and they can be scaled to meet different grid needs [4]. Several kinds of the redox flow batteries have been commercialized, Figure 1-1 shows a commercial redox flow battery from Sumitomo Electric Industries [5].

Figure 1-1. Sumitomo Electric Industries redox flow battery [5]

Redox flow batteries (RFBs) are considered to be a high-capacity, reversible, scalable energy storage system, and may play a key role in electrical grid energy storage. Also, redox flow batteries can decouple power and energy density, unlike the traditional batteries. The power density is determined by the surface area of the battery electrodes and energy density is determined by the amount of electrolyte; therefore, design of RFBs can be very flexible. The energy of the RFB is stored in the electrolyte; therefore, it can be scaled to fit different needs, and more importantly, it is not dependent on terrain. In addition, the electrochemical reaction in some redox flow batteries has been shown to be faster than that in lithium-ion batteries[6]. Lithium ion batteries are limited in lifetime stability by repeated insertion and deinsertion of Li cations into the active electrode material, while RFBs are typically limited in stability only by the active species. All-vanadium RFBs have been shown to be stable for more than ten years [7].

A schematic of a redox flow battery is shown in Figure 1-2. The typical redox flow battery is composed of electrolyte tanks, separator (ion exchange membrane or nano pore size membrane), electrodes, pumps, and power sources. Electrolyte tanks are where the electrolyte is stored. When charging, the catholyte is oxidized and the anolyte is reduced, and vice versa when discharging. The catholyte and anolyte can be the same chemical, in which case the flow battery is symmetric, or they can be different species in the case of asymmetric redox flow batteries. Pumps are required to circulate the electrolyte solutions while the cell is charged or discharged.

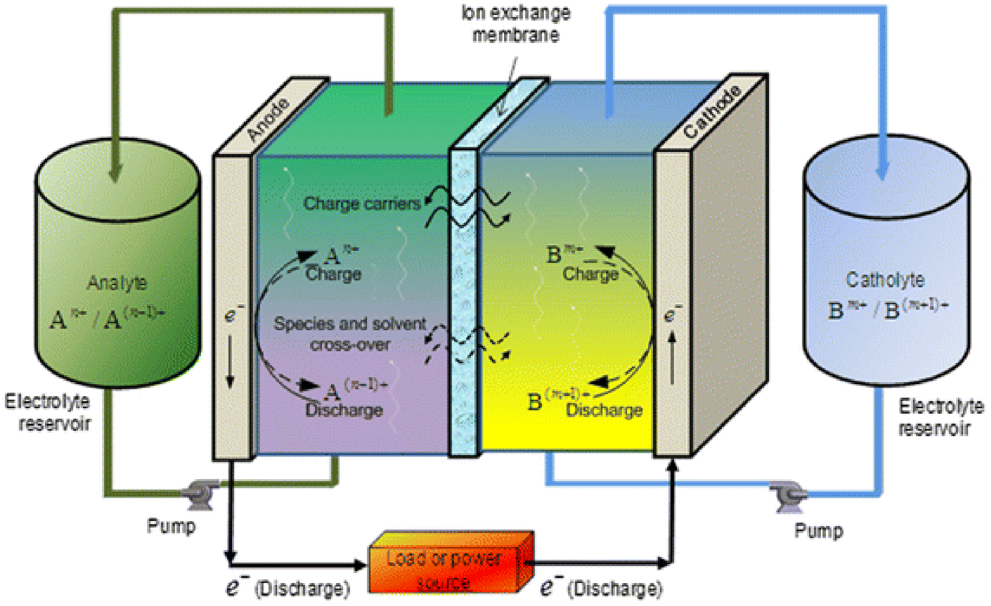

Figure 1-2 A redox flow battery [4]

The membrane (or separator) is one of the important parts of the RFBs. The membrane (or separator) allows the catholyte and anolyte to exchange charged species efficiently while keeping these solutions separated. Undesired crossover of chemical species is a crucial issue if the membrane (or separator) is not sufficiently selective. For a symmetric redox flow battery, crossover results in self-discharge, lowering the efficiency. For an asymmetric battery, crossover results not only in the loss of energy, but also cross-contamination of the electrolyte solutions.

The chemical properties of the RFB electrolytes can be considered in three parts: solvent, active species (solute) and supporting electrolyte. Currently all commercial redox flow batteries are aqueous systems because of the high solubility of the solute (~ 2M in all-vanadium RFBs [4]) and low cost. However, aqueous systems are limited by the stable electrochemical window of water (1.5V); if the applied voltage is higher than 1.5 V, then water splitting can occur to form hydrogen and oxygen. Non-aqueous redox flow batteries with a wide stable solvent voltage window have been considered in order to solve this problem. For example, acetonitrile has a 5V stable window. However, in general inorganic species have lower solubility in organic solvents than in water, potentially limiting the energy density of the cell. Finally, the role of the supporting electrolyte is to increase the solution conductivity, but it should not react with the active species or other components of the RFB.

1.1.2 Aqueous Redox Flow Batteries

The first redox flow battery was designed by Posner in 1955 [8]. Unlike the common redox flow batteries today, the system was based on chemical rather than reversible electrochemical regeneration of the electrolytes. The first redox flow battery which allowed the dissolved cation and anion charge and discharge came out from NASA [9] by Thaller et al. However, the biggest challenge for the system was the crossover of the two sides of the electrolyte. Several common redox flow batteries developed since are summarized below [4]:

1. Iron/chromium (Fe/Cr)[10]:

Developed by NASA in the 1970s with 1 kW/13 kWh system. The system was easy to setup and could be operated with an ion exchange membrane (IEM). Low open-circuit potential and crossover were two main problems.

2. Bromine/polysulfide (Br/S) [11]

This system was patented by Remick in 1984. It exhibited high capacity – up to 12 MWh, with two huge 1800 m^3 catholyte and anolyte tanks. However, crossover and precipitation of H_2S and Br_2 were important limitations.

3. All-vanadium (V^{2+}/V^{3+}) [12]

This system is perhaps the most well-known redox flow battery. First designed by NASA and since been improved by many other research groups, a 5–10 kW RFB was achieved by Skyllas-Kazacos et al. [13] The limitations are precipitation and solubility. The coulombic efficiency could be up to 95%. The all-vanadium RFB system has been adopted commercially in several countries, including Australia, Austria, Canada, Germany, China (PRoC), United States of America (USA) and Japan [14].

There are some disadvantages of the aqueous redox flow batteries in the systems highlighted above. The energy density of the flow battery can be written as:

$$\text{Energy density} \propto n \times F \times V_{\text{Cell}} \times C_{\text{active}}$$

The energy density is proportional to the number of electrons transferred (n), maximum cell potential window (V_{Cell}) and the concentration of the active species (C_{active}). Water is limited by its stable electrochemical window (1.5V), therefore the potential of redox couples beyond the 1.5 V was also limited.

A variety of other kinds of redox flow batteries have been proposed, with different cell designs, active species, and solvents. Redox flow batteries have attracted significant research in recent years. The number of publications per year involving redox flow batteries has increased significantly since 2011 [15].

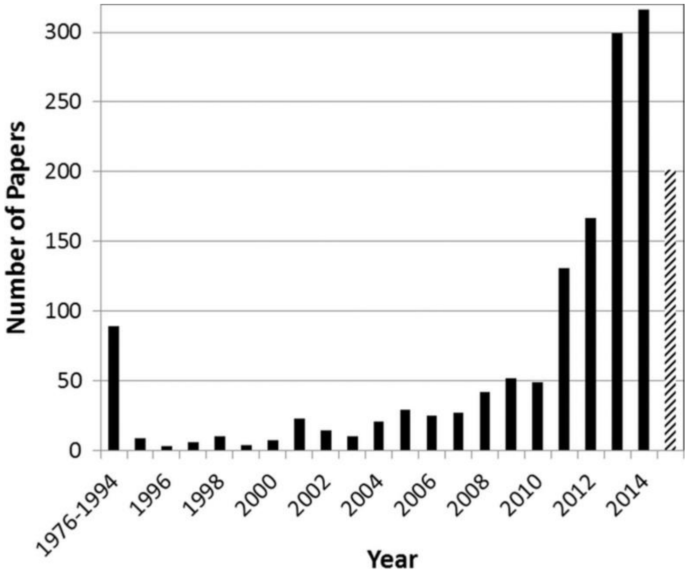

Figure 1-3 Number of publications per year involving redox flow batteries [14]

1.1.3 Non-aqueous redox flow batteries

The voltage range of the non-aqueous redox flow battery could be up to 5V for solvents such as acetonitrile [16]. Many different kinds of the non-aqueous redox flow batteries have been invented including metal-centered complexes [17][18][19][20] and redox-active macro-architectures [21][22]. Matsuda et al. first proposed the idea of a non-aqueous acetonitrile system in 1988 based on a tris(2,2'-bipyridine) ruthenium(II) tetrafluoroborate $(Ru(bpy)_3(BF_4)_2$ complex

[17]. The most studied ligand-based RFB systems are acetylacetonate (acac) complexes and bipyridine (bpy) complexes. Vanadium complexes,($V(acac)_3$) [23][24], manganese complexes [25], chromium complexes [26], nickel and iron complexes [27][28], uranium complexes [29], cobalt complexes [30], and all-organic redox systems [31] have also been considered.

However, there are some limitations of non-aqueous redox flow batteries. Higher solvent costs, higher viscosities, lower ionic conductivities, lower current densities and the compatibility of the reactants with air and water are among these [14]. This research investigates a new kind of air/water stable non-aqueous RFB with the potential for high energy density and high columbic efficiency: polyoxometalates in non-aqueous media.

1.1.4 Polyoxometalate redox flow batteries

There have been relatively few studies of polyoxometalate RFBs. Initial work was published by Anderson et al. in 2013 and 2014 [32][33][34]. These researchers mostly focused on aqueous systems with coulombic efficiencies up to 90%, to demonstrate feasibility of polyoxometalate in redox flow batteries. A propylene carbonate non-aqueous RFB with $SiV^{IV}_3W^{VI}_9O_{40}^{10-}$ was reported in [32], the electrochemical yield of the system quickly dropped by half after 10 cycles.

Unlike traditional redox flow batteries using single metal ion complexes as the active species, polyoxometalate redox flow batteries use polynuclear polyoxometalate as the active species. These air and water stable active species have the potential to undergo multielectron transfer reactions, making them interesting candidates for redox flow battery applications.

1.2 Polyoxometalates

Polyoxometalates (POMs) are polyatomic metal oxide molecular clusters, which usually consist of group 5 or group 6 transition metals linked together by oxygen atoms with the heteroatom at the core (phosphorous, silicon, etc.). Polyoxometalates (POMs) constitute a very large family of molecules with a wide variety of different structures and properties [35]. POMs were first reported by Berzelius in 1826 [36] and POM research has grown rapidly since Pope and Müller's review in 1991 [37]. The number of studies of these species, shown in Figure 1-4, including both experimental [38][39] and theoretical[40][41] investigations, has increased exponentially over the past several decades.

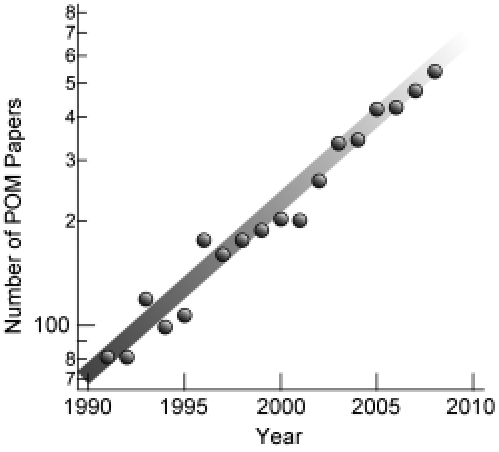

Figure 1-4 Number of publications per year that involve polyoxometalates [35]

POMs come in a vast range of different structures and sizes, and their molecular weights can vary from hundreds to thousands as shown in Figure 1-5. The most studied structures are the

Keggin ($XM_nO_{40}^{n-}$) and Dawson ($X_2M_nO_{62}^{n-}$) types [42]. Although polyoxocations can also take on the Keggin structure, e. g., the Al polyoxocation (Al_{13} Keggin ion, $(AlO_4Al_{12}(OH)_{24}(H_2O)_{12})^{7+}$), this work will consider only heteropolyanions such as $PMo_{12}O_{40}^{3-}$. These heteropolyanions can undergo several reversible and stable electron transfer reactions, which makes them good oxidants and reductants [43][44].

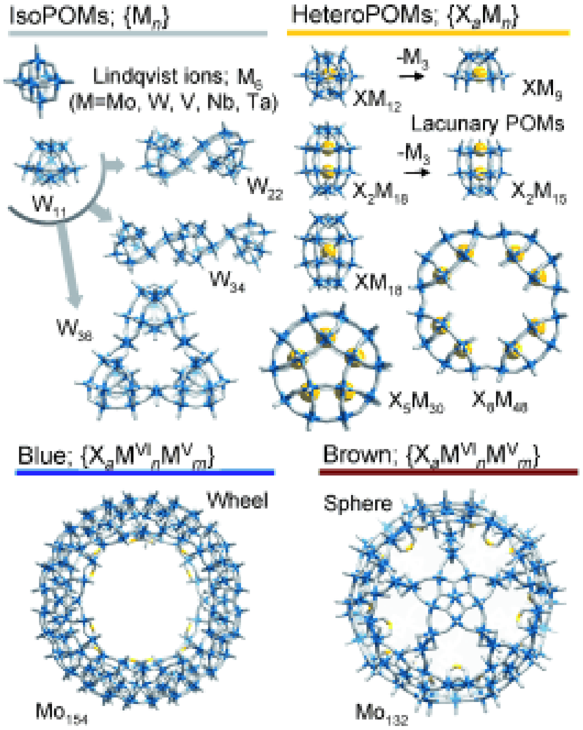

Figure 1-5 POM structure examples [35]

Characteristics of POMs include metal oxide character, stability (H_2O/air, temperature), size (6 ~ 25 Å), high molecular weight, variable oxidation states for framework metal atoms, photoreducibility, etc. POMs have been considered for a remarkable range of applications, including coatings, catalysts, processing radioactive waste, sensors, dopants in nonconductive polymers, food chemistry, and medical treatments [45][46][47].

The electrochemical behavior of POMs in solution is complicated and must be considered under each particular set of conditions. For example, the position of the redox couples is influenced by pH [48][49]. Reduction increases the charge density of the POMs and therefore the basicity. In aqueous POM solutions, the redox potentials change with a slope of 59mV/pH unit. Both pH and pK_a values affect the positions of the redox couples observed [50][51]. The electrochemical properties of POMs show different features depending on their composition and structure [52].

The applications of POMs in the energy field include capacitors [53], fuel cells [54], solar cells [55], lithium-ion batteries [56][57], as well as the redox flow battery applications by Anderson et al. mentioned previously [32].

1.3 Separator

The separator plays an important role in RFBs. The separator can influence the coulombic efficiency due to crossover issues, and the energy efficiency by its resistance. An ideal redox flow battery separator would meet the following requirements: high ionic conductivity of the electrolyte, high ion selectivity, chemical stability, mechanical stability and long lifetime [58]. Generally, separators can be classified as ion exchange membranes (IEM) and nano-porous membranes (NPM). Ion exchange membranes (IEM) can then be further classified as anion-exchange membranes (AEM) or cation-exchange membranes (CEM) based on the functional groups attached to the membrane.

One of the biggest challenges with the non-aqueous RFBs is membrane compatibility. For aqueous RFBs, suitable membranes are abundant [7][59]. However, in non-aqueous RFBs, suitable membranes are an active subject of investigation. Anion-exchange membranes (AEMs) that have been used in non-aqueous battery studies include Neosepta [60] and Ultrex^{TM} [23] . However, compatibility issues have limited their application [58]. Among cation-exchange membranes (CEMs), Nafion has been reported to have high resistance in non-aqueous solvents [61][62]. For nano-porous membranes (NPMs), selection ability is based on pore size. For RFBs, crossover is the main issue, as most of the active species are too small for the current NPMs to prevent crossover. The aramid nanofiber (ANF) membranes developed by Ming et al. [63] open a new possible path for smaller pore size NPMs, and were utilized in much of the present work.

1.4 Research Goals and Thesis Layout

The goal of this research is to establish a new air/water stable, high energy density and high stability non-aqueous redox flow battery system by applying polyoxometalates. Important foci include:

1. Investigation of polyoxometalate behavior in non-aqueous systems and identification of the effects of each component in the polyoxometalates.
2. Establishment of the form of the POM non-aqueous RFB system, including electrolyte material and membranes, and exploration of appropriate POMs for RFB applications.
3. Demonstration of the performance of non-aqueous POM-based non-aqueous RFBs.

Subsequent chapters of this dissertation are summarized below.

Chapter 2 Polyoxometalate Electrochemical Characteristics in Solution

This chapter describes the Keggin polyoxometalate electrochemical behavior in acetonitrile. Different components of the Keggin POMs were exchanged and the POMs were characterized by cyclic voltammetry. The effects of counter cation, heteroatom and framework transition metal exchange were studied. After cyclic voltammetry measurements of the POMs, the electrochemical behavior of the aqueous acid form and lithium salt form POMs (LiPOM) in acetonitrile were compared. This work produced a new correlation of the redox potentials between the two systems. A systematic investigation of POM electrochemical behavior was made in this chapter for the further battery design.

Chapter 3 General Chemical Characteristics of Polyoxometalates

Several physical and chemical characteristics of polyoxometalates were investigated in this chapter, including solubility, Thermal Gravimetric Analysis (TGA), X-ray Diffraction (XRD), Fourier Transform Infrared Spectroscopy (FTIR) and bulk electrolysis (BE). The solubility information can be used as a guide for estimating POM battery energy densities. TGA was used to examine the water content of the POMs, which typically contain a large number of associated water molecules in the solid state. XRD and FTIR were used to confirm the structures of the POMs. FTIR spectra of POMs in different oxidation states were examined as well. The bulk electrolysis (BE) results demonstrated the stability of some POMs and the number of electron transfers potentially accessible in RFB operations.

Chapter 4 Polyoxometalate Charge and Discharge Performance as Batteries in Static Cell Studies

The separator of the battery and the charge/discharge stability of POMs were examined in this chapter. Ion exchange membranes (IEM) and nano-porous membranes (NPM) were studied with $Li_3PMo_{12}O_{40}$ as the POM. Nafion®117 was used as the cation exchange membrane (CEM), Celgard2325 and aramid nanofiber (ANF) nano-porous membranes were also tested. Both electrochemical impedance spectroscopy (EIS) and crossover tests were performed to test Nafion®117, Celgard2325 and aramid nanofiber (ANF) membranes. After membrane selection, static cell charge/discharge tests were carried out to examine the stability of the active species (POMs) as flow battery materials. The long-term stability of $Li_3PMo_{12}O_{40}$ was tested for over 1000 hours to demonstrate the stability of this POM. $Li_3PW_{12}O_{40}$, $Cu_{1.5}PMo_{12}O_{40,}$ were also tested in the static cell in symmetric charge/discharge experiments. Asymmetric charge/discharge experiments with different POMs were performed to investigate the feasibility of higher energy densities (wider voltage window and more electron transfer couples.)

Chapter 5 Redox Flow Battery Performance

$Li_3PMo_{12}O_{40}$ was selected for the redox flow battery tests because of it stability and high solubility in acetonitrile. Two types of flow battery were tested here, the Gen 1 flow battery [63] and the Gen 2 flow battery[64]. The Gen 1 flow battery current collectors were machined from type 316 stainless steel with flow through pattern channel. The Gen 2 flow battery was also tested [64]; the flow cell was machined from polypropylene for chemical compatibility with acetonitrile, and the current collectors were made from thick impregnated graphite. Multiple cycles of the POM redox flow battery were tested for different electrolyte compositions, including both symmetric and asymmetric RFB configurations.

Chapter 6 Summary, Limitations and Future Work

The final chapter organizes and summary the previous chapters key finding which including the POMs electrochemical characteristics and the applications in redox flow batteries for energy storage. The limitations and future research needs are discussed in this chapter based on the results of this research.

1.5 References

[1] Tester, J.W., Drake, E.M.,Driscoll, M.J., Golay, M.W. and Peters, W.A. *Sustainable energy: choosing among options*. MIT Press, 2012.

[2] Nguyen, T., & Savinell, R. F. (2010). Flow batteries. *The Electrochemical Society Interface*, *19*(3), 54-56.

[3] *Annual Energy Outlook* (2017). Energy Information Administration. U. S. Department of Energy.

[4] Weber, A. Z., Mench, M. M., Meyers, J. P., Ross, P. N., Gostick, J. T., & Liu, Q. (2011). Redox flow batteries: a review. *Journal of Applied Electrochemistry, 41*(10), 1137-1164.

[5] Kenkyu, S. (2012, December 14). No. 668: Sumitomo Electric mass produces redox flow batteries next year. *High-Tech Industry in Japan.*

[6] De Leon, C. P., Frías-Ferrer, A., González-García, J., Szánto, D. A., & Walsh, F. C. (2006). Redox flow cells for energy conversion. *Journal of Power Sources*, *160*(1), 716-732.

[7] Wang, W., Luo, Q., Li, B., Wei, X., Li, L., & Yang, Z. (2013). Recent progress in redox flow battery research and development. *Advanced Functional Materials*, *23*(8), 970-986.

[8] Posner, A. M. (1955). Redox fuel cell. *Fuel*, *34*(3), 330-338.

[9] Thaller, L. H. (1976). *U.S. Patent No. 3,996,064*. Washington, DC: U.S. Patent and Trademark Office.

[10] Bartolozzi, M. (1989). Development of redox flow batteries. A historical bibliography. *Journal of Power Sources*, *27*(3), 219-234.

[11] Remick, R. J., & Ang, P. G. (1984). *U.S. Patent No. 4,485,154*. Washington, DC: U.S. Patent and Trademark Office.

[12] Yang, Z., Zhang, J., Kintner-Meyer, M. C., Lu, X., Choi, D., Lemmon, J. P., & Liu, J. (2011). Electrochemical energy storage for green grid. *Chemical Reviews*, *111*(5), 3577-3613.

[13] Skyllas-Kazacos, M. (2003). Novel vanadium chloride/polyhalide redox flow battery. *Journal of Power Sources*, *124*(1), 299-302.

[14] Kear, G., Shah, A. A., & Walsh, F. C. (2012). Development of the all-vanadium redox flow battery for energy storage: a review of technological, financial and policy aspects. *International Journal of Energy Research*, *36*(11), 1105-1120.

[15] Perry, M. L., & Weber, A. Z. (2016). Advanced redox-flow batteries: a perspective. *Journal of The Electrochemical Society*, *163*(1), A5064-A5067.

[16] Bard, A. J., Faulkner, L. R., Leddy, J., & Zoski, C. G. (1980). *Electrochemical methods: fundamentals and applications* (Vol. 2). New York: Wiley.

[17] Matsuda, Y., Tanaka, K., Okada, M., Takasu, Y., Morita, M., & Matsumura-Inoue, T. (1988). A rechargeable redox battery utilizing ruthenium complexes with non-aqueous organic electrolyte. *Journal of Applied Electrochemistry*, *18*(6), 909-914.

[18] Chakrabarti, M. H., Dryfe, R. A. W., & Roberts, E. P. L. (2007). Evaluation of electrolytes for redox flow battery applications. *Electrochimica Acta*, *52*(5), 2189-2195.

[19] Laramie, S. M., Milshtein, J. D., Breault, T. M., Brushett, F. R., & Thompson, L. T. (2016). Performance and cost characteristics of multi-electron transfer, common ion exchange non-aqueous redox flow batteries. *Journal of Power Sources*, *327*, 681-692.

[20] Chakrabarti, M. H., Lindfield Roberts, E. P., & Saleem, M. (2010). Charge–discharge performance of a novel undivided redox flow battery for renewable energy storage. *International Journal of Green Energy*, *7*(4), 445-460.

[21] Nagarjuna, G., Hui, J., Cheng, K. J., Lichtenstein, T., Shen, M., Moore, J. S., & Rodríguez-López, J. (2014). Impact of redox-active polymer molecular weight on the electrochemical properties and transport across porous separators in nonaqueous solvents. *Journal of the American Chemical Society*, *136*(46), 16309-16316.

[22] Winsberg, J., Hagemann, T., Muench, S., Friebe, C., Häupler, B., Janoschka, T., Morgenstern S., Hager M., Schubert, U. (2016). Poly (boron-dipyrromethene)—A Redox-Active Polymer Class for Polymer Redox-Flow Batteries. *Chemistry of Materials*, *28*(10), 3401-3405.

[23] Shinkle, A. A., Pomaville, T. J., Sleightholme, A. E., Thompson, L. T., & Monroe, C. W. (2014). Solvents and supporting electrolytes for vanadium acetylacetonate flow batteries. *Journal of Power Sources*, *248*, 1299-1305.

[24] Zhang, D., Liu, Q., Shi, X., & Li, Y. (2012). Tetrabutylammonium hexafluorophosphate and 1-ethyl-3-methyl imidazolium hexafluorophosphate ionic liquids as supporting electrolytes for non-aqueous vanadium redox flow batteries. *Journal of Power Sources*, *203*, 201-205.

[25] Sleightholme, A. E., Shinkle, A. A., Liu, Q., Li, Y., Monroe, C. W., & Thompson, L. T. (2011). Non-aqueous manganese acetylacetonate electrolyte for redox flow batteries. *Journal of Power Sources*, *196*(13), 5742-5745.

[26] Liu, Q., Shinkle, A. A., Li, Y., Monroe, C. W., Thompson, L. T., & Sleightholme, A. E. (2010). Non-aqueous chromium acetylacetonate electrolyte for redox flow batteries. *Electrochemistry Communications*, *12*(11), 1634-1637.

[27] Kim, J. H., Kim, K. J., Park, M. S., Lee, N. J., Hwang, U., Kim, H., & Kim, Y. J. (2011). Development of metal-based electrodes for non-aqueous redox flow batteries. *Electrochemistry Communications*, *13*(9), 997-1000.

[28] Mun, J., Lee, M. J., Park, J. W., Oh, D. J., Lee, D. Y., & Doo, S. G. (2012). Non-aqueous redox flow batteries with nickel and iron tris (2, 2′-bipyridine) complex electrolyte. *Electrochemical and Solid-State Letters*, *15*(6), A80-A82.

[29] Yamamura, T., Shiokawa, Y., Yamana, H., & Moriyama, H. (2002). Electrochemical investigation of uranium β-diketonates for all-uranium redox flow battery. *Electrochimica Acta*, *48*(1), 43-50.

[30] Zhang, D., Lan, H., & Li, Y. (2012). The application of a non-aqueous bis (acetylacetone) ethylenediamine cobalt electrolyte in redox flow battery. *Journal of Power Sources*, *217*, 199-203.

[31] Li, Z., Li, S., Liu, S., Huang, K., Fang, D., Wang, F., & Peng, S. (2011). Electrochemical properties of an all-organic redox flow battery using 2, 2, 6, 6-tetramethyl-1-piperidinyloxy and N-methylphthalimide. *Electrochemical and Solid-State Letters*, *14*(12), A171-A173.

[32] Pratt, H. D., Hudak, N. S., Fang, X., & Anderson, T. M. (2013). A polyoxometalate flow battery. *Journal of Power Sources*, *236*, 259-264.

[33] Pratt, H. D., & Anderson, T. M. (2013). Mixed addenda polyoxometalate “solutions” for stationary energy storage. *Dalton Transactions*, *42*(44), 15650-15655.

[34] Pratt, H. D., Pratt, W. R., Fang, X., Hudak, N. S., & Anderson, T. M. (2014). Mixed-metal, structural, and substitution effects of polyoxometalates on electrochemical behavior in a redox flow battery. *Electrochimica Acta*, *138*, 210-214.

[35] Long, D. L., Tsunashima, R., & Cronin, L. (2010). Polyoxometalates: building blocks for functional nanoscale systems. *Angewandte Chemie International Edition*, *49*(10), 1736-1758.

[36] Hill, C. L. (1998). Introduction: polyoxometalates multicomponent molecular vehicles to probe fundamental issues and practical problems. *Chemical Reviews*, 98(1), 1-2.

[37] Pope, M. T., & Müller, A. (1991). Polyoxometalate chemistry: an old field with new dimensions in several disciplines. *Angewandte Chemie International Edition*, *30*(1), 34-48.

[38] Sartorel, A., Carraro, M., Scorrano, G., Zorzi, R. D., Geremia, S., McDaniel, N. D., Bernhard S. & Bonchio, M. (2008). Polyoxometalate embedding of a tetraruthenium (IV)-oxo-core by template-directed metalation of [γ-$SiW_{10}O_{36}$]$^{8-}$: a totally inorganic oxygen-evolving catalyst. *Journal of the American Chemical Society*, *130*(15), 5006-5007.

[39] Neumann, R., & Dahan, M. (1997). A ruthenium-substituted polyoxometalate as an inorganic dioxygenase for activation of molecular oxygen. *Nature*, *388*(6640), 353-355.

[40] Yan, L., López, X., Carbó, J. J., Sniatynsky, R., Duncan, D. C., & Poblet, J. M. (2008). On the origin of alternating bond distortions and the emergence of chirality in polyoxometalate anions. *Journal of the American Chemical Society*, *130*(26), 8223-8233.

[41] Bagno, A., & Bonchio, M. (2005). Vicinal Tungsten–Tungsten Coupling Constants in Polyoxotungstates: DFT Calculations Challenge an Empirical Rule. *Angewandte Chemie International Edition*, *44*(13), 2023-2026.

[42] Sadakane, M., & Steckhan, E. (1998). Electrochemical properties of polyoxometalates as electrocatalysts. *Chemical Reviews*, *98*(1), 219-238.

[43] So, H., & Pope, M. T. (1972). Origin of some charge-transfer spectra. Oxo compounds of vanadium, molybdenum, tungsten, and niobium including heteropoly anions and heteropoly blues. *Inorganic Chemistry*, *11*(6), 1441-1443.

[44] Okuhara, T., Mizuno, N., & Misono, M. (1996). Catalytic chemistry of heteropoly compounds. *Advances in Catalysis*, *41*, 113-252.

[45] Katsoulis, D. E. (1998). A survey of applications of polyoxometalates. *Chemical Reviews*, *98*(1), 359-388.

[46] Dolbecq, A., Dumas, E., Mayer, C. R., & Mialane, P. (2010). Hybrid organic− inorganic polyoxometalate compounds: from structural diversity to applications. *Chemical Reviews*, *110*(10), 6009-6048.

[47] Judd, D.A., Nettles, J.H., Nevins, N., Snyder, J.P., Liotta, D.C., Tang, J., Ermolieff, J., Schinazi, R.F. and Hill, C.L. (2001). Polyoxometalate HIV-1 protease inhibitors. A new mode of protease inhibition. *Journal of the American Chemical Society*, *123*(5), 886-897.

[48] Himeno, S., Maeda, K., Osakai, T., Saito, A., & Hori, T. (1993). A voltammetric study on the one-electron redox processes of the Dawson-type heteropolymolybdate complexes. *Bulletin of the Chemical Society of Japan*, *66*(1), 109-113.

[49] Maeda, K., Himeno, S., Osakai, T., Saito, A., & Hori, T. (1994). A voltammetric study of Keggin-type heteropolymolybdate anions. *Journal of Electroanalytical Chemistry*, *364*(1-2), 149-154.

[50] Maeda, K., Katano, H., Osakai, T., Himeno, S., & Saito, A. (1995). Charge dependence of one-electron redox potentials of Keggin-type heteropolyoxometalate anions. *Journal of Electroanalytical Chemistry*, *389*(1-2), 167-173.

[51] Altenau, J. J., Pope, M. T., Prados, R. A., & So, H. (1975). Models for heteropoly blues. Degrees of valence trapping in vanadium (IV)-and molybdenum (V)-substituted Keggin anions. *Inorganic Chemistry*, *14*(2), 417-421.

[52] Brewer, K. J. (2007). in *Encyclopedia of Electrochemistry, Volume 7b: Inorganic Electrochemistry*, Scholz, F. and Pickett, C. J. (eds.). Wiley-VCH Verlag GmbH & Co. KGaA: Weinheim. 2006.

[53] Akter, T., Hu, K., & Lian, K. (2011). Investigations of multilayer polyoxometalates-modified carbon nanotubes for electrochemical capacitors. *Electrochimica Acta*, *56*(14), 4966-4971.

[54] Kim, W. B., Voitl, T., Rodriguez-Rivera, G. J., & Dumesic, J. A. (2004). Powering fuel cells with CO via aqueous polyoxometalates and gold catalysts. *Science*, *305*(5688), 1280-1283.

[55] Palilis, L. C., Vasilopoulou, M., Douvas, A. M., Georgiadou, D. G., Kennou, S., Stathopoulos, N. A., Constantoudis, V. & Argitis, P. (2013). Solution processable tungsten polyoxometalate as highly effective cathode interlayer for improved efficiency and stability polymer solar cells. *Solar Energy Materials and Solar Cells*, *114*, 205-213.

[56] Uematsu, S., Quan, Z., Suganuma, Y., & Sonoyama, N. (2012). Reversible lithium charge–discharge property of bi-capped Keggin-type polyoxovanadates. *Journal of Power Sources*, *217*, 13-20.

[57] Sonoyama, N., Suganuma, Y., Kume, T., & Quan, Z. (2011). Lithium intercalation reaction into the Keggin type polyoxomolybdates. *Journal of Power Sources*, *196*(16), 6822-6827.

[58] Shin, S. H., Yun, S. H., & Moon, S. H. (2013). A review of current developments in non-aqueous redox flow batteries: characterization of their membranes for design perspective. *Rsc Advances*, *3*(24), 9095-9116.

[59] Parasuraman, A., Lim, T. M., Menictas, C., & Skyllas-Kazacos, M. (2013). Review of material research and development for vanadium redox flow battery applications. *Electrochimica Acta*, *101*, 27-40.

[60] Shinkle, A. A., Sleightholme, A. E., Griffith, L. D., Thompson, L. T., & Monroe, C. W. (2012). Degradation mechanisms in the non-aqueous vanadium acetylacetonate redox flow battery. *Journal of Power Sources*, *206*, 490-496.

[61] Sachan, S., Ray, C. A., & Perusich, S. A. (2002). Lithium ion transport through nonaqueous perfluoroionomeric membranes. *Polymer Engineering & Science*, *42*(7), 1469-1480.

[62] Goswami, A., Acharya, A., & Pandey, A. K. (2001). Study of self-diffusion of monovalent and divalent cations in Nafion-117 ion-exchange membrane. *The Journal of Physical Chemistry B*, *105*(38), 9196-9201.

[63] Yang, M., Cao, K., Sui, L., Qi, Y., Zhu, J., Waas, A., Arruda, E.M., Kieffer, J., Thouless, M.D. and Kotov, N.A. (2011). Dispersions of aramid nanofibers: a new nanoscale

building block. *ACS Nano*, *5*(9), 6945-6954.

[64] Laramie, S. M., Milshtein, J. D., Breault, T. M., Brushett, F. R., & Thompson, L. T. (2016). Performance and cost characteristics of multi-electron transfer, common ion exchange non-aqueous redox flow batteries. *Journal of Power Sources*, *327*, 681-692.

[65] Milshtein, J. D., Fisher, S. L., Breault, T. M., Thompson, L. T., & Brushett, F. R. (2017). Feasibility of a supporting-salt-free nonaqueous redox flow battery utilizing ionic active materials. *ChemSusChem*, *10*(9), 2080-2088.

Chapter 2

Electrochemical Properties Of Keggin-Structure Polyoxometalates In Acetonitrile: Effects Of Counter-Cation, Heteroatom And Framework Metal

Portions of work summarized in this chapter were published in Chen, J. J. J., & Barteau, M. A., Electrochemical properties of Keggin-structure Polyoxometalates in acetonitrile: Effects of counter-cation, heteroatom and framework metal exchange. Industrial & Engineering Chemistry Research 2016, 55, 9857

2.1 Background and Approach

Polyoxometalates (POMs) represent a large class of early transition metal oxide clusters capable of multiple electron transfer reactions that are of interest in electrochemistry and catalysis. POMs generally contain at least three or more transition metal atoms of Groups V or VI, combined with oxygen atoms. POMs with many different structures have been found; two of the most common types are Keggin-type POMs ($[XM_{12}O_{40}]^{q-}$, where X = P, Si, Ge, etc., and M = Mo, W, etc.), and Wells-Dawson type ($[X_2M_{18}O_{62}]^{q-}$ [1,2]. The redox properties of POMs vary depending on their structure and the combinations of different elements. They also show different properties in different solvents. The large majority of electrochemical studies of POM redox properties have been carried out in aqueous systems and a compilation can be found in the review by Sadakane and Steckhan [3]. POM redox properties in a solvent-free environment have also been measured for POM monolayers on graphite by scanning tunneling spectroscopy [4]. These have been shown to correlate well with first reduction potentials in water for Keggin-type POMs [5].

The present work is an evaluation of the electrochemical properties of POMs with a view toward their potential application in Redox Flow Batteries (RFBs). RFBs are mainly used for large-scale integration of renewable energy sources that need a high-capacity and rechargeable energy storage system [6,7]. However, the voltage range of electrochemical storage systems is limited by the electrochemical stability of the solvent. Non-aqueous RFBs are of interest for their potentially wider range of operating voltage. Acetonitrile has received attention as a possible solvent because of the wider stable voltage window (~5V) compared to water (~1.5V) [8].

Possible advantages of using POMs as active species in battery applications are their highly reversible multi-electron redox processes and tunable redox properties. One report has indicated that $H_3PMo_{12}O_{40}$ incorporated into electrodes can undergo as many as 24 single electron transfers during charge/discharge cycles [9]. Moreover, the redox properties of POMs are tunable via substitutions of framework metals, central heteroatoms, and counter ions, as well as structural variations [10].

This chapter investigates Keggin-type POM redox properties in acetonitrile for potential application in non-aqueous RFBs. Redox properties of POMs with different counter-cations, heteroatoms, and framework metals in acetonitrile are compared. Variations include H, Li, Na, K, Mg, Ca counter-cations; Si, P, As heteroatoms; and Mo, W, and V-containing frameworks.

2.2 Material and Methods

2.1.1 Preparation of the Keggin POMs

Phosphomolybdic acid ($H_3PMo_{12}O_{40}$, ≥99.99%) and $Na_3PMo_{12}O_{40}$ were obtained from Sigma Aldrich and phosphotungstic acid ($H_3PW_{12}O_{40}$) from Fisher Scientific. $Li_4PMo_{11}VO_{40}$ was obtained from Nippon Inorganic Colour & Chemical Co., Ltd. Other heteropolyacid samples were as described in [5]. Counter-cation exchanges were performed as described in the literature to produce $Li_3PMo_{12}O_{40}$ [11] and other Li-exchanged POMs, as well as $Mg_{1.5}PMo_{12}O_{40}$ [12] and $Ca_{1.5}PMo_{12}O_{40}$ [12]. Lithium carbonate (Li_2CO_3, 99.997% trace metals basis), magnesium carbonate hydroxide hydrate ($C_4Mg_4O_{12} \cdot H_2MgO_2 \cdot xH_2O$) and calcium carbonate ($CaCO_3$) used for cation exchanges were all obtained from Sigma Aldrich. All counter-cation exchanged polyoxometalates were exchanged following protocols described in [11,12,13] and then purified by recrystallization in acetonitrile. Elemental compositions were determined by Inductively Coupled Plasma - Optical Emission Spectroscopy (Perkin-Elmer Optima 2000 DV with Winlab software).

2.2.2 Cyclic voltammetry

Cyclic Voltammetry (CV) is a common and powerful potentiostatic electrochemical experiment that reveals the redox properties of an active species in solution. This is the technique used for investigating polyoxometalate electrochemical characteristics. A CV experiment monitors the change in current while the potential is varied. When the active species is reduced or oxidized, an increase in current occurs, resulting in reduction (E_{pc}) and oxidation peaks (E_{pa}). An ideal 1-electron reversible redox couple should have a peak voltage difference for the E_{pc} and E_{pa} peaks of 59mV. For an ideal reversible redox couple, the ratio of the reduction peak (i_{pc}) and oxidation peak currents (i_{pa}) should be close to 1. The peak height ratio (i_{pa}/i_{pc}) and the peak voltage difference (E_{pc} - E_{pa}) can be tools for examining the stability or reversibility of the redox couple for further charge/discharge screening purposes.

The standard potential (E^0) is define as the mean value (E_{mid}) of reduction (E_{pc}) and oxidation peaks (E_{pa}) [14]. Cyclic voltammetry can also be used to measure the diffusion coefficient by applying the Randles–Sevcik equation [15]:

$$i_p = 0.4463nFAC[nFvD/(RT)]^{0.5}$$

where i_p is current (A), n is number of electrons transferred in the redox reactions, A is electrode area in cm^2, F is Faraday constant, D is diffusion coefficient in cm^2/s, C is concentration in mol/cm^3, v is scan rate in V/s, R is the gas constant and T is the absolute temperature.

All POMs were dissolved in acetonitrile (Sigma Aldrich, 99.9%). Standard potentials and diffusivities of the polyoxometalate compounds were obtained using cyclic voltammetry (CV). All CV experiments were performed with 0.1M lithium trifluoromethanesulfonate (99.995% trace metals basis, Sigma Aldrich) as the support electrolyte in acetonitrile, except where noted. An Autolab PGSTAT302N Potentiostat was used with a three electrodes electrochemical cell with a 3 mm glassy carbon working electrode (BASi), polished and washed in an ultrasonic bath and dried before CV measurements. A graphite plate (GraphiteStore) was used for the counter electrode and the reference electrode was Ag/Ag^+ (BASi). Working solutions were bubbled with nitrogen for 10 minutes before CV experiments. All experiments were performed in air at 25 ^oC. The CV experiments were controlled with NOVA software (Autolab) and were typically carried out at a scan rate of 100mV/s. Cyclic voltammograms shown here represent the 5th scan cycle, and only stable CV plots are shown. As an illustration of the stability of these measurements,

Figure 2-1 shows the first, fiftieth and hundredth CV cycles for $Na_3PMo_{12}O_{40}$ in acetonitrile under our typical conditions. Neither peak positions nor magnitudes changed significantly during repeated cycling. CV spectra were further examined as convolution plots constructed with the NOVA software.

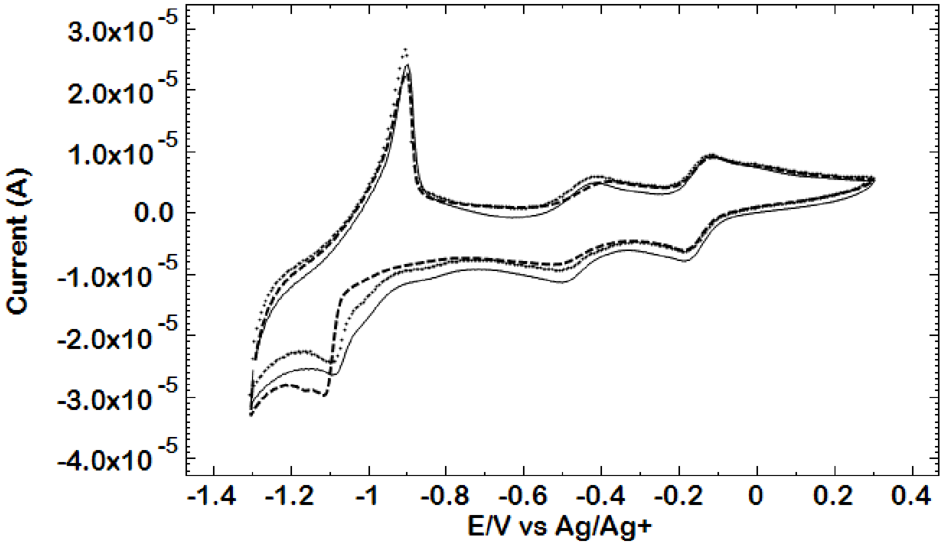

Figure 2-1 Cyclic voltammograms in acetonitrile for 0.5mM $Na_3PMo_{12}O_{40}$ with 100mM LiTf, solid line: 1st cycle; dotted line: 50th cycle; dashed line: 100th cycle

2.2.3 Bulk Electrolysis (BE)

Another electrochemical technique performed was bulk electrolysis. Bulk electrolysis involves applying a constant potential for an extended period of time. This technique is useful for changing the oxidation state of the active species to a useable form for charge/discharge experiments.

Bulk electrolysis of $Li_3PMo_{12}O_{40}$ was performed in a glass bulk electrolysis cell. The reference electrode was Ag/Ag$^+$ (BASi graphite plate (GraphiteStore) was used for the counter electrode which are same as used for cyclic voltammetry. The working electrode a was GFD4.6 carbon film from SGL Group – The Carbon Company. The experiment was performed at 10 mM

POM with 100mM LiTf stirred for the whole BE experiment. CVs were run in order to confirm the integrity of the solution after the BE experiment. Figure 2-2 demonstrates the correspondence of the first two redox couples between CV and BE experiments for $Li_3PMo_{12}O_{40}$ in acetonitrile. E_{mid} voltages for these couples are indicated by the dashed line in the Figure 2-2.

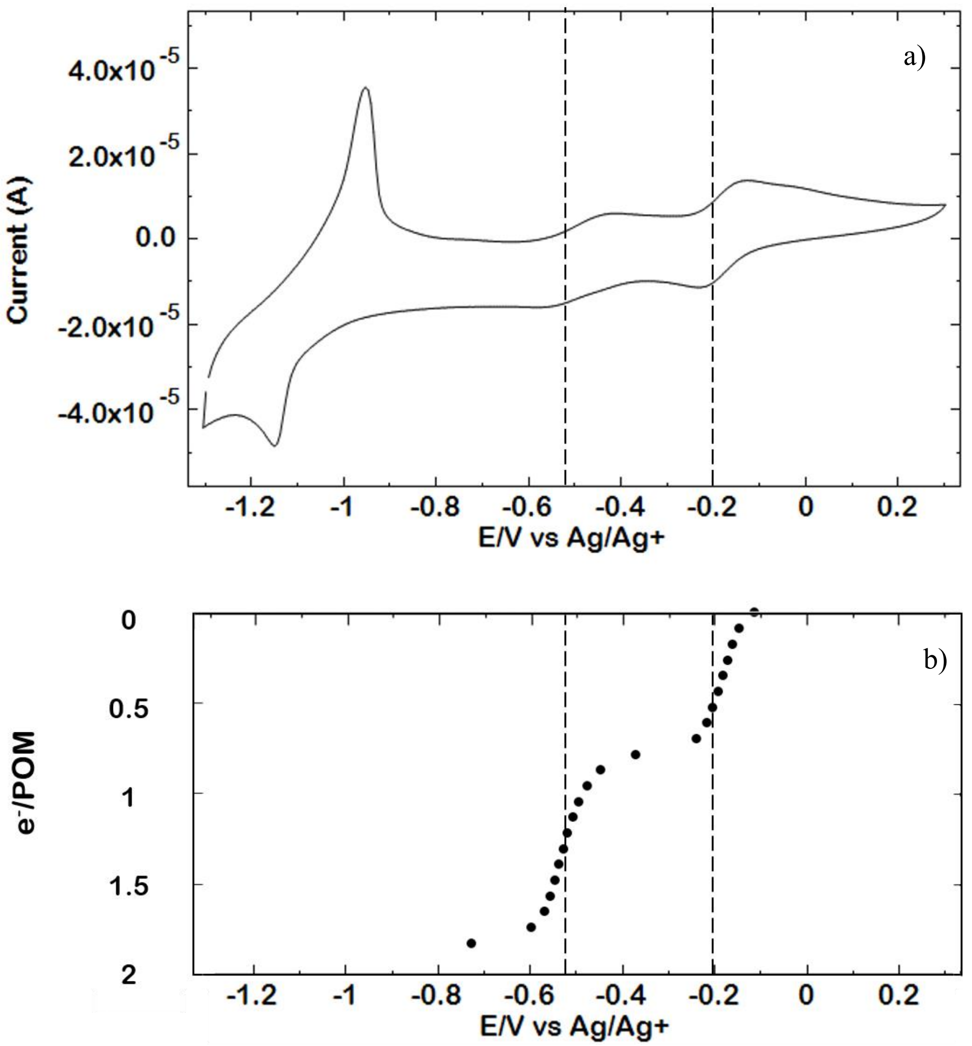

Figure 2-2 Comparison of 0.5 mM $Li_3PMo_{12}O_{40}$ cyclic voltammogram with 100mM LiTf vs. bulk electrolysis of 10 mM $Li_3PMo_{12}O_{40}$ with 100mM LiTf, a) CV, b) bulk electrolysis for the first two couples.

2.2.4 Electrochemical impedance spectroscopy

Electrochemical impedance spectroscopy (EIS) was carried out in the two electrode configuration with an Autolab PGSTAT302N Potentiostat with the same glassy carbon working electrode (BASi) and a graphite plate (GraphiteStore) as used in cyclic voltammetry experiments. These experiments were used simply to confirm the absence of significant solution resistances for the systems studied. Typical values observed were between 125 and 800 Ω.

2.3 Results and Discussion

2.3.1 Counter-cation exchanged phosphomolybdates: ($H_3PMo_{12}O_{40}$, $Li_3PMo_{12}O_{40}$, $Na_3PMo_{12}O_{40}$, $K_3PMo_{12}O_{40}$, $Mg_{1.5}PMo_{12}O_{40}$, $Ca_{1.5}PMo_{12}O_{40}$)

Cyclic voltammetry results for high (10 mM) and low (0.5 mM) concentrations of $H_3PMo_{12}O_{40}$ in acetonitrile are shown in Figure 2-3. Although the position of the first redox couple was relatively insensitive to POM concentration (E_{mid} = 10mM: 0.47 V; 0.5mM: 0.42 V), the peaks become more quasi-reversible as the concentration increased. At the lower concentration (0.5 mM) we observed 5 peaks (E_{mid} = 0.42, 0.22, -0.07, -0.49 and -0.73V) with peak separations of 0.05, 0.10, 0.07, 0.07 and 0.08V, respectively, while the 10mM $H_3PMo_{12}O_{40}$ solution exhibited 5 peaks (E_{mid} = 0.47, 0.23, -0.31, -0.54 and -0.78 V) with peak separations of 0.20, 0.17, 0.10, 0.14 and 0.09V. At the higher concentration, the reduction and oxidation peaks merged into two main quasi-reversible peaks with both oxidation and reduction (E_{pc} and E_{pa}) peak potential separation (ΔE_p) larger than 0.059 V, showing that the kinetics of this redox process for 10mM $H_3PMo_{12}O_{40}$ are slower than at lower concentrations (0.5mM.)

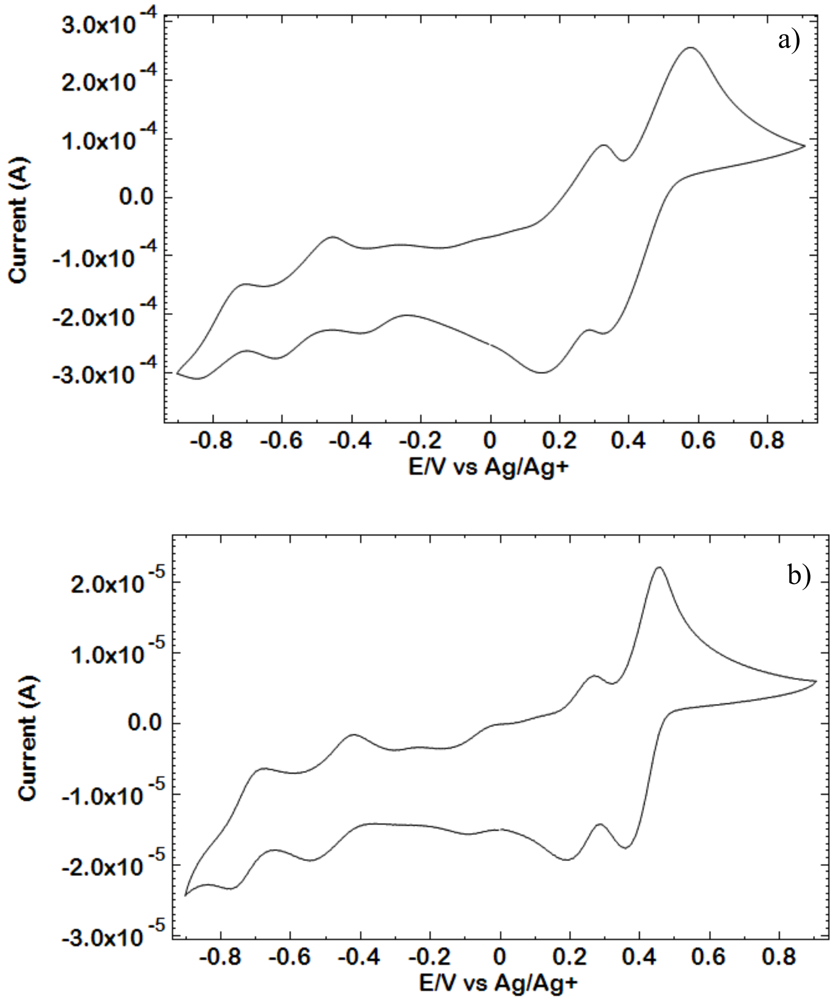

Figure 2-3 Cyclic voltammograms in acetonitrile for $H_3PMo_{12}O_{40}$ at a) 10 mM and b) 0.5 mM with 100mM LiTf, 100mV/s

Previous researchers varied the proton concentration independently, and as the proton versus POM ratio increased, redox peaks were also observed to merge [16,17]. Qualitatively similar behavior for POMs in acetonitrile solution was reported by Maeda et al. [16] Those workers examined CV spectra when different concentrations (0 ~ 3.6mM) of triflic acid (CF_3SO_3H) were used at a constant (0.5mM) concentration of $PMo_{12}O_{40}^{3-}$. As the concentration of triflic acid was increased, the potential window of the redox processes in the CV spectra narrowed. Along with this contraction, peaks shifted and converged as the proton concentration was increased, ultimately forming a series of three two-electron waves. Similar phenomena were also reported for $SiMo_{12}O_{40}^{4-}$.

CV peak shifts as a function of acid concentration were found by Himeno et al. [17] for 0.5mM $PMo_{12}O_{40}^{3-}$ and $PW_{12}O_{40}^{3-}$ in acetonitrile with different concentrations of triflic acid. These workers also examined the effect of Li^+ on $PMo_{12}O_{40}^{3-}$ and $PW_{12}O_{40}^{3-}$ CV in acetonitrile by adding different concentrations of lithium perchlorate ($LiClO_4$). The effects of addition of either H^+ or Li^+ were qualitatively similar. With addition of these ions, the peaks in the CV spectra shifted to more positive potentials and the one-electron waves also merged into two-electron waves [17]. The details, however depended on both the cation identity and the POM anion. For $PMo_{12}O_{40}^{3-}$, three one-electron peaks changed to three two-electron peaks as the H^+ concentration increased or were consolidated into two peaks when the Li^+ concentration was increased [17]. For $PW_{12}O_{40}^{3-}$, four one-electron peaks merged into two two-electron peaks as the H^+ concentration was increased; as Li^+ increased the first two one-electron waves converged. Based on those results, it is apparent that increasing H^+ or Li^+ in general causes redox peaks to merge and shift to more positive potentials.

In these two literature examples, the proton and POM concentrations were varied independently, and the changes in CV spectra were attributed to the variation of proton concentration [16,17]. In the present experiments, the proton concentration varied in tandem with the POM anion concentration. Maeda [16] explained the two electron couples observed at higher acid concentrations in terms of reaction steps involving addition of two protons to the POM, and suggested that these are limited at low proton concentrations. Following this reasoning, we therefore carried out measurements at low POM concentration.

This work aims to show the differences in redox behavior of different polyoxometalates. Therefore, all CVs were obtained at concentrations of 0.5mM of POM and 100mM LiTf (Lithium trifluoromethanesulfonate) supporting electrolyte in acetonitrile, except as noted. A scan rate of 100mV/s was used throughout, except as noted. By utilizing salts of both the active POM species and the promoter electrolyte, proton concentration effects and redox couples involving protons were avoided. The experiments were all run in air, however some experiments were also run in a glovebox. These showed the same electrochemical behavior compared to experiments in air, demonstrating that the CV peaks observed were not associated with the reduction of oxygen.

Group IA (Li, Na) and IIA (Mg, Ca) salts of $CcPMo_{12}O_{40}$ (Cc represents the counter cation) were synthesized and the CV spectra shown in Figure 2-4 were obtained. The solubility of $K_3PMo_{12}O_{40}$ in acetonitrile was found to be too low so it was not examined further. In general, spectra for IA or IIA phosphomolybdate salts showed three redox couples, but the peak positions were slightly different. The effects of IA or IIA cations on cell potentials were fairly minor. $Li_3PMo_{12}O_{40}$ (E_{mid} = -0.17, -0.49 and -1.05 V) and $Na_3PMo_{12}O_{40}$ (E_{mid} = -0.15, -0.46 and -1.01 V) showed similar results, with three main redox peaks. The first and second peaks from the positive right side were reversible but the third peaks were both quasi-reversible. Peak separations can be utilized to distinguish different rate controlling processes of redox steps. Wider peak separation (ΔE) indicates slower kinetic processes for species in solution. For separations <0.059V and $i_{pa}/i_{pc} = 1$, the reaction is defined as ideal. Here most of the couples observed exhibited $\Delta E > 0.059V$ and those are characterized as quasi-reversible reactions for which the diffusion rate is greater than the reaction rate. Different scan rates (10mV, 50mV, 100mV and 200mV) and electrochemical impedance spectroscopy (EIS), were also run to check the resistance of the system to make sure that the separation was not caused by IR drop. The resistances measured were between 125 and 800 Ω which means that IR drop can affect the peak voltages in CV by at most 7mV. Since this is much less than the peak separation observed, the origin of these separations must be due to kinetics.

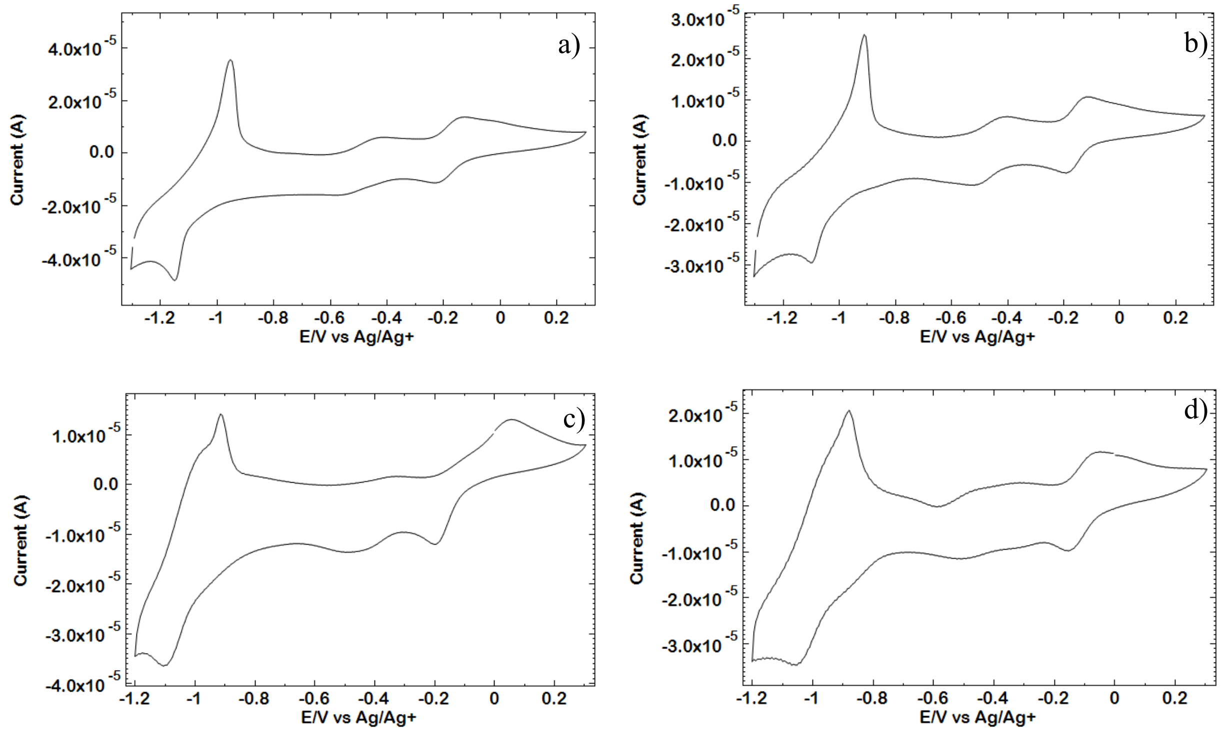

Figure 2-4 Cyclic voltammograms in acetonitrile for 0.5mM a) $Li_3PMo_{12}O_{40}$, b) $Na_3PMo_{12}O_{40}$, c) $Mg_{1.5}PMo_{12}O_{40}$ and d) $Ca_{1.5}PMo_{12}O_{40}$ with 100mM LiTf, 100mV/s

CV spectra of $Mg_{1.5}PMo_{12}O_{40}$ and $Ca_{1.5}PMo_{12}O_{40}$ salts also showed three quasi-reversible peaks. $Mg_{1.5}PMo_{12}O_{40}$ exhibited quasi-reversible behaviour for all three peaks, while $Ca_{1.5}PMo_{12}O_{40}$ gave rise to more reversible peaks compared to $Mg_{1.5}PMo_{12}O_{40}$. Again these reversible or quasi-reversible features are indicative of the controlling mechanisms of the different redox steps, but the details require further investigation.

In our experiments the relative rates of redox processes from high to low potential for the materials shown in Figure 2-2 can be summarized as: $PMo_{12}O_{40}^{3-} \leftrightarrow PMo_{12}O_{40}^{4-} \approx PMo_{12}O_{40}^{4-} \leftrightarrow PMo_{12}O_{40}^{5-} > PMo_{12}O_{40}^{5-} \leftrightarrow PMo_{12}O_{4}^{6-}$ (from positive side to negative side), based on the width of the three couples, with similar trends observed for the sodium analog, $Na_3PMo_{12}O_{40}$.

Given the fact that the experiments described above were carried out at LiTf:POM ratios of 200:1, it is possible that some or all of the POM counter cations may have exchanged with those of the support electrolyte. In order to explore this possibility, we carried out a limited number of CV measurements using NaTf as the support. These are compared with the corresponding spectra using LiTf in Figure 2-5. As shown in Figures 2-5 (a) and (b), the peaks corresponding to the first 1-electron reduction appeared at essentially the same potential (-0.185 V ± 0.007V) for all Li and Na combinations (i.e., LiTf+$Li_3PMo_{12}O_{40}$, NaTf+$Na_3PMo_{12}O_{40}$, LiTf+$Li_3PMo_{12}O_{40}$, NaTf+$Na_3PMo_{12}O_{40}$). However, the second peak for both $Li_3PMo_{12}O_{40}$ and $Na_3PMo_{12}O_{40}$ was dependent on the choice of Li or Na salts for the support electrolyte, suggesting that these cations may exchange readily. In contrast, for the IIA POM salts ($Mg_{1.5}PMo_{12}O_{40}$ and $Ca_{1.5}PMo_{12}O_{40}$,) almost no effect on peak positions was observed when LiTf was replaced by NaTf, suggesting that these Group IIA cations are not readily exchanged with those of the support.

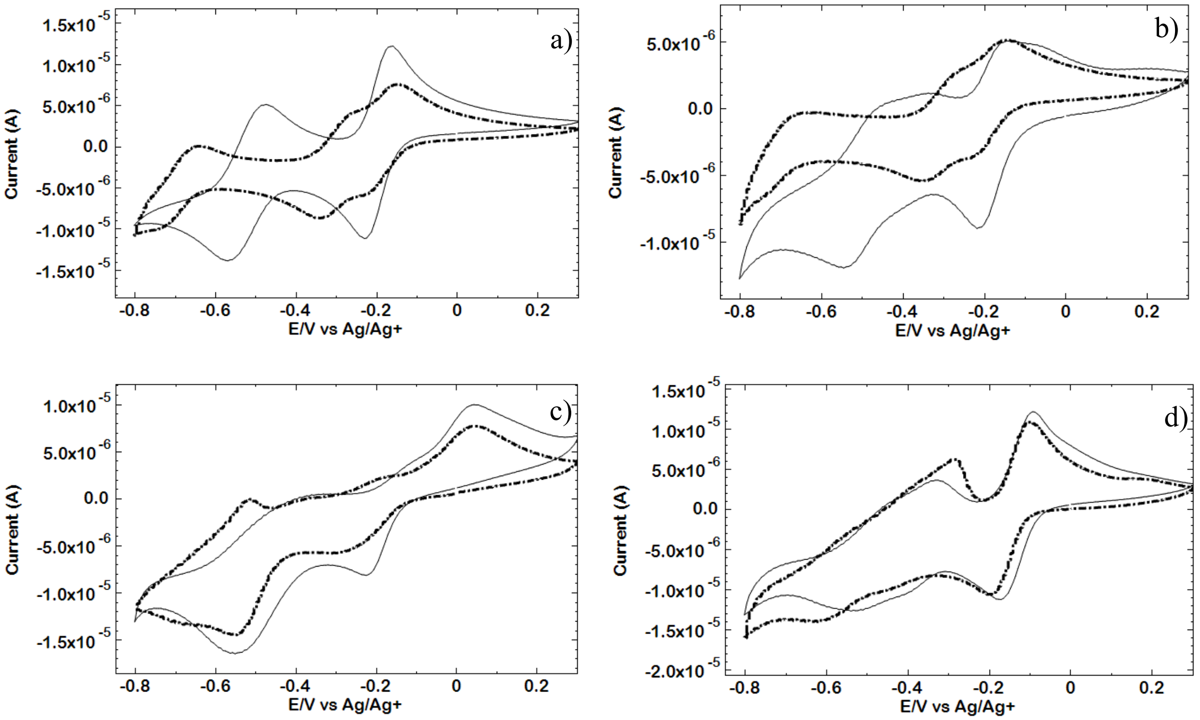

Figure 2-5 Cyclic voltammograms for 0.5mM POMs in acetonitrile with 100mM LiTf (line) or NaTf (thick dot-line) supports. a) $Li_3PMo_{12}O_{40}$, b) $Na_3PMo_{12}O_{40}$, c) $Mg_{1.5}PMo_{12}O_{40}$ and d) $Ca_{1.5}PMo_{12}O_{40}$, 100mV/s

LiTf was therefore chosen as the support electrolyte for all subsequent experiments and Li salts were used exclusively. The advantages of this choice are that Li is the smallest counter cation, and the Li POM salts display the highest solubilities. Further, by utilizing POM salts rather than the acid forms, H_2 generation was avoided.

2.3.2 Heteroatom exchanged POMs: ($Li_3PMo_{12}O_{40}$, $Li_3AsPMo_{12}O_{40}$, $Li_4SiMo_{12}O_{40}$, $Li_3PW_{12}O_{40}$, $Li_4SiW_{12}O_{40}$)

The influence of different heteroatoms (X = phosphorus, arsenic and silicon) on POM CV behavior in acetonitrile was investigated for both $Li_cXMo_{12}O_{40}$ and $Li_cXW_{12}O_{40}$ compounds. CV spectra for $Li_3PMo_{12}O_{40}$, $Li_3AsPMo_{12}O_{40}$, and $Li_4SiMo_{12}O_{40}$ are compared in Figure 2-6.

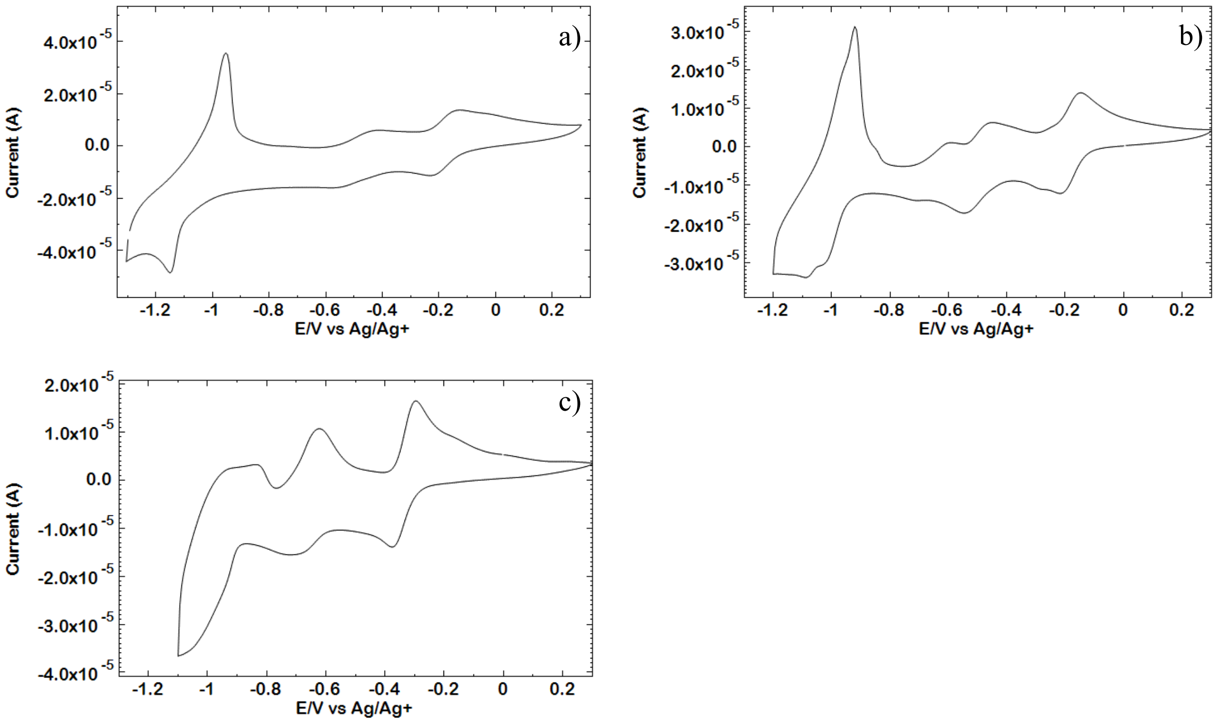

Figure 2-6 Cyclic voltammograms in acetonitrile for 0.5mM a) $Li_3PMo_{12}O_{40}$, b) $Li_3AsMo_{12}O_{40}$, c) $Li_4SiMo_{12}O_{40}$ with 100mM LiTf, 100mV/s

All three compounds exhibited three redox couples. Peak potentials for heteroatoms in the same VA group (P and As), were similar. Si, in the IVA group, gives POMs with one more negative charge, and the peaks for this compound are shifted to more negative potentials relative to the others. Similar observations were reported for aqueous POMs by Sadakane and Steckhan [3]. In the literature results, the negative charge density of the substituted Keggin ions affected

the first and second redox peak potentials, following the order $SMo_{12}O_{40}^{2-}$ > $PMo_{12}O_{40}^{3-}$ >
b)
$SiMo_{12}O_{40}^{4-}$.

As shown in Figure 2-6, compared to $Li_3PMo_{12}O_{40}$, for $Li_4SiMo_{12}O_{40}$ the first redox couple from the positive right side was 0.3 V more negative (in ACN), which is similar to the trend in aqueous solution [3,18,19]. The peak positions observed were as follows: $Li_3PMo_{12}O_{40}$ (E_{mid} = -0.17, -0.49 and -1.05 V), $Li_3AsMo_{12}O_{40}$ (E_{mid} = -0.18, -0.50, -0.66 and -0.97 V) and $Li_4SiMo_{12}O_{40}$ (E_{mid} = -0.34, -0.66 and -0.93 V.) These results are consistent with previous observations that the reduction potentials of one-electron waves decrease linearly with a decrease in the valence of the heteroatom for Keggin-type heteropolyanions [3]. Himeno and Takamoto [18] have explained these shifts in terms of changes in the surface charge density of the heteropolyanions with different heteroatoms.

Tungsten POMs were also examined in this study. $Li_3PW_{12}O_{40}$ (E_{mid} = -0.60, -0.87, -1.13), $Li_4SiW_{12}O_{40}$ (E_{mid} = -0.88 and -1.15), showed two to three redox peaks in ACN (Figure 2-7), again following the same trend reported for aqueous systems [3,18]. The first $Li_4SiW_{12}O_{40}$ redox couple was 0.3 V more negative than that for $Li_3PW_{12}O_{40}$ in both water and acetonitrile. This difference can again be ascribed to the different POM charges.

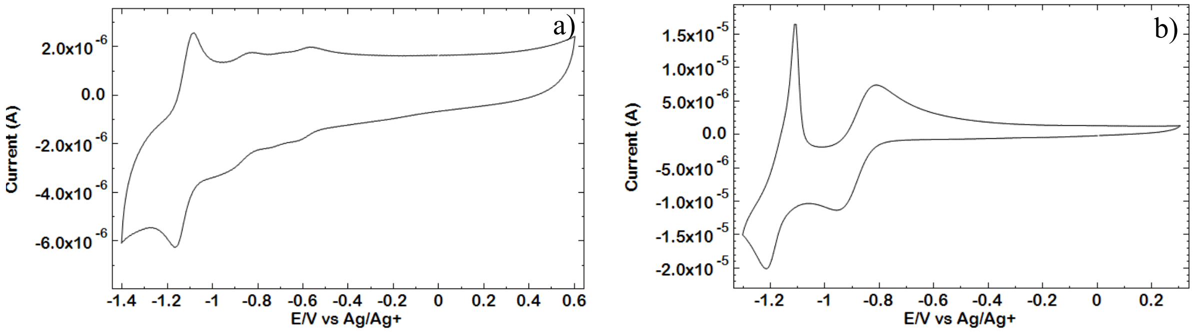

Figure 2-7 Different 0.5mM $Li_cXW_{12}O_{40}$ cyclic voltammograms, a) $Li_3PW_{12}O_{40}$, b) $Li_4SiW_{12}O_{40}$, with 100mM LiTf, 100mV/s

$Li_4SiW_{12}O_{40}$ was observed to be unstable at more negative potentials (< -1.3V) therefore only two peaks representing the voltage range over which this compound was stable are shown.

The reason for this shift is likely the higher negative charge density on the POM, which renders reduction more difficult.

Even though heteroatom charge affects the first and second redox potentials, the number of peaks for all POMs remained similar. This suggests that the POMs cannot be easily altered to receive more electrons by changing the heteroatom elements among X = P, As, Si. Further, the stability in acetonitrile may also vary with the identity of the central heteroatom.

2.3.3 Variation of framework metal atoms: ($Li_3PMo_{12}O_{40}$, $Li_3PW_{12}O_{40}$, $Li_3PMo_6W_6O_{40}$, $Li_4PMo_{11}VO_{40}$)

$Li_3PMo_{12}O_{40}$ (E_{mid} = -0.17, -0.49 and -1.05 V) and $Li_3PW_{12}O_{40}$ (E_{mid} = -0.60, -0.87, -1.13), cyclic voltammograms are shown in Figures 2-6(a) and Figure 2-7(a), respectively. Unlike heteroatom-exchanged POMs, changing the framework metal elements does change the redox behavior, which includes both the position and number of peaks. Similar results were also found in previous studies in 1,2-dichloro ethane and dimethyl sulfoxide (DMSO) [21]. As shown in Figure 2-8, the CV spectrum for $Li_3PMo_6W_6O_{40}$ exhibited 4 peaks with E_{mid} = -0.04, -0.35, -0.60 and -0.95V. While not particularly well resolved, it is apparent that the peaks in the CV spectrum of the Mo-W mixed framework compound are not located at intermediate potentials between the three one-electron waves for $Li_3PMo_{12}O_{40}$ and $Li_3PW_{12}O_{40}$.

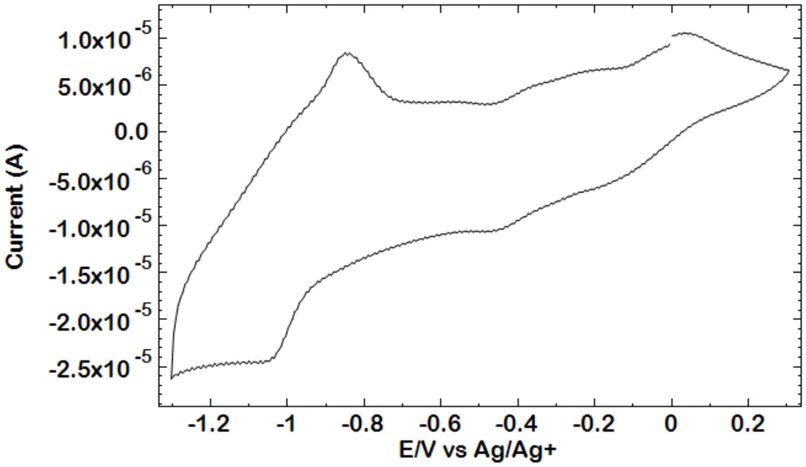

Figure 2-8 Cyclic voltammogram in acetonitrile for 0.5mM $Li_3PMo_6W_6O_{40}$ with 100mM LiTf, 100mV/s

CV spectra for $Li_4PMo_{11}VO_{40}$ (E_{mid} = 0.530, 0.327, 0.184, -0.074 and -0.232 V), mixed addenda POMs are compared in Figure 2-9. $Li_4PMo_{11}VO_{40}$ exhibited five redox couples. The redox processes were quasi-reversible. In aqueous solution [5], $H_{3+x}PMo_{12-x}V_xO_{40}$ compounds show multiple redox peaks compared to $H_3PMo_{12}O_{40}$. Our results for lithium salts in acetonitrile were similar. It should be noted, however, that the first reduction potential of the vanadium-substituted compound occurs at more positive potentials compared to $PMo_{12}O_{40}$ in either aqueous or acetonitrile media.

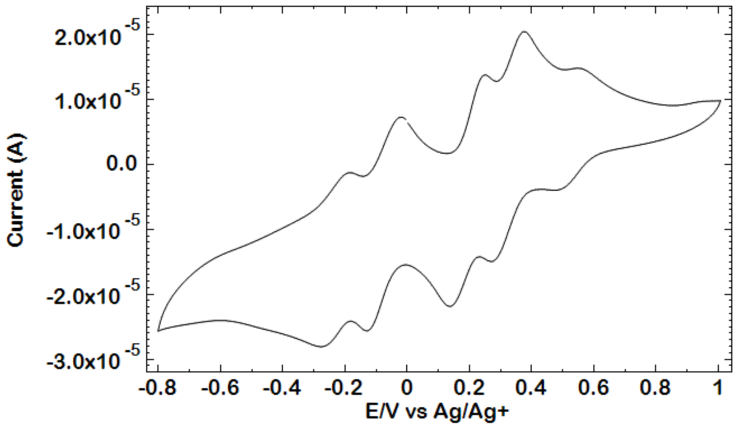

Figure 2-9. Cyclic voltammogram in acetonitrile for 0.5mM $Li_4PMo_{11}VO_{40}$ with 100mM LiTf, 100mV/s

2.3.4 Comparison of POM redox properties in aqueous and acetonitrile solution

Redox potentials for the acid forms of polyoxometalates in aqueous solution are compared with those for the corresponding lithium salts in acetonitrile in Table 1. In some cases, peak potentials were extracted from aqueous cyclic voltammetry spectra in the literature where specific numerical values were not given. The overall cyclic voltammetry results in acetonitrile solution can be estimated from the aqueous data for the relative redox couple potential and the number of couples. In general, the POMs exhibit similar trends in aqueous solution and in acetonitrile, taking into account the difference in reference electrodes used in the two media. Figure 2-10 illustrates the correlation between redox couples for the acid form of POMs in aqueous solution and for lithium salts of POMs in acetonitrile. For all of the POMs studied except $PMo_{11}VO_{40}$, there is a linear correlation of all redox couples in ACN with those reported in water, with a slope of unity. For each of the POMs examined, results for two to four couples are included in the figure. Thus, the linear correlation indicates that the separation between redox couples for each POM are the same in ACN as in water. The offset (y-axis intercept) for this correlation is about -0.6 volts, which represents the cumulative effect of the differences in solvent, support electrolyte, and reference electrodes between the measurements in ACN and water. For $PMo_{11}VO_{40}$, the slope of the correlation is also unity, indicating common separations between the first, second and third redox couples in ACN and water. However, the offset is nearly 0.2 volts. The origin of this difference is unclear, but it does suggest that an asymmetric RFB with framework-substituted POMs might be capable of operating over a wider voltage range in acetonitrile than in aqueous media. In any case, the present work suggests that the large library of POM electrochemistry in aqueous solution may provide a guide to POM redox behavior in non-aqueous applications, including redox flow batteries.

Table 2-1: Comparison of POM reduction potentials in water and acetonitrile

Aqueous (SCE)	E1/V	E2/V	E3/V	E4/V		Ref	Acetonitrile (Ag/Ag$^+$)	E1/V	E2/V	E3/V	E4/V	E5/V
							0.5mM POM w/ 0.1M LiTf	(i_{pa}/i_{pc})	(i_{pa}/i_{pc})	(i_{pa}/i_{pc})	(i_{pa}/i_{pc})	(i_{pa}/i_{pc})
$H_3PMo_{12}O_{40}$	0.36	0.24	0.01		1mM POM w/ 0.5M H_2SO_4 in1:1 Water-Dioxane	[22]	$Li_3PMo_{12}O_{40}$	-0.17	-0.49	-1.05		
								(0.73)	(0.63)	(0.12)		
							$Na_3PMo_{12}O_{40}$	-0.15	-0.46	-1.01		
								(0.93)	(1.08)	(0.43)		
							$Mg_{1.5}PMo_{12}O_{40}$	-0.08	-0.4	-1.05		
								(0.10)	(1.15)	(0.25)		
							$Ca_{1.5}PMo_{12}O_{40}$	-0.11	-0.5	-0.96		
								(0.81)	(0.17)	(0.25)		
$H_3PW_{12}O_{40}$	-0.004	-0.27	-0.62		1mM POM w/ 0.5M H_2SO_4 in1:1 Water-Dioxane	[22]	$Li_3PW_{12}O_{40}$	-0.60	-0.87	-1.13		
								(0.96)	(1.12)	(0.70)		
$H_4PMo_{11}VO_{40}$	0.40	0.23	0.01		w/1 M	[23]	$Li_4PMo_{11}VO_{40}$	0.53	0.32	0.18	-0.07	-0.23
					$HClO_4$			(1.79)	(0.60)	(1.71)	(0.83)	(1.05)
$H_5PMo_{10}V_2O_{40}$	0.40	0.24	0.01		w/1 M	[23]						
					$HClO_4$							
$H_6PMo_9V_3O_{40}$	0.40	0.23	0.02		w/1 M	[23]						
					$HClO_4$							
							$Li_3PMo_6W_6O_{40}$	-0.04	-0.35	-0.6	-0.95	
								(0.55)	(1.44)	(0.58)	(0.63)	
$H_3AsMo_{12}O_{40}$	0.30	0.16	0.00	-0.19	1mM POM w/ 0.5M H_2SO_4 in1:1 Water-Dioxane	[24]	$Li_3AsMo_{12}O_{40}$	-0.18	-0.5	-0.66	-0.97	
								(0.80)	(1.29)	(0.24)	(0.23)	
$H_4SiMo_{12}O_{40}$	0.23	0.05	-0.38	-0.5	-	[25]	$Li_4SiMo_{12}O_{40}$	-0.34	-0.66	-0.93		
								(0.63)	(0.34)	(0.89)		
$H_4SiW_{12}O_{40}$	-0.2	-0.41	-0.56		1mM POM w/	[26]	$Li_4SiW_{12}O_{40}$	-0.88	-1.15			
					1M $HClO_4$			(0.76)	(0.32)			

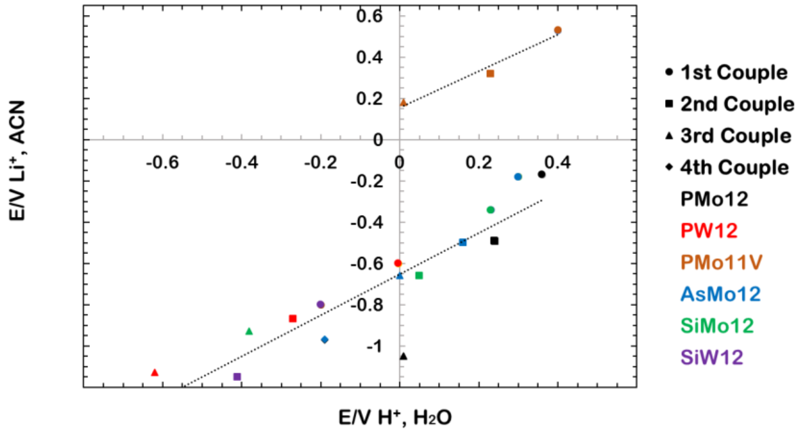

Figure 2-10 Correlation of the voltages of redox couples measured in acetonitrile for lithium salts of POMs vs. reported values for the corresponding acids in aqueous solution. Reference electrodes are as specified in Table 2-1. The oxygen in the POM frameworks (O_{40} in all cases) has been omitted in the inset legend.

2.4 Conclusions

Cyclic voltammetry of molybdenum and tungsten-containing Keggin-structure polyoxometalates was carried out in acetonitrile with LiTf as support electrolyte.

Variations with respect to counter-cation, heteroatom, and metal framework atoms in these POMs were examined. No significant differences in overall redox properties were observed when Group IA and IIA counter-cations were exchanged. Variation of heteroatoms among P, As, and Si showed that charge affects reduction potentials but not redox processes. The more negative the charge on the POM, the more negative the potentials of its redox couples. The framework metal elements play the most important role in determining in the redox properties. The Mo, W, and V-containing POMs show substantially different properties with respect to the number and potential of the redox couples. Reduction potentials for the Li-POM salts in acetonitrile and the corresponding heteropolyacids in aqueous solution were relatively well correlated.

2.5 References

[1] Pope, M. T., & Müller, A. (1991). Polyoxometalate chemistry: an old field with new dimensions in several disciplines. *Angewandte Chemie International Edition*, *30*(1), 34-48.

[2] Müller, A., Peters, F., Pope, M. T., & Gatteschi, D. (1998). Polyoxometalates: very large clusters nanoscale magnets. *Chemical Reviews*, *98*(1), 239-272.

[3] Sadakane, M., & Steckhan, E. (1998). Electrochemical properties of polyoxometalates as electrocatalysts. *Chemical Reviews*, *98*(1), 219-238.

[4] Barteau, M. A., Lyons, J. E., & Song, I. K. (2003). Surface chemistry and catalysis on well-defined oxide surfaces: nanoscale design bases for single-site heterogeneous catalysts. *Journal of Catalysis*, *216*(1), 236-245.

[5] Song, I. K., & Barteau, M. A. (2004). Redox properties of Keggin-type heteropolyacid (HPA) catalysts: effect of counter-cation, heteroatom, and polyatom substitution. *Journal of Molecular Catalysis A: Chemical*, *212*(1), 229-236.

[6] Weber, A. Z., Mench, M. M., Meyers, J. P., Ross, P. N., Gostick, J. T., & Liu, Q. (2011). Redox flow batteries: a review. *Journal of Applied Electrochemistry*, *41*(10), 1137-1164.

[7] De Leon, C. P., Frías-Ferrer, A., González-García, J., Szánto, D. A., & Walsh, F. C. (2006). Redox flow cells for energy conversion. *Journal of Power Sources*, *160*(1), 716-732.

[8] Shin, S. H., Yun, S. H., & Moon, S. H. (2013). A review of current developments in non-aqueous redox flow batteries: characterization of their membranes for design perspective. *RSC Advances*, *3*(24), 9095-9116.

[9] Wang, H., Hamanaka, S., Nishimoto, Y., Irle, S., Yokoyama, T., Yoshikawa, H., & Awaga, K. (2012). In operando X-ray absorption fine structure studies of polyoxometalate molecular cluster batteries: polyoxometalates as electron sponges. *Journal of the American Chemical Society*, *134*(10), 4918-4924.

[10] Long, D. L., Tsunashima, R., & Cronin, L. (2010). Polyoxometalates: building blocks for functional nanoscale systems. *Angewandte Chemie International Edition*, *49*(10), 1736-1758.

[11] Thistlethwaite, W. P. (1966). The “normal” 12-molybdophosphates of the alkali metals and ammonium. *Journal of Inorganic and Nuclear Chemistry*, *28*(10), 2143-2146.

[12] Hayashi, H., & Moffat, J. B. (1983). Methanol conversion over metal salts of 12-tungstophosphoric acid. *Journal of Catalysis*, *81*(1), 61-66.

[13] Tsigdinos, G. A. (1974). Preparation and characterization of 12-molybdophosphoric and 12-molybdosilicic acids and their metal salts. *Industrial & Engineering Chemistry Product Research and Development*, *13*(4), 267-274.

[14] Mabbott, G. A. (1983). An introduction to cyclic voltammetry. *Journal of Chemical Education*, *60*(9), 697.

[15] Bard, A. J., L. R. Faulkner. (2001). *Electrochemical Methods: Fundamentals and Applications, 2nd ed.* New York, NY: John Wiley & Sons, Inc.

[16] Maeda, K., Himeno, S., Osakai, T., Saito, A., & Hori, T. (1994). A voltammetric study of Keggin-type heteropolymolybdate anions. *Journal of Electroanalytical Chemistry*, *364*(1-2), 149-154.

[17] Himeno, S., & Takamoto, M. (2002). Difference in voltammetric properties between the Keggin-type $[XW_{12}O_{40}]^{n-}$ and $[XMo_{12}O_{40}]^{n-}$ complexes. *Journal of Electroanalytical Chemistry*, *528*(1), 170-174.

[18] Himeno, S., Takamoto, M., & Ueda, T. (2000). Cation effects on the voltammetric behavior of α-Keggin-type $[SiMo_{12}O_{40}]^{4-}$ and $[PMo_{12}O_{40}]^{3-}$ complexes in CH_3COCH_3 and CH_3CN. *Journal of Electroanalytical Chemistry*, *485*(1), 49-54.

[19] Altenau, J. J., Pope, M. T., Prados, R. A., & So, H. (1975). Models for heteropoly blues. Degrees of valence trapping in vanadium (IV)-and molybdenum (V)-substituted Keggin anions. *Inorganic Chemistry*, *14*(2), 417-421.

[20] Pope, M. T., & Varga Jr, G. M. (1966). Heteropoly blues. I. Reduction stoichiometries and reduction potentials of some 12-tungstates. *Inorganic Chemistry*, *5*(7), 1249-1254.

[21] Maeda, K., Katano, H., Osakai, T., Himeno, S., & Saito, A. (1995). Charge dependence of one-electron redox potentials of Keggin-type heteropolyoxometalate anions. *Journal of Electroanalytical Chemistry*, *389*(1-2), 167-173.

[22] Keita, B., & Nadjo, L. (1989). New oxometalate-based materials for catalysis and electrocatalysis. *Materials chemistry and physics*, *22*(1-2), 77-103.

[23] Limoges, B. R., Stanis, R. J., Turner, J. A., & Herring, A. M. (2005). Electrocatalyst materials for fuel cells based on the polyoxometalates $[PMo_{(12-n)}V_nO_{40}]^{(3+n)-}$ (n= 0–3). *Electrochimica acta*, *50*(5), 1169-1179.

[24] Eguchi, K., Seiyama, T., Yamazoe, N., Katsuki, S., & Taketa, H. (1988). Electronic structures of $XMo_{12}O_{40}$ heteropolyanions (X= P, As, Si, and Ge) and their reduction behavior. *Journal of Catalysis*, *111*(2), 336-344.

[25] Fruchart, J. M., Herve, G., Launay, J. P., & Massart, R. (1976). Electronic spectra of mixed valence reduced heteropolyanions. *Journal of Inorganic and Nuclear Chemistry*, *38*(9), 1627-1634.

[26] Keita, B., & Nadjo, L. (1987). New aspects of the electrochemistry of heteropolyacids: Part II. Coupled electron and proton transfers in the reduction of silicotungstic species. *Journal of Electroanalytical Chemistry and Interfacial Electrochemistry*, *217*(2), 287-304.

Chapter 3

Characterization of Polyoxometalate Samples

3.1 Experimental techniques and their application

In order to perform redox flow battery experiments, a fundamental study of the relevant polyoxometalate materials was needed. These studies included solubility measurements in non-aqueous solvents, thermal gravimetric analysis (TGA), X-Ray Diffraction (XRD), Fourier transform infrared spectroscopy (FTIR), and stability testing by BE (bulk electrolysis).

Solubility measurements were used for estimating the maximum energy density of the redox flow battery. Ultraviolet–visible spectroscopy (UV-Vis) was used for some of the solubility measurements. The principle of UV-Vis measurements is the Beer-Lambert law:

$$A=\varepsilon Cl$$

with parameters defined as A: absorbance, ε: molar attenuation coefficient, C: concentration of the species and l: path length specific to the instrument used for measurement. The molar attenuation coefficient is related to the possibility of the electronic transition. In this section, the effects of IA and IIA group counter-cations on solubility were investigated. A range of different polyoxometalates was tested.

$H_3PMo_{12}O_{40}$, $Li_3PMo_{12}O_{40}$, $Na_3PMo_{12}O_{40}$, $Mg_{1.5}PMo_{12}O_{40}$ salts were measured with an Implen P300 UV-Visible Nanophotometer, and other POM salts shown in Figure 3-1 were measured by weight percent measurements. Saturated POM solution was prepared by portion-wise addition of POM to 1 mL of acetonitrile with stir bar stirring until a solid suspension was observed. After this saturated POM solution was prepared, the solution was pretreated with the same procedure shown in [5]. The saturated POM solution was then centrifuged with an Eppendorf 5415C centrifuge at 8000 rpms for 20 minutes and the clear supernatant liquid was removed for measurement. The 309 nm wavelength was picked for measurements in the UV-vis experiments, which corresponds to an O → M band transition [6]. Before the saturated solution was measured by UV-vis, a standard calibration was obtained for POM solutions prepared at lower known concentrations. Saturation values for other POM solutions were obtained by evaporating a saturated solution to dryness and measuring the POM mass remaining.

TGA was used to measure the POM water content. Typically, a hydrated Keggin heteropolyacid can contain around 15 to 25 water molecules per POM in the solid state [1][2]. In this research, the POMs were stored in a vacuum desiccator at room temperature for periods longer than three weeks. TGA analysis was used to determine how many water molecules remained. TGA measures the mass of the material lost or gained while the temperature increases or decreases against time. The mass may change due to decomposition, dehydration or chemical reaction.

TGA was performed using a TA Q50 TGA instrument. TGA experiments were performed under a steady flow of helium at 90 mL/min. The temperature started at 30 °C followed by a 15°C per minute ramp to 300 °C and subsequent cooling to room temperature. The temperature limit was set at 300 °C, as the water loss below this temperature could be correlated with the existence of intermediary hydrateforms of the respective acids $H_3PMo_{12}O_{40}$, $H_3PW_{12}O_{40}$ and $H_4PMo_{11}VO_{40}$. At higher temperatures, water loss is associated with reduction and loss of the Keggin structure [7][8].

XRD was used verify the crystal structure of our materials. This technique relies on Bragg's Law:

$$2d\sin\theta = n\lambda$$

where d is the space distance between the diffracting plane, θ is the incident angle and λ is the wavelength of the x-ray applied. According to Bragg's Law, at a given incident angle, only X-rays scattered from atoms or molecules of a specific spacing will constructively interfere and therefore be detected.

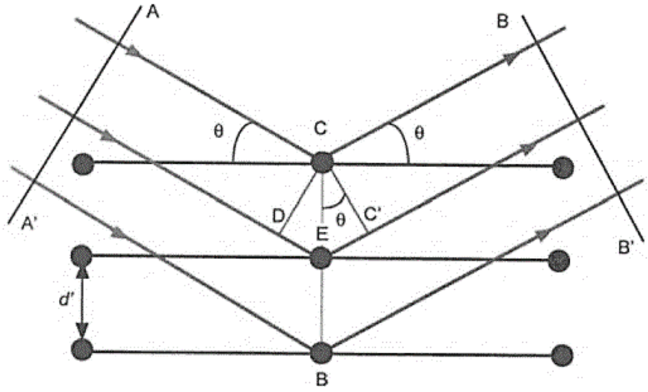

Figure 3-1 Diffraction of X-ray by a crystal [3]

A Rigaku Miniflex XRD instrument was used for bulk POM structural analysis. The 2θ range sampled was from 10° to 90°, with a step size of 0.1° and a step time of 1 second. All samples were ground into fine powder before measurement.

FTIR was performed with Attenuated total reflectance (ATR) FTIR (FT/IR-4100 Jasco) in air. Spectra of electrolyte solutions were measured at wavelengths between 600 cm^{-1} to 4000 cm^{-1}. FTIR was used to confirm POM stability before and after electrochemical experiments. FTIR can be used to measure the sample in solid, liquid or gas phases by absorption or emission spectroscopy. In this research, Attenuated Total Reflectance (ATR) FTIR was used. The infrared light was applied to the ATR crystal and the infrared light was reflected from the interface with the sample. ATR is easily used with the solid and liquid samples.

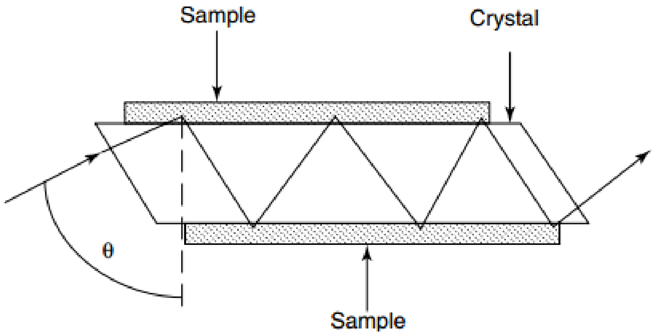

Figure 3-2 Schematic of a typical Attenuated Total Reflectance FTIR [4]

Bulk electrolysis is a form of coulometry with a constant voltage or current held for a defined period of time. The material can be oxidized or reduced by bulk electrolysis. By monitoring the current, the number of electrons taken up via each oxidation or reduction step can be determined.

Bulk electrolysis experiments were carried out in a bulk electrolysis cell as described in chapter 2. The RVC working electrode consisted of carbon sheets with 60 pores per inch (ERG Aerospace). The reference used was Ag/Ag^+ quasi-reference electrode (QRE). The measurement was performed with 0.01 M POM with 0.1 M LiTf in acetonitrile. The POM solution was electrolyzed with 0.5 coulombs and the open circuit potential was then measured. This step was repeated until the amount of charge transferred reached the theoretical limit.

FTIR spectra of solutions bulk-electrolyzed to different OCP values in a water/oxygen free argon glovebox were obtained after quick transfer to the FTIR spectrometer in air

3.2 Results and Discussion

3.2.1 Solubility

The results of solubility measurements in acetonitrile are shown in Figure 3-3 below.

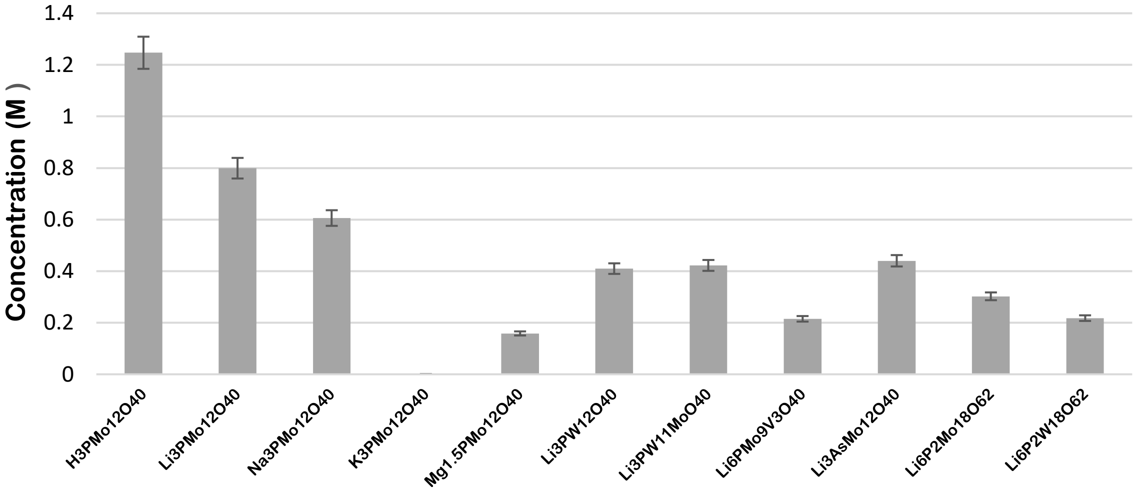

Figure 3-3 Solubility of POMs in acetonitrile

The solubility of $CcPMo_{12}O_{40}$ (Cc = H, Li, Na, K, Mg) decreases from H^+ to K^+ as the atomic weight and ion diameter increases in the IA group. $K_3PMo_{12}O_{40}$ was almost insoluble in acetonitrile, as previously found [9]. For POMs of different composition but with the same counter cation (Li^{+}), similar solubility behavior was found. Comparing POMS exhibiting different structures (Keggin and Dawson), the Keggin structures exhibited approximately twice the solubility of the Dawson structure POMs ($Li_3PMo_{12}O_{40}$ vs. $Li_6P_2Mo_{18}O_{62}$ and $Li_3PW_{12}O_{40}$ vs. $Li_6P_2W_{18}O_{62}$).

3.2.2 Thermogravimetric Analysis (TGA)

The vacuum-dried POMs were compared in order to quantify the amount of water of crystallization that can be removed without decomposing the POM structures at room temperature. The intermediate hydrates increase the overall weight of the POM • xH_2O compound; quantification of the water content was therefore important in order to prepare POM solutions of specific concentration.

TGA profiles of these compounds are shown below.

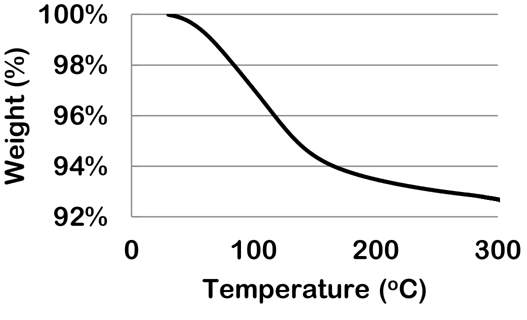

(a)

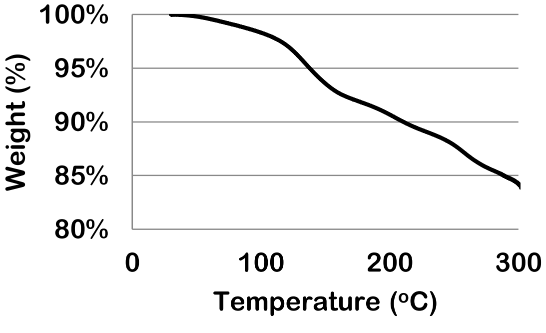

(b)

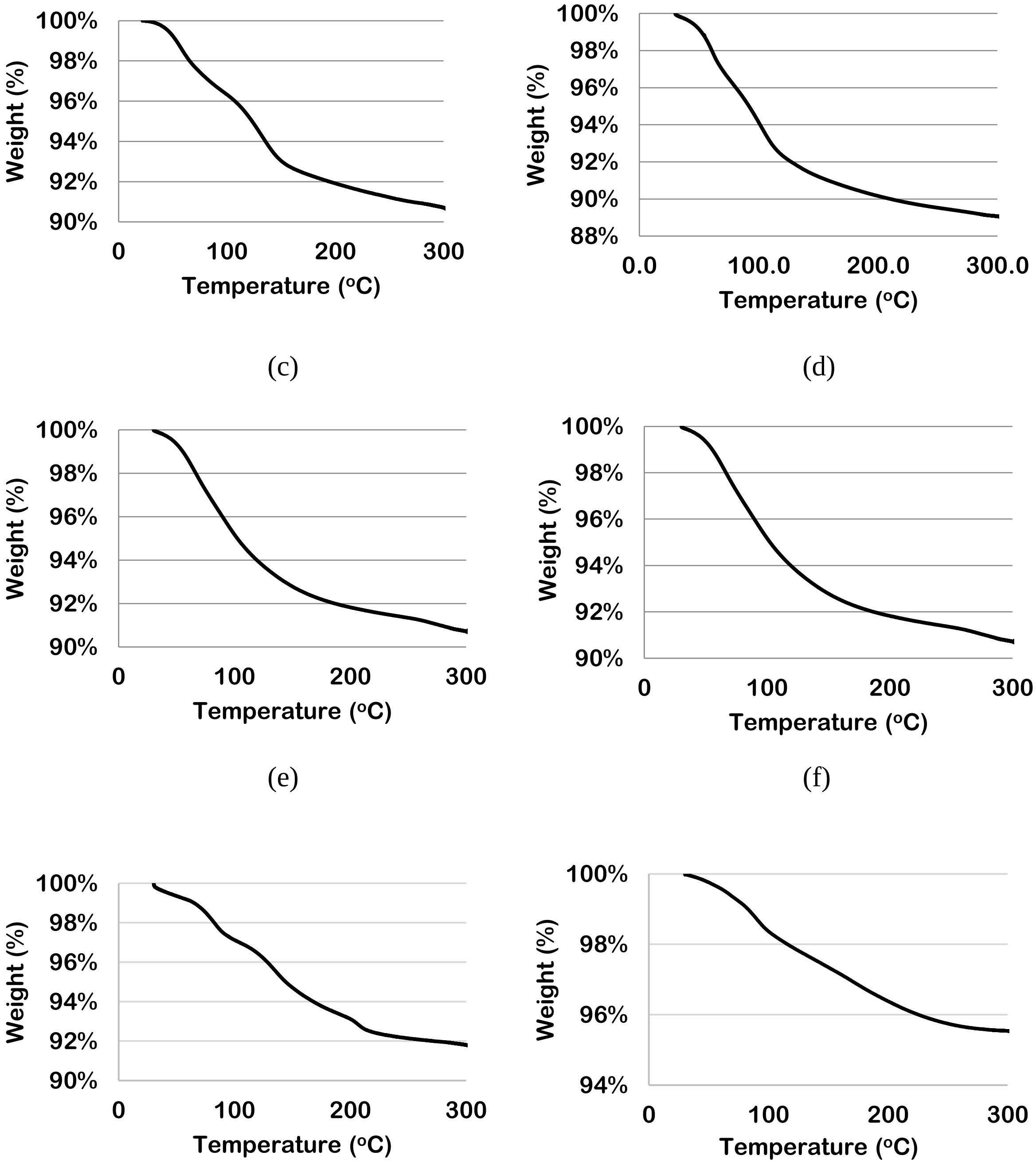

(c) (d)

(e) (f)

(g) (h)

Figure 3-4 TGA plots (a) $Li_3PMo_{12}O_{40}$ (b) $Li_3AsMo_{12}O_{40}$ (c) $Li_4SiMo_{12}O_{40}$ (d) $Li_4PMo_{11}VO_{40}$ (e) $Li_5PMo_{10}V_2O_{40}$ (f) $Li_6PMo_9V_3O_{40}$ (g) $Li_6P_2Mo_{18}O_{62}$ (h) $Li_6P_2W_{18}O_{62}$

The number of water molecules in each case was calculated by the weight loss from 30°C to 300°C. TGA results provided hydration levels of POMs stored under vacuum at room temperature. The intermediary hydrates numbers calculated by TGA were $Li_3PMo_{12}O_{40} \cdot 7H_2O$, $Li_3AsMo_{12}O_{40} \cdot 14H_2O$, $Li_4SiMo_{12}O_{40} \cdot 10\ H_2O$, $Li_4PMo_{11}VO_{40} \cdot 11\ H_2O$, $Li_5PMo_{10}V_2O_{40} \cdot 10H_2O$, $Li_6PMo_9V_3O_{40} \cdot 9\ H_2O$, $Li_6P_2Mo_{18}O_{62} \cdot 14\ H_2O$ and $Li_6P_2W_{18}O_{62} \cdot 11\ H_2O$. The vacuum-dried POM samples thus retained between 7 and 14 water molecules per POM. The air-stored Keggin polyoxometalates typically have 20 wt% water content, corresponding to around 20 ~ 25 water molecules per POM [10]. The vacuum-dried POM samples with fewer water molecules maintained stable POM structures, as shown by XRD and FTIR results below.

3.2.3 X-Ray Powder Diffraction (XRD)

Representative polyoxometalate XRD results are shown as below; these demonstrate the structural integrity of the samples.

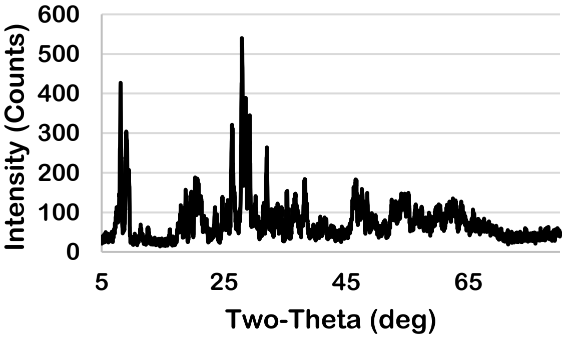

(a)

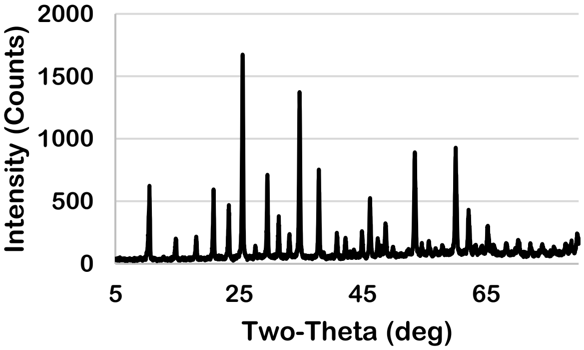

(b)

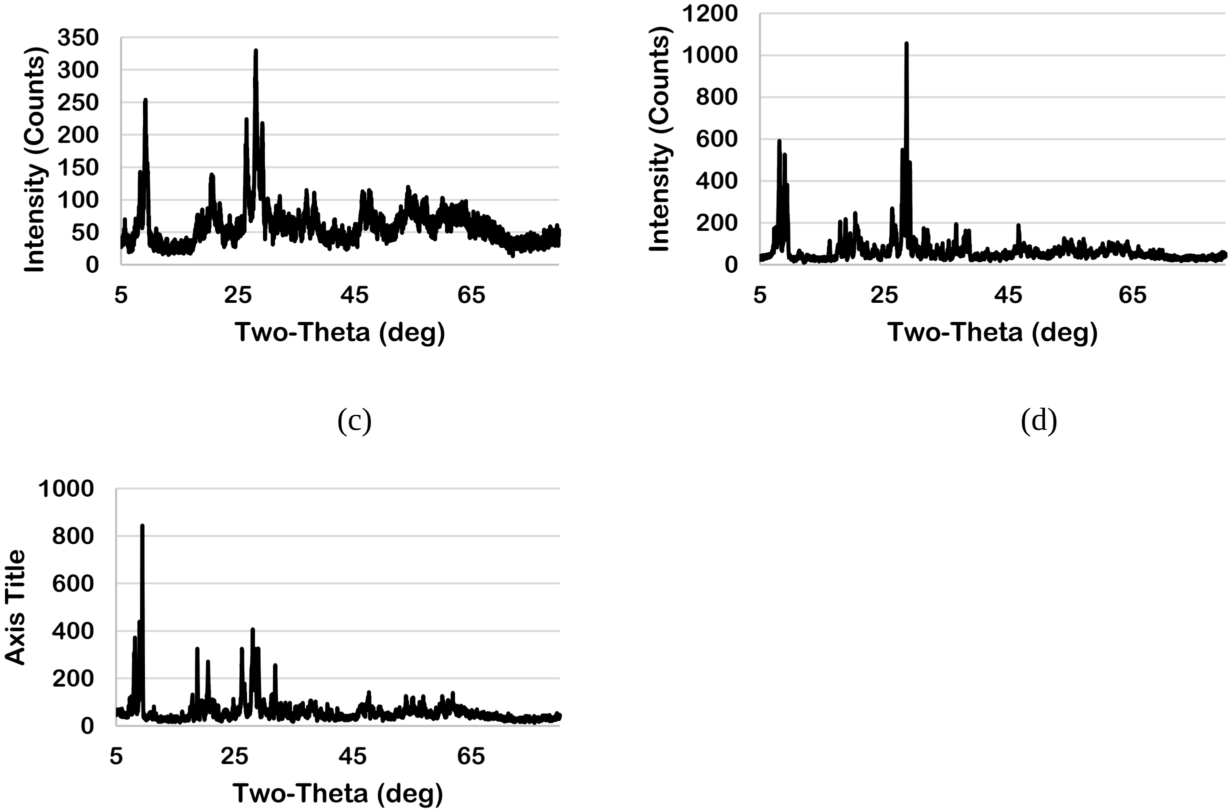

(c)

(d)

(e)

Figure 3-5 XRD pattern (a) $H_3PMo_{12}O_{40}$ (b) $H_3PW_{12}O_{40}$ (c) $H_4PMo_{11}VO_{40}$ (d) $H_5PMo_{10}V_2O_{40}$ (e) $H_6PMo_{10}V_3O_{40}$

The XRD patterns in Figure 3-5 of vacuum-dried $H_3PMo_{12}O_{40}$, $H_3PW_{12}O_{40}$, $H_4PMo_{11}VO_{40}$, $H_5PMo_{10}V_2O_{40}$, $H_6PMo_{10}V_3O_{40}$ were consistent with literature results. For $H_3PMo_{12}O_{40}$, $H_3PW_{12}O_{40}$ the results agreed well with those reported by Misono et al. [11] and Yang et al. [12]. It is worth mentioning that in the literature [11], the authors indicated the XRD pattern is a function of the extent of dehydration of the POM, indicating that POM spacing is affected by water content. The $H_4PMo_{11}VO_{40}$, $H_5PMo_{10}V_2O_{40}$, $H_6PMo_{10}V_3O_{40}$ results were compared with literature [13][14][15] and also found to be consistent.

3.2.4 Fourier transform infrared spectroscopy (FTIR)

3.2.4.1 $H_3PMo_{12}O_{40}$ vacuum-dried sample and sample stored in air (designated “wet”)

For $H_3PMo_{12}O_{40}$, FTIR spectra show peaks at 1051 cm^{-1} (P−O), 951 cm^{-1}(Mo=O$_t$), 877 cm^{-1} (Mo−O$_b$−Mo), and 741 cm^{-1} (Mo−O$_c$−Mo) [16]. The broad peak around 3100 cm^{-1}, indicative of O-H bonds, showed diminished intensity in the vacuum-dried materials relative to the air-stored (wet) POMs, as shown in Figure 3-6. The band near 1620 cm^{-1} is also indicative of the presence of H_2O (δ(OH) modes) and the broad peak between 3200~3600 cm^{-1} is indicative of the ν(OH) modes [17].

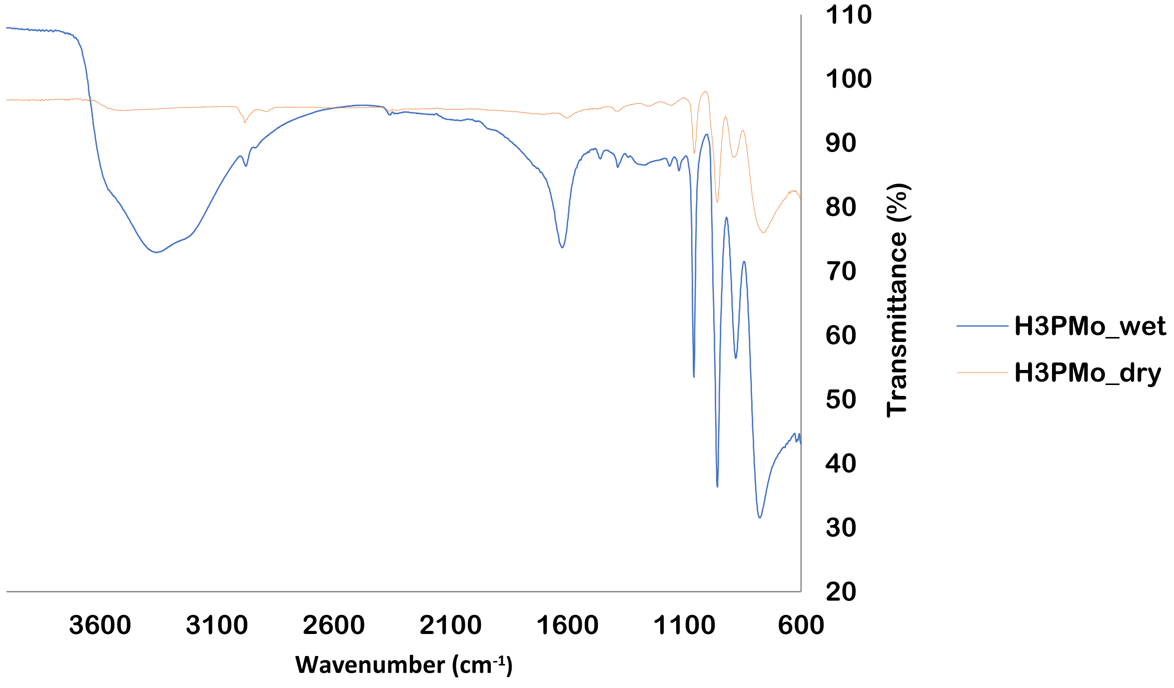

Figure 3-6 FTIR spectra of $H_3PMo_{12}O_{40}$ air-stored (wet) and vacuum-dried (dry) samples

3.2.4.2 $H_3PMo_{12}O_{40}$, $Li_3PMo_{12}O_{40}$, $Na_3PMo_{12}O_{40}$, $Mg_{1.5}PMo_{12}O_{40}$, $Ca_{1.5}PMo_{12}O_{40}$

The counter-cation exchanged POMs showed very similar results, indicating that the structure and bonding within the Keggin ions are not significantly affected by the counter-cations.

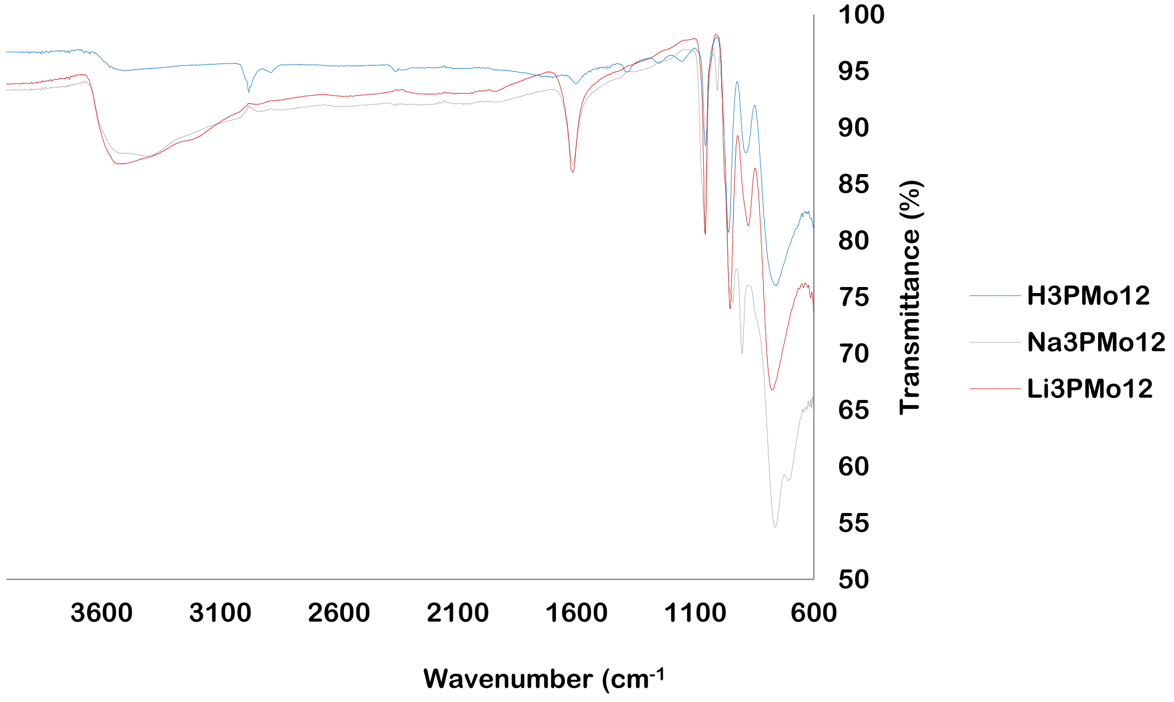

Figure 3-7 FTIR of vacuum-dried $H_3PMo_{12}O_{40}$, $Li_3PMo_{12}O_{40}$ and $Na_3PMo_{12}O_{40}$ samples

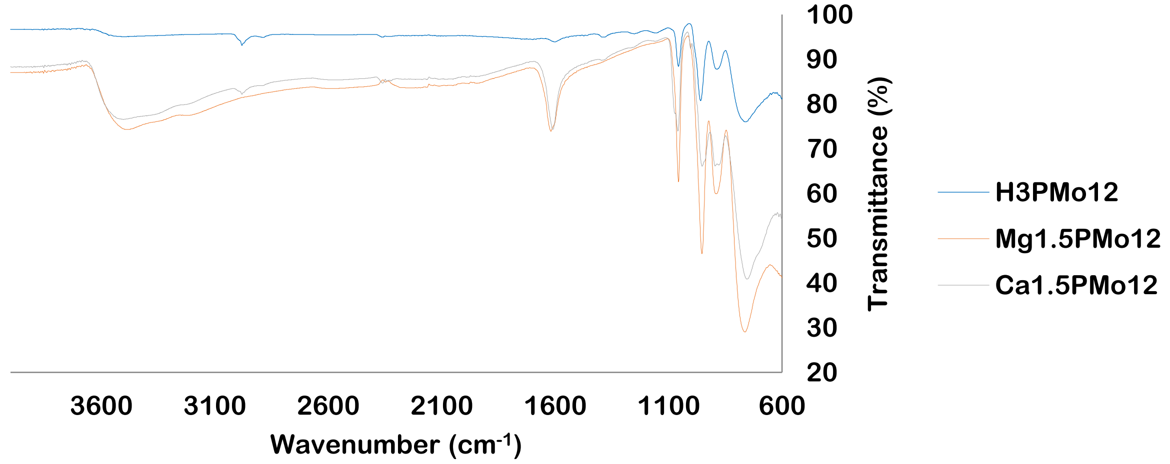

Figure 3-8 FTIR of vacuum-dried $H_3PMo_{12}O_{40}$, $Mg_{1.5}PMo_{12}O_{40}$ and $Ca_{1.5}PMo_{12}O_{40}$ samples

3.2.4.3 FTIR following reduction of $Li_3PMo_{12}O_{40}$ in acetonitrile to different open circuit potentials (OCPs)

FTIR spectra for POM solutions that had undergone bulk electrolysis to different extents were obtained for comparison with the results from charge/discharge experiments in the next chapter to demonstrate structural integrity. Therefore, FTIR results obtained after reduction to different with different open circuit potentials are shown below to illustrate the changes for different POM oxidation states.

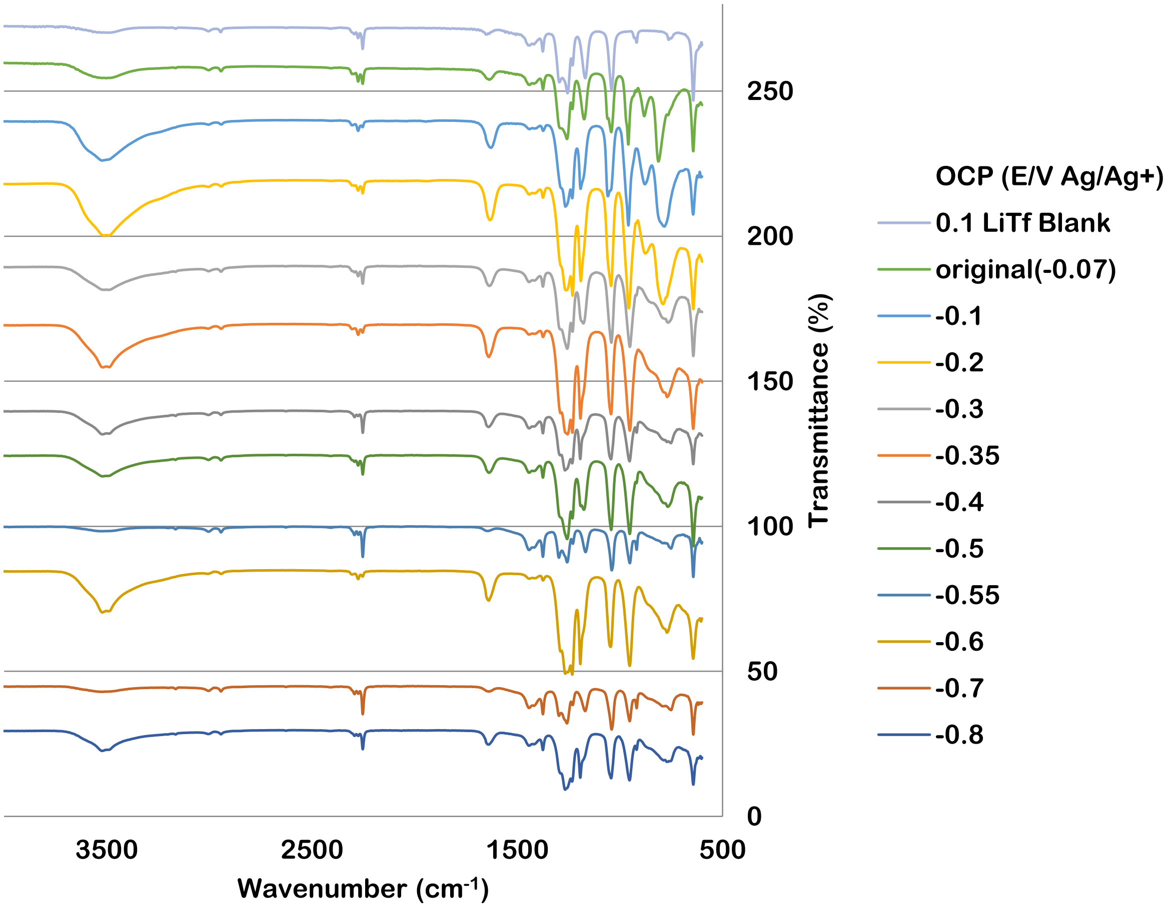

Figure 3-9 FTIR spectra of 0.01M $Li_3PMo_{12}O_{40}$ with 0.1M LiTf in acetonitrile at different extents of reduction

As the 0.01M $Li_3PMo_{12}O_{40}$ with 0.1 M LiTf was reduced by bulk electrolysis, FTIR spectra of the liquid were obtained at increments of the open circuit potential. At an OCP of -0.5V, corresponding to $PMo_{12}O_{40}^{4-}$, the vibration frequency of the Mo−O_c−Mo mode shifted from 837 cm^{-1} to 756 cm^{-1} and Mo−O_b−Mo mode shifted from 877 cm^{-1} to 821 cm^{-1}. These shifts illustrate the effect of electron addition to the $PMo_{12}O_{40}^{4-}$ molecule. Sun et al. reported similar behavior with $TBA_3PMo_{12}O_{40}$ [18]. The changes of the vibrational frequencies indicated that the added electrons were localized, as previously indicated by Electron Spin Resonance Spectroscopy [18][19]. However, the overall structure was maintained, and subsequent reversibility tests showed the reversibility of $Li_3PMo_{12}O_{40}$ reduction.

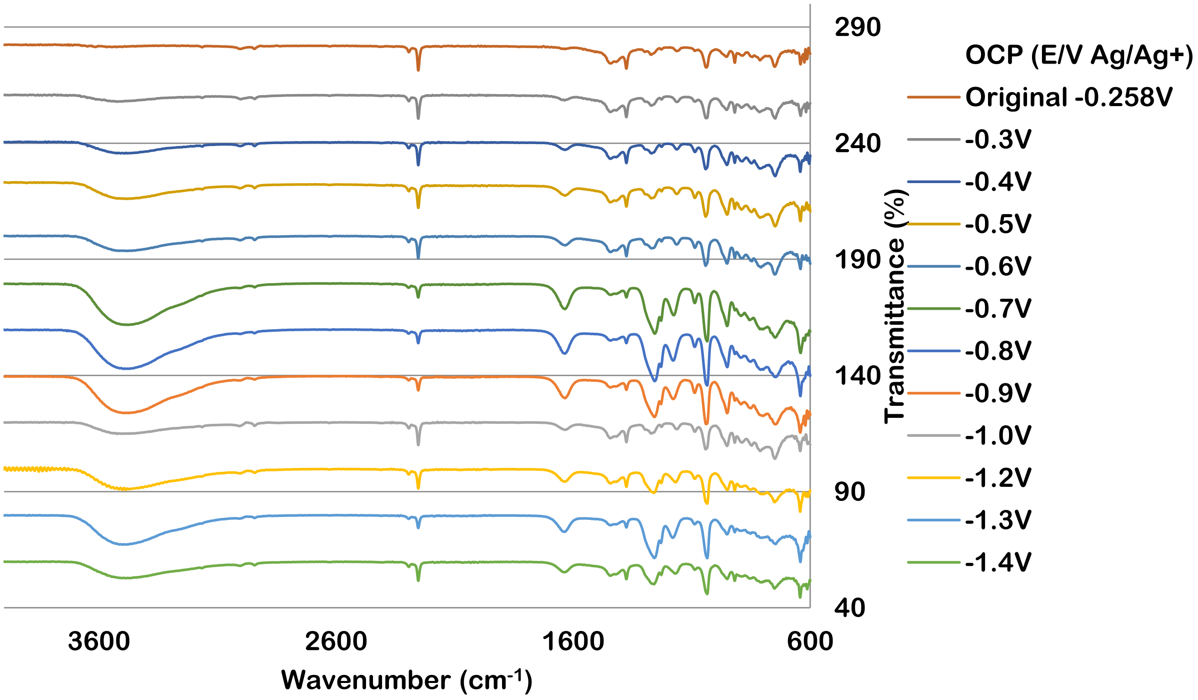

Figure 3-10 FTIR spectra of 0.01M $Li_3PW_{12}O_{40}$ with 0.1M LiTf in acetonitrile with different extents of reduction

Typical $PW_{12}O_{40}^{3-}$ bands appear at 1090-1060 cm^{-1} (P-O), 1010-930 cm^{-1} (W_dO), 900-870 and 850-700 cm^{-1} (W-O-W) [17]. The FTIR results within those regions did not change while the $PW_{12}O_{40}^{3-}$ was reduced. The broad peaks between 3200~3600 cm^{-1} (OH stretching modes), the peak near 1620 cm^{-1} (OH bending modes) increased after bulk electrolysis to an OCP of -0.5 E/V Ag/Ag^+ indicated the presence of OH groups, possibly from the RVC electrodes. The first redox peak of $Li_3PW_{12}O_{40}$ appeared at -0.6 E/V Ag/Ag^+ which corresponds to the increasing intensity of the -OH modes at with increasing reduction, as the RVC electrode began to react. A similar effect could be seen with in $PMo_{12}O_{40}^{3-}$, where the first redox couple started from -0.17 E/V Ag/Ag^+.

3.2.5 Bulk Electrolysis

The bulk electrolysis results were to determine the number of electrons transferred in each redox couple for further battery application purposes. The number of electron transfers in the first and second redox couples for $Li_3PMo_{12}O_{40}$ was reported in chapter 2. The first and second couples for this compound were both one electron transfers.

3.2.5.1 $Cu_{1.5}PMo_{12}O_{40}$

$Cu_{1.5}PMo_{12}O_{40}$ exhibited three redox couples in CV. The number of electrons transferred in each couple (from positive to negative voltage) were two, one, and one. The second and third couple represent the typical $PMo_{12}O_{40}^{3-}$ redox couples (-0.23, -0.59 E/V, Ag/Ag^+). The first couple from the positive side is the Cu^{2+}/Cu couple (0.60 E/V Ag/Ag^+). The 0.32 V peak separation of the first Cu^{2+}/Cu couple corresponded to complete reduction of the copper cations.

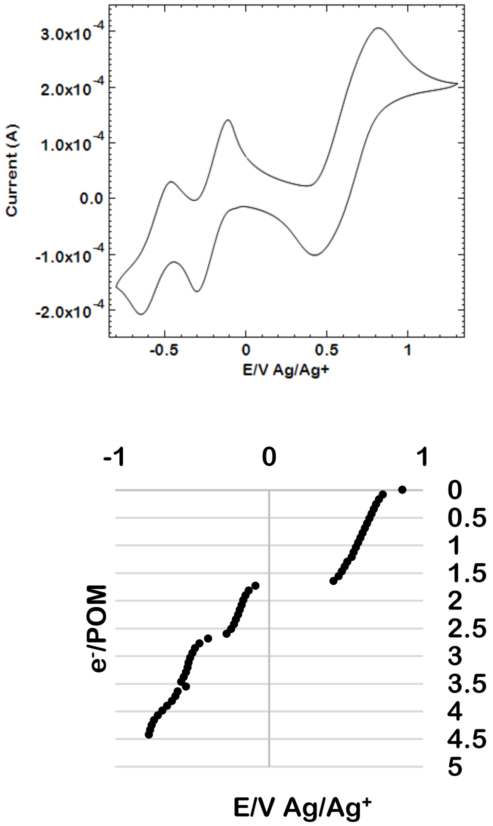

Figure 3-11 Top: CV of 0.01M $Cu_{1.5}PMo_{12}O_{40}$ with 0.1M LiTf in acetonitrile; Bottom: bulk electrolysis of the same solution

3.2.5.2 $Li_6P_2W_{18}O_{62}$

After examination by bulk electrolysis, the redox couples at -0.78 E/V Ag/Ag^+ and -1.21 E/V Ag/Ag^+ were both determined to be one electron transfer couples. The first oxidation peak decreased after the first 5 cycles of CV. The peak voltage separations of 0.30 and 0.37V for the -0.78E/V Ag/Ag^+ and -1.21 E/V Ag/Ag^+ peaks indicated that both the redox couples are controlled by both charge transfer and mass transport phenomena.

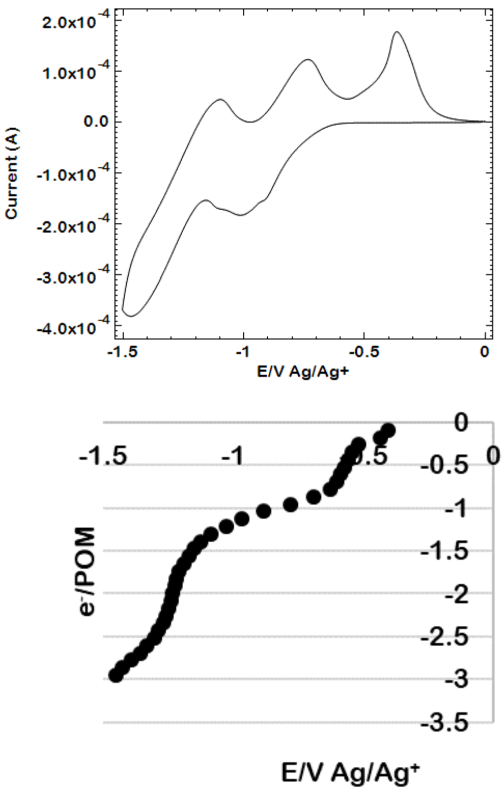

Figure 3-12 Top: CV of 0.01M $Li_6P_2W_{18}O_{62}$ with 0.1M LiTf in acetonitrile; Bottom: bulk electrolysis of the same solution

3.3 Conclusions

In this chapter, several basic characteristics of the polyoxometalates utilized in this dissertation have been examined. TGA was used to determine the water content of vacuum-dried POMs used in later experiments. XRD was used to confirm the crystal structure. FTIR was used to monitor structure and bonding in different POM materials (e.g., $Li_3PMo_{12}O_{40}$ and $Li_3PW_{12}O_{40}$) and different oxidation states. Bulk electrolysis provided the number of electron transfers taking place in each redox couple, providing guidance for battery design purposes.

3.4 References

[1] Song, F., Ding, Y., Ma, B., Wang, C., Wang, Q., Du, X., Fu, S, & Song, J. (2013). K 7 [Co III Co II (H 2 O) W 11 O 39]: a molecular mixed-valence Keggin polyoxometalate catalyst of high stability and efficiency for visible light-driven water oxidation. *Energy & Environmental Science*, *6*(4), 1170-1184.

[2] Ishii, Y., Takenaka, Y., & Konishi, K. (2004). Porous Organic–Inorganic Assemblies Constructed from Keggin Polyoxometalate Anions and Calix [4] arene–Na+ Complexes: Structures and Guest-Sorption Profiles. *Angewandte Chemie International Edition*, *43*(20), 2702-2705.

[3] Suryanarayana, C., & Norton, M. G. (2013). *X-ray diffraction: a practical approach*. Springer Science & Business Media.

[4] Stuart, B. Infrared Spectroscopy (2005) *Kirk-Othmer Encyclopedia of Chemical Technology*. Hoboken, NJ, USA: John Wiley & Sons, Inc.

[5] Kucharyson, J. (2017). Structure-Function Relationships of Metal Coordination Complexes for Non-Aqueous Redox Flow Batteries. Doctoral dissertation. University of Michigan – Ann Arbor.

[6] Molina, P. I., Sures, D. J., Miró, P., Zakharov, L. N., & Nyman, M. (2015). Bridging the opposite chemistries of tantalum and tungsten polyoxometalates. *Dalton Transactions*, *44*(36), 15813-15822.

[7] Damyanova, S., & Fierro, J. L. G. (1998). Structural features and thermal stability of titania-supported 12-molybdophosphoric heteropoly compounds. *Chemistry of materials*, *10*(3), 871-879.

[8] Rocchiccioli-Deltcheff, C., & Fournier, M. (1991). Catalysis by polyoxometalates. Part 3.—Influence of vanadium (V) on the thermal stability of 12-metallophosphoric acids from in situ infrared studies. *Journal of the Chemical Society, Faraday Transactions*, *87*(24), 3913-3920.

[9] Kozhevnikov, I. V. (1998). Catalysis by heteropoly acids and multicomponent polyoxometalates in liquid-phase reactions. *Chemical Reviews*, *98*(1), 171-198.

[10] Sigma-Aldrich. Phosphomolybdic acid hydrate for microscopy. Retrieved from http://www.sigmaaldrich.com/catalog/product/sial/79560?lang=en&region=US.

[11] Misono, M., Mizuno, N., Katamura, K., Kasai, A., Konishi, Y., Sakata, K., ... & Yoneda, Y. (1982). Catalysis by Heteropoly Compounds. III. The Structure and Properties of 12-Heteropolyacids of Molybdenum and Tungsten (H3PMo12− x W x O40) and Their Salts Pertinent to Heterogeneous Catalysis. *Bulletin of the Chemical Society of Japan*, *55*(2), 400-406.

[12] Zhang, Y., & Yang, S. (2008). Synthesis, characterization and catalytic application of H 3 PW 12 O 40/MCM-48 in the esterification of methacrylic acid with n-butyl

alcohol. *Journal of Wuhan University of Technology--Materials Science Edition*, *23*(3), 346-349.

[13] Popa, A., Sasca, V., Kiss, E. E., Marinkovic-Neducin, R., Bokorov, M. T., & Holclajtner-Antunović, I. (2010). Studies in structural characterization of silica–heteropolyacids composites prepared by sol–gel method. *Materials Chemistry and Physics*, *119*(3), 465-470.

[14] La, K. W., Kim, H., Jung, J. C., Lee, J., Park, D. R., Lee, S. H., & Song, I. K. (2008). Preparation of H5PMo10V2O40 catalyst immobilized on spherical carbon and its application to the vapor-phase 2-propanol conversion reaction. *Korean Journal of Chemical Engineering*, *25*(4), 710-713.

[15] Benadji, S., Eloy, P., Leonard, A., Su, B. L., Rabia, C., & Gaigneaux, E. M. (2012). Characterization of H 3+ xPMo 12− xVxO 40 heteropolyacids supported on HMS mesoporous molecular sieve and their catalytic performance in propene oxidation. *Microporous and Mesoporous Materials*, *154*, 153-163.

[16] Tessonnier, J. P., Goubert-Renaudin, S., Alia, S., Yan, Y., & Barteau, M. A. (2012). Structure, stability, and electronic interactions of polyoxometalates on functionalized graphene sheets. *Langmuir*, *29*(1), 393-402.

[17] Paze, C., Bordiga, S., & Zecchina, A. (2000). H2O interaction with solid H3PW12O40: An IR study. *Langmuir*, *16*(21), 8139-8144.

[18] Sun, H. R., Zhang, S. Y., Xu, J. Q., Yang, G. Y., & Shi, T. S. (1998). Electrochemical and in-situ UV-visible-near-IR and FTIR spectroelectrochemical characterisation of the mixed-valence heteropolyanion PMo 12 O 40 n−(n= 4, 5, 6, 7) in aprotic media. *Journal of Electroanalytical Chemistry*, *455*(1), 57-68.

[19] Sanchez, C., Livage, J., Launay, J. P., Fournier, M., & Jeannin, Y. (1982). Electron delocalization in mixed-valence molybdenum polyanions. *Journal of the American Chemical Society*, *104*(11), 3194-3202.

Chapter 4

Evaluation Of Polyoxometalate Charge And Discharge Performance In Static Cell Studies

4.1 Background and Approach

Polyoxymetalates (POMs) have been studied extensively for use in energy applications such as fuel cells, supercapacitors, and as electrode components [1],[2]. One appealing feature of these materials is their stability in multi-electron redox reactions. Sonoyama et al. investigated a potassium cation POM salt, $K_3PMo_{12}O_{40}$, as a lithium battery cathode component. Lithium ions were presumed to be intercalated into bulk $K_3PMo_{12}O_{40}$ layers during discharge [3]. Wang et al. previously reported that $H_3PMo_{12}O_{40}$ incorporated into electrodes can undergo 24 electron transfers during charge/discharge cycles [4]. These results suggest POMs have several useful characteristics for use in energy storage applications.

Non-aqueous redox flow batteries (RFBs) offer both advantages and disadvantages relative to aqueous systems. Water has a relatively narrow window for electrochemical processes, 1.5 V for practical purposes, while acetonitrile has a potential window of 5 V, potentially increasing the energy density[5]. Reactions that occur outside the voltage window within which water is stable can therefore be made accessible in organic solvents. However, higher solvent cost, higher viscosities, lower conductivities, and lower current densities compared to aqueous systems provide challenges for the application of non-aqueous RFBs. In order to improve the low conductivities in non-aqueous systems, support electrolyte is commonly used to increase the cell conductivity. Therefore, the cost of support electrolyte is an important issue for development of economical RFBs. The comparatively lower current densities in non-aqueous RFBs are in part due to the lower solubilities of most active materials in non-aqueous media. In the present work, lithium was chosen as the counter ion for both the active species and the support electrolyte in order to prevent H_2 generation during charge and discharge. Further, the lithium salt of phosphomolybdic acid has the highest solubility in acetonitrile (0.8M) among the all the group IA and IIA salts of this compound.

Membrane performance has also been shown to differ between aqueous and non-aqueous media [6]. High ionic conductivity, high ion selectivity, good chemical stability, good mechanical stability and long lifetime are all key properties for membranes [7]. Depending on the specific system, one may choose ion-exchange membranes or nano-porous membranes. Examples evaluated in this work included Li^+-exchanged Nafion®117 and a nanoporous aramid nanofiber based membrane (ANF) previously reported by Yang et al. [8]. The ANF membranes were constructed by layer-by-layer assembly from a stable dispersion of high-aspect-ratio aramid nanofibers (ANFs) with diameters between 3 and 30 nm [22]. In this chapter, key properties relevant to membrane performance and current density are examined in acetonitrile employing POMs as the active material

4.2 Material and Methods

All standard potentials and diffusivities were measured by cyclic voltammetry (CV) with an Autolab PGSTAT302N Potentiostat and Nova software. The three electrode cyclic voltammetry experiments were performed with a 3mm glassy carbon working electrode (BASi), Ag/Ag^+ (BASi) as the reference electrode and a platinum wire (BASi) as the counter electrode. The working electrodes were all polished with 15 µm silicon carbide paper, washed in an ultrasonic bath to ensure a clean surface, and dried in air before the experiment. $Li_3PMo_{12}O_{40}$ was obtained from Nippon Inorganic Colour & Chemical Co., Ltd. The support LiTf (Lithium trifluoromethanesulfonate, (99.995%) was obtained from Sigma-Aldrich and solvent ACN (acetonitrile, 99.9%) from Fisher Scientific. Working solutions were sparged with nitrogen for 10 minutes before CV, and the experiments were run in the air at room temperature.

Electrochemical impedance spectroscopy (EIS) was performed in a two-electrode configuration with an Autolab PGSTAT302N Potentiostat in a static H-cell (Adams & Chittenden Scientific Glass.) Each side of the half H-cell was filled with 5 mL 0.1M LiTf in ACN. The H-cell design has been previously presented in [9]. The two electrodes (graphite plates with an area of $1cm^2$, GraphiteStore) were calcined at 550^oC in nitrogen to remove moisture prior to use.

Attenuated total reflectance (ATR) FTIR (FT/IR-4100 Jasco) spectra of electrolyte solutions were measured at wavelengths between 600 cm^{-1} to 4000 cm^{-1}. These were used to detect changes in polyoxometalate characteristics before and after electrochemical experiments.

Crossover tests were performed in the H-cell and the membranes were placed in the electrolyte solution on one side and pure acetonitrile on the other. Both were stirred with micro stir bars, and the initially pure acetonitrile side was sampled over time using a NanoPhotometer®P300.

Charge/Discharge (CD) experiments were performed in the static H-cell with a Maccor Series 4000 battery tester. The working electrodes were the same graphite electrodes used in EIS experiments. Each side of the H-cell was filled with 5 mL of the test solution, and electrodes were soaked in the solution. The electrodes were calcined prior to CD experiments. CD experiments were monitored with Ag/Ag^+ reference electrodes. Both sides of the H-cell contained a micro stir bar to minimize mass transport limitations while the cell was being charged or discharged. The separators used were Nafion® 117 (Fuel Cell Store), Celgard®2325 (Celgard), and an aramid nanofiber based membrane (ANF) provided by the Kotov group at the University of Michigan [10].

Membranes were soaked in acetonitrile containing the supporting electrolyte (LiTf) for more than 24 hours prior to each test. The Nafion 117 membrane was exchanged with lithium prior to use, following the procedure adopted from [11].

4.3 Results and Discussion

4.3.1 Membrane Selections: EIS and permeability test

Membrane selection was the first step in the experimental design, as membrane properties can have a large influence on the charge/discharge results. A good membrane or separator will selectively allow charge carriers to pass freely while preventing transport of other ions that would result in mixing and loss of performance. Such a selection generally involves a tradeoff, as materials that allow transport of charge carriers will often result in some rate of electrolyte transport resulting in losses of stored energy, and membranes that minimize electrolyte transport can often have high resistance to charge carrier transport leading to I^2R energy losses.

For the analysis of POMs in non-aqueous RFBs, ion selection and pore size selection membranes were selected as potential candidates due to their routine use in RFB and fuel cell applications. Celgard® 2325, a commercial pore size selection membrane, has a 0.028 µm average diameter pore size, allowing molecules smaller than this diameter to pass. In a visual crossover test, within one hour the two sides of an H-cell containing reduced and oxidized phosphomolybdate ions had started to mix, as shown in Figure 4-1. Thus, this separator was not considered further.

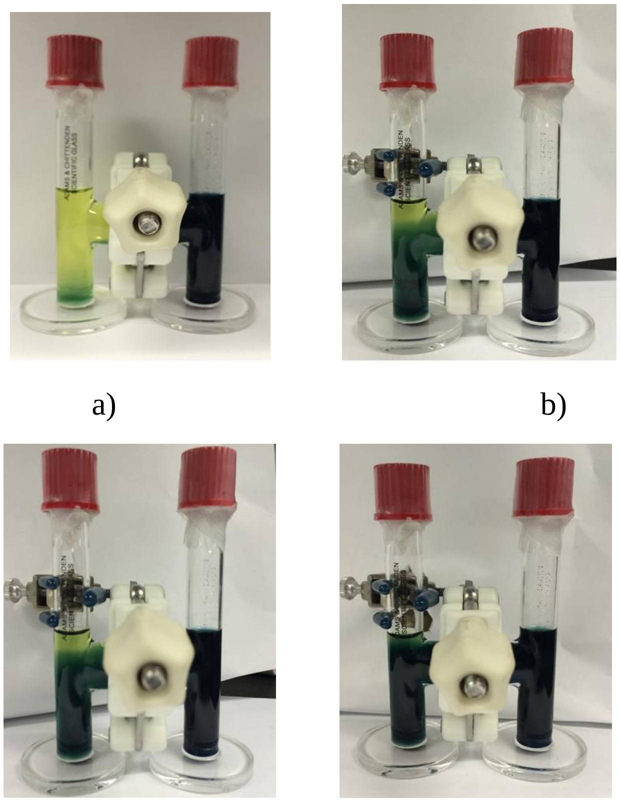

a) b)

c) d)

Figure 4-1. Visual cross over test for Celgard® 2325. $PMo_{12}O_{40}^{3-}$ is the light yellow solution, and $PMo_{12}O_{40}^{5-}$ is the dark green solution. Time: a) 0hr, b) 0.5 hr, c)1hr, d) 6hr.

Nafion®117 is a well-known proton-exchange membrane which has been widely used in fuel cell applications. Since lithium ions were the charge carriers in this work, the Nafion®117 membrane was pretreated to exchange lithium ions for protons as described above. Ideally, only the Li cations can pass through the membrane, with the POM anions unable to cross. A test to measure the extent of crossover from a $Li_3PMo_{12}O_{40}$ solution into pure acetonitrile is depicted in Figure 4-2a. After 144 hours (6 days), less than 0.5% of the active species had diffused across the membrane as determined from the increase of the UV-vis signal for the POM in the initially pure acetonitrile, showing good resistance to POM transport by the Nafion®117 membrane. The small excursion of the point at 96 hours reflected the uncertainty of measuring very low POM concentrations with UV-Vis. Overall, these results clearly demonstrate the low permeability of the Nafion®117 membrane to POMs.

We also investigated the use of a new aramid nanofiber (ANF) based pore-size selection membrane [10]. The crossover test in Figure 4-2b showed that even after 6 days, less than 4% of the active species had diffused across the membrane. Compared to the pore size selection membrane Celgard® 2325, ANF shows good separation ability. Celgard® 2325 has an average pore diameter of 28 nm (0.028 µm), compared to ANF with a 5 nm pore size [12]. While the diameter of the unsolvated Keggin-type polyoxometalate ion is around 1 nm, smaller than both, the small pores of the ANF membrane appeared to provide adequate separation. Based on their proven ability to prevent heteropolyanion crossover, Nafion®117 and ANF membranes were selected as viable candidates for the POM non-aqueous RFB studies.

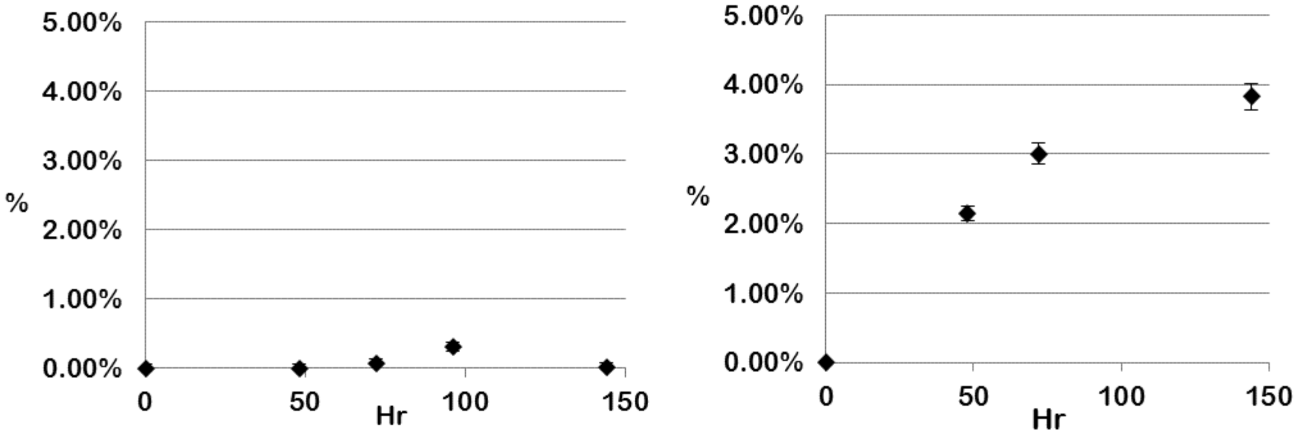

a)

b)

Figure 4-2. Percent crossover of $PMo_{12}O_{40}^{3-}$ from a 0.01M solution into pure acetonitrile for a) Nafion®117, b) ANF membranes.

Membrane	Resistance (Ω)
Celgard® 2325	64
ANF	82
Nafion®117	853

Table 4-1. EIS resistance measurements for different membranes in acetonitrile with 0.1M LiTf in the H-cell.

As the resistance of the membrane could also influence the charge/discharge energy efficiency, electrochemical impedance spectroscopy (EIS) was used to determine the resistances of the membranes. The resistances of the membranes in the H-cell with 0.1M Lithium trifluoromethanesulfonate (LiTf) added to acetonitrile as a support are shown in Table 4-1. These values were obtained by subtracting the background resistance of 916 **Ω** measured in the same cell without the membrane. Both pore selection membranes (Celgard® 2325 and ANF) in acetonitrile have similar resistances, but ANF had much higher transport selectivity as discussed above. Nafion®117 had almost ten times higher resistance than the other two membranes in acetonitrile. A similar poor conductivity for Li-exchanged Nafion®117 in acetonitrile was reported previously: 5.36×10^{-6} S/cm in acetonitrile vs. 1.61×10^{-2} S/cm in water [6]. Lithiated Nafion®117 membranes have previously been examined in different non-aqueous solvents (propylene carbonate, propylene carbonate: ethylene carbonate, and dimethyl sulfoxide) [13]. The main reason for the variations in membrane conductivity among these could be the solvent volume fraction and the degree of charge carrier dissociation from the tethered ion. Charge exclusion also contributes, but the authors argue that this effect is small compared to size exclusion [13].

The resistance versus time of ANF in 0.1M LiTf/ACN was tested in order to determine the appropriate soaking time and the stability of the membrane in the electrolyte solution. A dried ANF membrane (in contrast, membranes in Table 4-1 were soaked for 2 weeks) was placed in the H-cell as a separator and measured with EIS. The EIS resistance dropped quickly between

1 hour and 8 hours of soaking in electrolyte from 218 Ω to 113 Ω. After 48 hours, the resistance remained stable at approximately 100 Ω, and changed relatively little for longer times.

4.3.2 Symmetric Charge Discharge Experiments

4.3.2.1 $Li_3PMo_{12}O_{40}$

The performance of POMs in acetonitrile was examined in charge/discharge experiments using the H-cell described above. The symmetric configuration contained 0.01M $Li_3PMo_{12}O_{40}$ with 0.1M LiTf as the supporting electrolyte. Figure 4-4 shows the characteristic CV for these concentrations. The first and second redox couples were observed at -0.21 and -0.57 V, respectively, with potentials reported relative to an internal Ag/Ag^+ reference. The respective peak separations ($\Delta E_p = E_{pc} - E_{pa}$) for the two redox events were 196 mV and 190 mV, and the peak height ratios (ip_a/ip_c) were 0.80 and 0.84. The peak separation and peak height ratios observed are indicative of quasi-reversible redox behavior, with reversible behavior defined as a peak separation of 59 mV per electron and a peak height ratio of 1. Previous literature has reported the $PMo_{12}O_{40}^{3-}$ ion diffusion coefficient in acetonitrile to be $9.7 \times 10^{-6}\ cm^2s^{-1}$ [14], about half that of ferrocene (Fc) at $2.24 \times 10^{-5}\ cm^2s^{-1}$ [15]. Since the Keggin structure does not change with varying oxidation state, the diffusion coefficients are expected to be similar for the different oxidation states accessed in our charge/discharge experiments, although direct measurements are lacking.

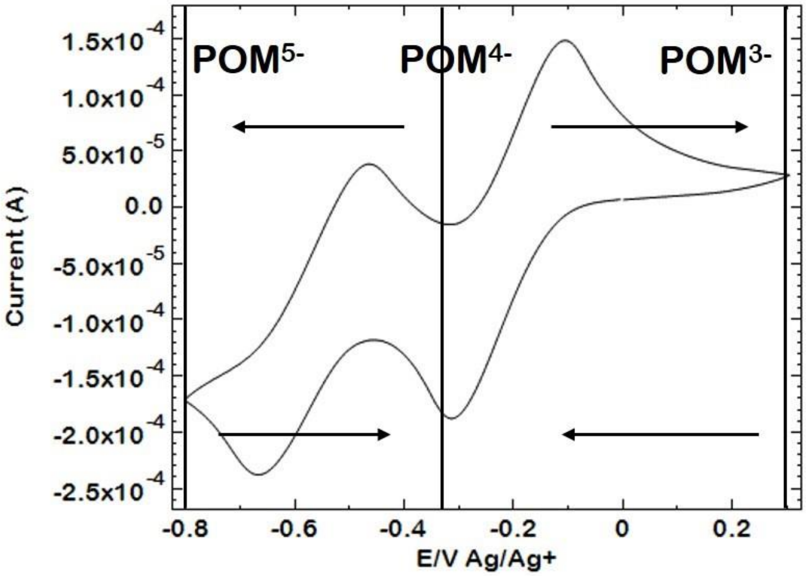

Figure 4-3 Cyclic voltammogram for 0.01M $Li_3PMo_{12}O_{40}$ with 0.1M LiTf in acetonitrile, showing the 1-electron transfers accessed in the charge/discharge experiments.

Initial experiments were carried out using the Li-exchanged Nafion®117 membrane. With bulk-electrolysis-pretreated $Li_3PMo_{12}O_{40}$ on both sides, the solution open circuit potential was reduced from 0.1 to -0.4 E/V Ag/Ag+ in order to make a balanced electron charge/discharge experiment. By charging the cell from an initial potential of -0.4 to 0.3 E/V Ag/Ag+ at the catholyte side and -0.8 E/V Ag/Ag+ at the anolyte as shown in the cyclic voltammetry plot in Figure 4-3, a 1-electron redox couple was accessed on each side. The charge/discharge reaction was $PMo_{12}O_{40}^{4-} \leftrightarrows PMo_{12}O_{40}^{3-}$ on the catholyte side and $PMo_{12}O_{40}^{4-} \leftrightarrows PMo_{12}O_{40}^{5-}$ on the anolyte side.

The charge/discharge cut-off was based on potentials measured with respect to reference electrodes on each side of the cell while monitoring the coulombic charge to ensure that the compound was not destroyed due to overcharging. Results of these charge/discharge experiments are shown in Figure 4-4. Figure 4-4a shows charge/discharge cycles 3 through 5. While stable charge and discharge were observed, the charge rate was limited to 0.1mA/cm^2 on a 1 cm^2 active surface area electrode. Therefore, the cycle time was between 20 and 26 hours to reach 100% state of charge. Figure 4-4b shows the stability of the $Li_3PMo_{12}O_{40}$ CD and its behavior with the Nafion®117 membrane. Even after 35 cycles with 50% state of charge (over 500 hours), the coulombic efficiency remained at 96% and the energy efficiency remained stable at 38%. When the $Li_3PMo_{12}O_{40}$ solution was charged or discharged, no precipitates were observed on either the catholyte side or anolyte side, indicating that the solubilities of oxidized and reduced states of the POM were not limiting at the concentration examined. This is not surprising since the tested concentration of 0.01 M is well below the solubility of $Li_3PMo_{12}O_{40}$, 0.8M. However, solubility variations of the Keggin species in different oxidation states could, in principle, limit the charge and discharge at higher concentrations.

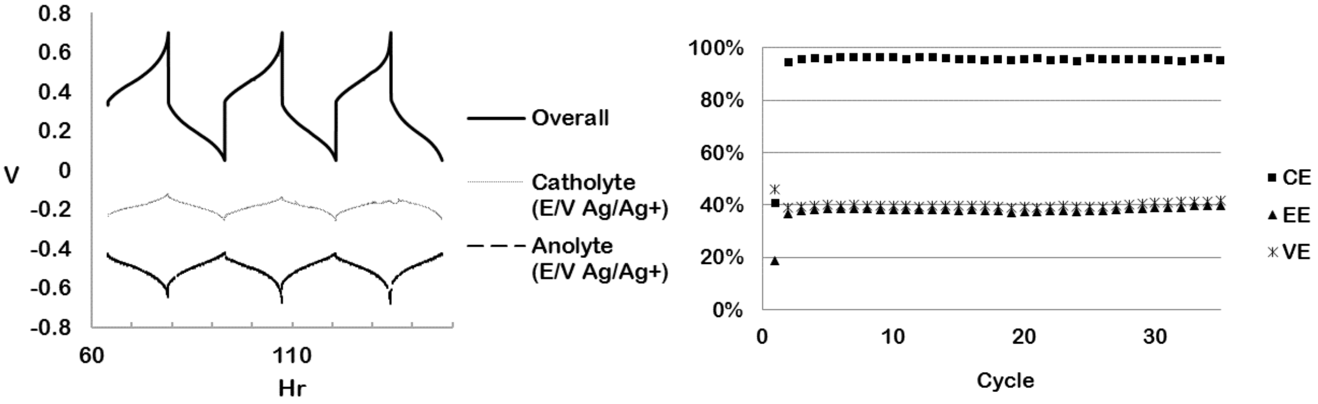

a)

b)

Figure 4-4. $Li_3PMo_{12}O_{40}$ charge/discharge with Nafion®117, a) 3rd-5th cycle, b) long term charge/discharge, coulombic efficiency (CE), energy efficiency (EE) and voltage efficiency (VE) at 50% state of charge.

In this work, we focus mainly on the coulombic efficiency, as this provides an indication of the reversibility of the electrochemical reaction and the stability of the compound. The coulombic efficiency is directly related to the lifetime of the battery; the higher the coulombic efficiency, the greater the number of cycles that the battery could potentially sustain. The energy efficiency is strongly affected by the cell design, the resistance and the energy lost. In order to shorten the charge/discharge cycle time, experiments were carried out using rates of $0.2 mA/cm^2$ and $0.5 mA/cm^2$. These experiments resulted in no stored charge.

Experiments were then carried out using the ANF membrane with 0.01M $Li_3PMo_{12}O_{40}$ in acetonitrile with 0.1M LiTf as support electrolyte. Results are shown in Figure 4-5 and Table 4-2. The coulombic efficiency (CE) remained high, indicating the high stability of $Li_3PMo_{12}O_{40}$ in charge/discharge experiments. The slightly lower CE relative to charge/discharge (CD) with Nafion®117 may reflect the different extents of crossover for these membranes noted above. With ANF, we were able to increase the charge rate two to five times higher than with Nafion®117. Nafion®117 has almost ten times higher resistance compared to ANF in the H-cell. Therefore, a lower energy efficiency (EE) of Nafion®117 was observed compared to ANF experiment at the same charge rate ($0.1 mA/cm^2$). However, even with the ANF membrane, as the current was increased, the energy efficiency dropped, as the energy lost due to the resistance increased with applied current. The use of higher current also decreased the state of charge, possibly due to mass transport limitations of species to and from the electrode surface. In the static cell study, the stirring condition was not ideal; the solutions on the two sides of H-cell were circulated by micro stir bars rather than by flow through the cell. The iR loss increased as the current increased in Figure 4-5a~5c. The ANF H cell system resistance from table 4-1 is 82 Ω (ANF) + 916 Ω (H Cell system). The iR drop caused by the resistance in different current density experiments could be calculated as 998 Ω times 0.1, 0.2, or 0.5 mA/cm^2 (the contact surface areas of electrodes were 1cm^2), which gives 99.8, 199.6, or 499 mV, respectively, close to the iR drop shown in Figure 4-5. Thus, while the H-cell results are a useful diagnostic tool for active species and membrane performance, the efficiencies measured do not translate directly to RFB performance.

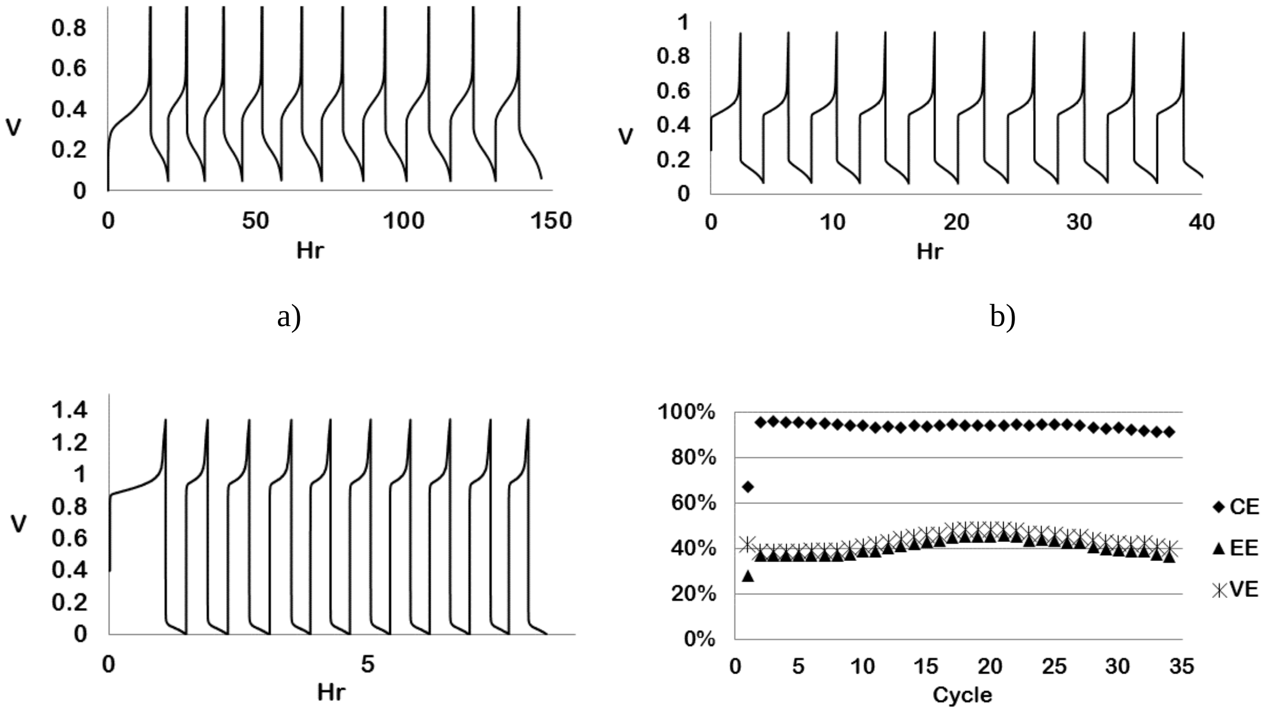

a) b)

c) d)

Figure 4-5 $Li_3PMo_{12}O_{40}$ charge/discharge with ANF, a) 0.1mA/cm^2, b) 0.2mA/cm^2, c) 0.5mA/cm^2, d) long term charge/discharge, coulombic efficiency (CE), energy efficiency (EE) and voltage efficiency (VE) with state of charge 95% at 0.1mA/cm^2.

A long-term experiment of 35 charge/discharge cycles spanning more than 1000 hours with 95% state of charge was performed for ANF with 0.01M $Li_3PMo_{12}O_{40}$ and 0.1M LiTf in acetonitrile, shown in Figure 4-5d. The high coulombic efficiency (~90%) and energy efficiency (~40%) over this long duration showed the compatibility of ANF and $Li_3PMo_{12}O_{40}$.

Membrane	C/D rate (mA/cm^2)	CE(%)	EE(%)	SoC(%)
Nafion®117	0.1	96	38	91
ANF	0.1	88	47	95
ANF	0.2	89	23	44
ANF	0.5	93	8	37

Table 4-2 Coulombic efficiency (CE), energy efficiency (EE) and state of charge obtained at the different currents shown in Figure 4-5

After the experiment, the catholyte and anolyte were also examined by CV (after dilution to 0.5 mM based on the initial POM concentration) and FTIR. Results are shown in Figure 4-6 and Figure 4-7. The CVs showed reproducible and stable results that agreed well with the electrochemical characteristics of $Li_3PMo_{12}O_{40}$ measured before charge/discharge. FTIR spectra in Figure 4-7 obtained before and after CD show the peaks at 1051 cm^{-1} (P−O), 951 cm^{-1} (Mo=O$_t$), 877 cm^{-1} (Mo−O$_b$−Mo), and 741 cm^{-1} (Mo−O$_c$−Mo) [16] characteristic of the POM. Both spectra showed intact POMs after the charge/discharge test.

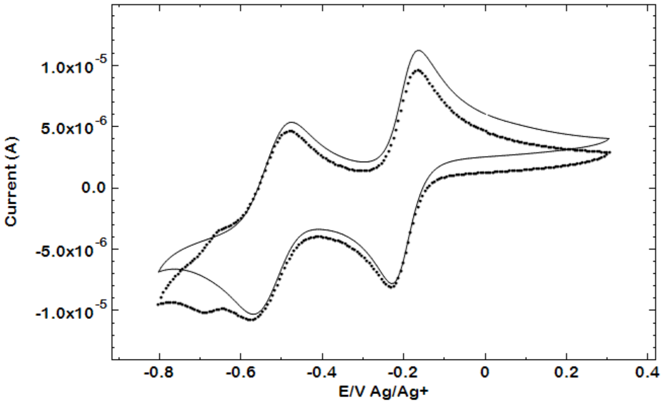

Figure 4-6 Cyclic voltammograms for $Li_3PMo_{12}O_{40}$ after charge/discharge diluted to 0.5mM in acetonitrile; dotted line: catholyte after CD; solid line: anolyte after CD

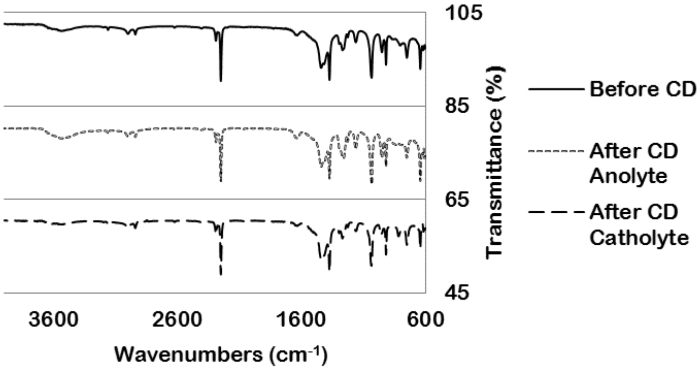

Figure 4-7 FTIR spectra of 0.01M $Li_3PMo_{12}O_{40}$ with 0.1M LiTf before and after charge/discharge, line: before CD; dotted line: catholyte after CD; dashed line: anolyte after CD

These $Li_3PMo_{12}O_{40}$ symmetric charge/discharge tests in the static cell indicate that POMs are a viable class of materials for use as active species in non-aqueous redox flow batteries. The Nafion®117 and ANF membranes both showed reasonable performance with $Li_3PMo_{12}O_{40}$; the latter permitted operation at higher currents. They also serve to put this work in the context of previous studies, primarily those of Pratt and Anderson. Studies by these workers regarding the performance of vanadium-substituted phospho- and silico-tungstate Keggin ions in both aqueous and non-aqueous (propylene carbonate) flow batteries [17],[18] showed similarly high coulombic efficiencies and moderate energy efficiencies in aqueous solution. In a non-aqueous (propylene carbonate) redox flow battery [17], the electrochemical yield, equal to the measured state of charge divided by the theoretical capacity of the system, dropped by half after 10 cycles. That report demonstrated varying performance decays and electrode deposition processes dependent on the specific POM structures and compositions. In the present work, the redox processes accessed in charge/discharge experiments did not depend on the incorporation of specific redox active elements (e. g., vanadium) in the Keggin framework. Extensive studies of the performance and stabilities of phosphomolybdates in non-aqueous RFB applications remain to be carried out.

4.3.2.2 $Cu_{1.5}PMo_{12}O_{40}$

Based on the bulk electrolysis test described in the previous chapter, $Cu_{1.5}PMo_{12}O_{40}$ was bulk electrolyzed from 0.7 to 0.3 E/V Ag/Ag^+ before the charge/discharge test with 0.01 M $Cu_{1.5}PMo_{12}O_{40}$ with 0.1M LiTf. The battery was tested as a 2-electron transfer system with a 1.4 V window starting from 0.3 E/V Ag/Ag^+ and a 50% cutoff for the state of charge with 0.2mA/cm^2 current density.

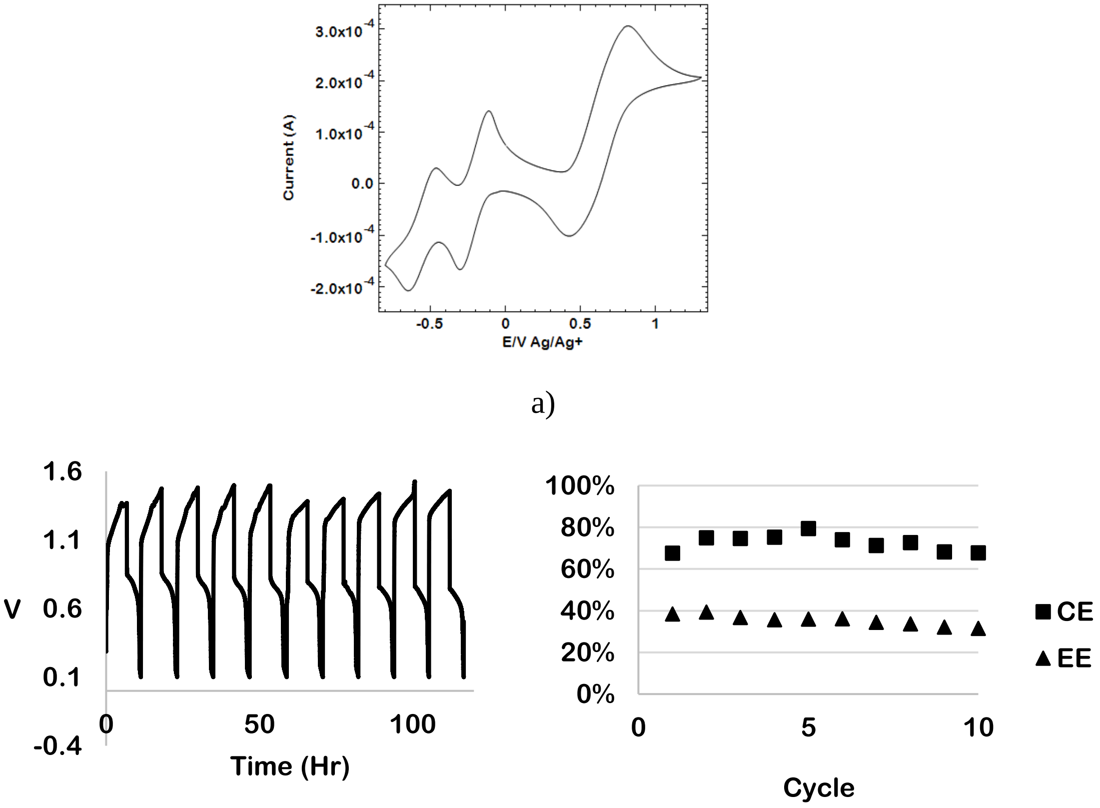

a)

b)

c)

Figure 4-8 Results for 0.01M $Cu_{1.5}PMo_{12}O_{40}$ with 0.1M LiTf in acetonitrile a) CV, b) charge/discharge c) coulombic efficiency, energy efficiency with 50% SoC and 0.2mA/cm^2 current density.

The results from cycling $Cu_{1.5}PMo_{12}O_{40}$ illustrate the benefits of a higher energy density symmetric battery with a wider voltage window and higher number of accessible electron transfers. The battery showed a 60% initial coulombic efficiency and maintained the 60% efficiency after 10 cycles. However, the reductive plating of copper on the cathode, as seen in Figure 4-9 below, remains a concern for the $Cu_{1.5}PMo_{12}O_{40}$ symmetric battery. The copper plating is also the reason for the lower coulombic efficiency compared to the $Li_3PMo_{12}O_{40}$ battery.

Figure 4-9 The cathode after the $Cu_{1.5}PMo_{12}O_{40}$ charge/discharge, the brown copper could be seen clearly on the right side in the picture

4.3.2.3 Effect of $Li_3PMo_{12}O_{40}$ Concentration on static cell performance

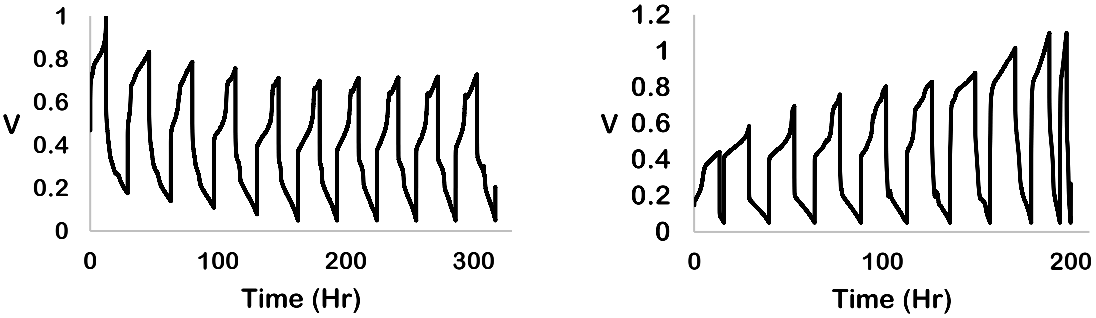

a) b)

Figure 4-10 a) Charge/discharge results for 0.05M $Li_3PMo_{12}O_{40}$ with 0.5M LiTf in acetonitrile at a 0.2 mA charge rate, b) 0.1M $Li_3PMo_{12}O_{40}$ with 1M LiTf at a 0.2 mA charge rate

The 0.01M $Li_3PMo_{12}O_{40}$ with 0.1M LiTf charge/discharge results are shown in Figure 4-5; Figure 4-10 shows results at higher concentrations. Stable cycling was achieved at 0.05M $Li_3PMo_{12}O_{40}$. However, the 0.1M $Li_3PMo_{12}O_{40}$ with 1M LiTf solution did not permit stable charge/discharge; the coulombic efficiency dropped quickly after the 5th cycle. One possible explanation may be the higher viscosity observed and the presumably lower diffusivity at higher concentrations of the POM. In the static H cell, the circulation might not be adequate since the driving force was from the micro stir bars.

4.3.3 Asymmetric Charge Discharge Experiments

The purpose of asymmetric charge/discharge is to increase the energy density of the battery by increasing the maximum voltage window and the number of achievable electron transfers. The following experiments were conducted to assess the performance of $Li_3PMo_{12}O_{40}$/$Li_3PW_{12}O_{40}$ and $Li_3PMo_{12}O_{40}$/$Li_6P_2W_{18}O_{62}$ combinations in asymmetric cells.

4.3.3.1 $Li_3PMo_{12}O_{40}$/$Li_3PW_{12}O_{40}$

The asymmetric charge/discharge experiment was designed with a maximum two electron transfer and a 1.1 voltage window with 0.1mA/cm^2 current density. 0.01M $Li_3PMo_{12}O_{40}$ with 0.1M LiTf was used as the catholyte and 0.01M $Li_3PW_{12}O_{40}$ with 0.1M LiTf was the anolyte. The battery was tested under conditions chosen to produce one electron transfer (50% state of charge as the cutoff). The catholyte side $Li_3PMo_{12}O_{40}$ was bulk electrolyzed at -0.4 E/V Ag/Ag$^+$ before the charge/discharge test, and the anolyte $Li_3PW_{12}O_{40}$ was bulk electrolyzed at -1.1 E/V Ag/Ag$^+$ before beginning the experiment. Catholyte voltages of 0.3 and -0.5 E/V Ag/Ag$^+$ and anolyte voltages of -0.8 and -1.6 E/V Ag/Ag$^+$ were set as the charge/discharge voltage limits for each side.

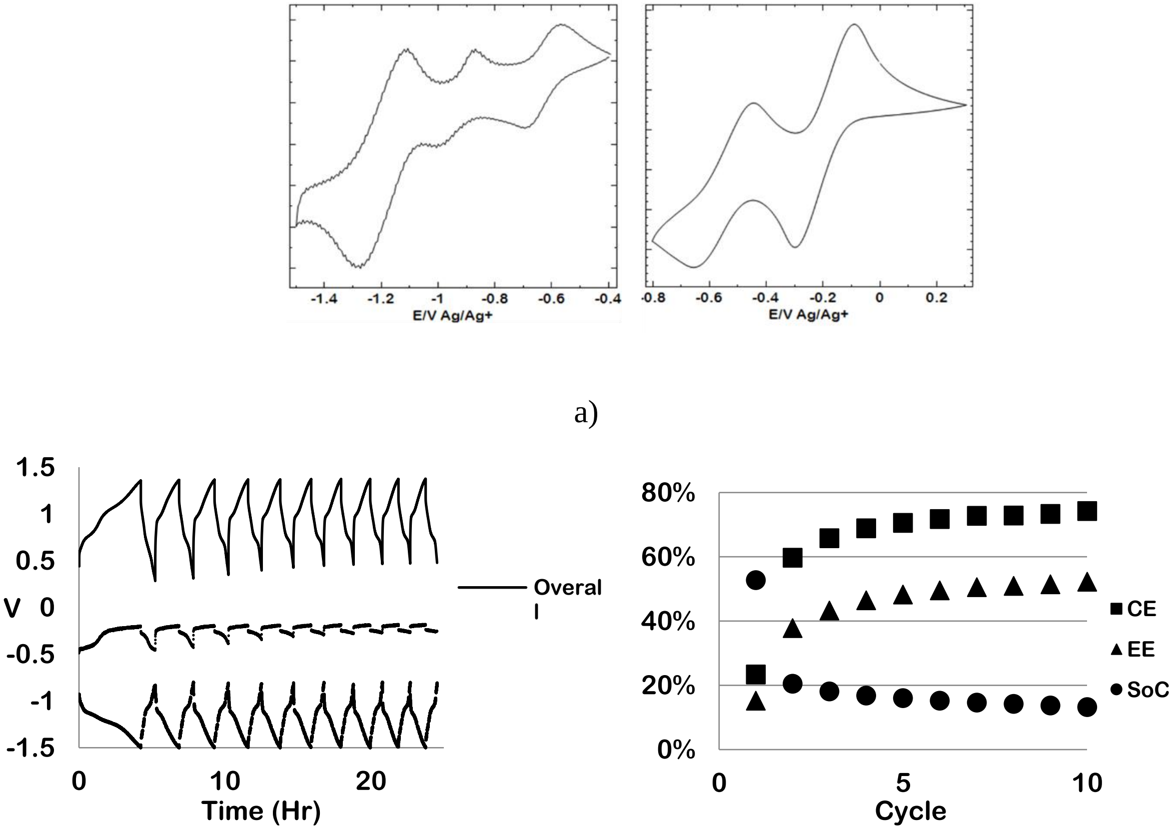

a)

b)

c)

Figure 4-11 $Li_3PMo_{12}O_{40}$/$Li_3PW_{12}O_{40}$ asymmetric charge/discharge results at 0.1mA/cm^2, a) CVs of 0.01M $Li_3PMo_{12}O_{40}$ with 0.1M LiTf (right) and 0.01M $Li_3PW_{12}O_{40}$ with 0.1M LiTf (left), b) charge/discharge, c) coulombic efficiency (CE), energy efficiency (EE) and state of charge (SoC) vs. cycle number.

Despite the observation of nearly reversible redox events in the CV, the results from the charge/discharge experiment show a low state of charge. The voltage curve over time revealed that the anolyte ($Li_3PW_{12}O_{40}$) limited the charge and discharge cycles, because the $Li_3PW_{12}O_{40}$ reached the cutoff voltages at -0.8 and -1.5 E/V Ag/Ag$^+$ during cycling. Theoretically, this battery could have 1.1 V output and 2 electrons transferred. However, the $Li_3PW_{12}O_{40}$ cycling appears to be an obstacle to achieving this performance.

4.3.3.2 $Li_3PMo_{12}O_{40}$/$Li_6P_2W_{18}O_{62}$

The asymmetric charge/discharge experiment was designed with a maximum two electron transfer and a 1.4 voltage window with 0.1mA/cm^2 current density. 0.01M $Li_3PMo_{12}O_{40}$ with 0.1M LiTf was used as the catholyte and 0.01M $Li_6P_2W_{18}O_{62}$ with 0.1M LiTf was the anolyte. The catholyte, $Li_3PMo_{12}O_{40}$, was electrolyzed at -0.4 E/V Ag/Ag$^+$ and the anolyte, $Li_6P_2W_{18}O_{62}$, was electrolyzed at -0.7 E/V Ag/Ag$^+$ before the beginning of the experiment. The charge/discharge strategy involved performing a 1-electron transfer battery test with 0.1mA/cm^2 current density. While performing charge/discharge, the battery was accessing the redox couple between 0.3 ~ -0.4 E/V Ag/Ag$^+$ on the catholyte side, and -0.6 ~ -1.1 E/V Ag/Ag$^+$ on the anolyte side. The battery performance could be theoretically as high as 1.4V and 2 electrons transferred if both redox couples on each side were fully utilized.

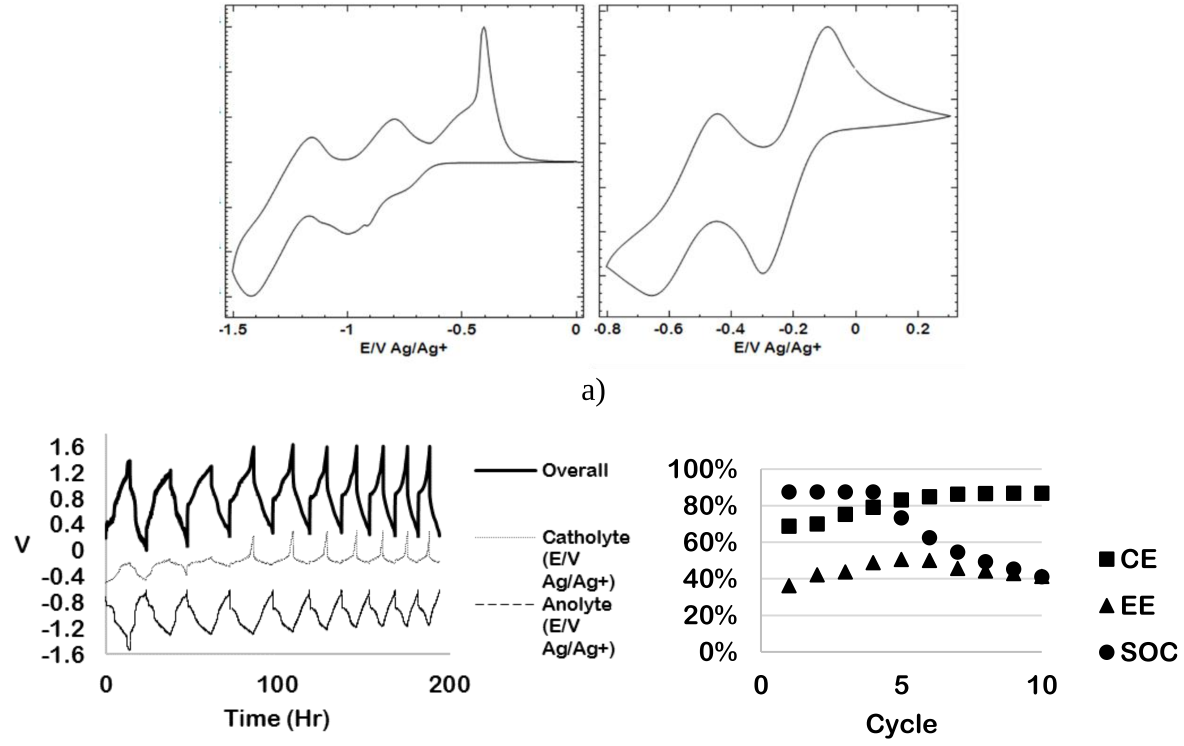

a)

b)

c)

Figure 4-12 $Li_3PMo_{12}O_{40}/Li_6P_2W_{18}O_{62}$ asymmetric charge/discharge with 0.1mA/cm^2, a) CVs of 0.01M $Li_3PMo_{12}O_{40}$ with 0.1M LiTf (right) and 0.01M $Li_6P_2W_{18}O_{62}$ with 0.1M LiTf (left), b) charge/discharge c) coulombic efficiency (CE), energy efficiency (EE) and state of charge (SoC) vs. cycle number.

As seen in Figure 4-12, the decreasing state of charge starting at cycle 5 indicates the stability of this POM combination is limited. By the reference potential measurement (catholyte and anolyte E/V Ag/Ag$^+$), the anolyte limits the early charge/discharge cycles. The battery was not fully discharged during the early cycles because the anolyte reached the discharge cut-off prior to the catholyte's complete discharge. At cycle #5, the catholyte finally reached the charge cut-off, resulting in a decreasing state of charge. However, this POM combination showed the highest state of charge of the asymmetric batteries tested here, which might suggest it as a possible candidate for the redox flow battery application.

4.4 Conclusions

In this chapter, we assessed the use of different membranes with polyoxometalate active species in symmetric batteries. The common commercial membranes Celgard 2325 (NPM) and Nafion®117 (CEM), were compared and tested. The membrane made from Kotov Lab aramid nanofiber (ANF) was also tested for possible use. While the Celgard 2325 showed poor separation ability, the Nafion®117 and ANF both showed high separation ability with less than 5% POM crossover after 144 hours. However, the Nafion®117 resistance in acetonitrile was almost ten times higher than ANF in the H cell experiment. The long term charge/discharge of both Nafion®117 and ANF were tested with $Li_3PMo_{12}O_{40}$, and both batteries retained high coulombic efficiencies (>90%) after more than 30 cycles.

Multiple POM materials were tested as the active species for higher energy density batteries. In these experiments, only the $Li_3PMo_{12}O_{40}$ showed stable columbic efficiency and high state of charge, while other POMs could not be consistently maintained at stable state of charge with high coulombic efficiency (>90%). Higher concentration tests were also performed in the static cell in an attempt to achieve a higher energy density. Unfortunately, at 0.1M POM concentration, the static cell charge/discharge system appeared to be limited by mass transport. The asymmetric charge/discharge experiments were designed to test possible options for achieving higher energy densities. $Li_3PMo_{12}O_{40}/Li_3PW_{12}O_{40}$ and $Li_3PMo_{12}O_{40}/Li_6P_2W_{18}O_{62}$ combinations were tested. $Li_3PMo_{12}O_{40}/Li_3PW_{12}O_{40}$ showed stable coulombic efficiencies over multiple cycles, but the decreasing state of charge limited the cell performance, dropping to below 20% on the second cycle. $Li_3PMo_{12}O_{40}/Li_6P_2W_{18}O_{62}$ showed a higher state of charge and energy density compared to the previous batteries; however, the decreasing state of charge with cycling remains a limitation to battery performance in these asymmetric systems. Further application to a redox flow configuration is discussed in the next chapter.

4.5 References

[1] Katsoulis, D. E. (1998). A survey of applications of polyoxometalates. *Chemical Reviews, 98*(1), 359-388.

[2] Dubal, D. P., Ayyad, O., Ruiz, V., & Gomez-Romero, P. (2015). Hybrid energy storage: the merging of battery and supercapacitor chemistries. *Chemical Society Reviews, 44*(7), 1777-1790.

[3] Sonoyama, N., Suganuma, Y., Kume, T., & Quan, Z. (2011). Lithium intercalation reaction into the Keggin type polyoxomolybdates. *Journal of Power Sources, 196*(16), 6822-6827.

[4] Wang, H., Hamanaka, S., Nishimoto, Y., Irle, S., Yokoyama, T., Yoshikawa, H., & Awaga, K. (2012). In operando X-ray absorption fine structure studies of polyoxometalate molecular cluster batteries: polyoxometalates as electron sponges. *Journal of the American Chemical Society*, *134*(10), 4918-4924.

[5] Shinkle, A. A. (2013). *Non-Aqueous single-metal redox flow batteries*, Doctoral dissertation, University of Michigan - Ann Arbor.

[6] Doyle, M., Lewittes, M. E., Roelofs, M. G., Perusich, S. A., & Lowrey, R. E. (2001). Relationship between ionic conductivity of perfluorinated ionomeric membranes and nonaqueous solvent properties. *Journal of Membrane Science*, *184*(2), 257-273.

[7] Shin, S. H., Yun, S. H., & Moon, S. H. (2013). A review of current developments in non-aqueous redox flow batteries: characterization of their membranes for design perspective. *RSC Advances, 3*(24), 9095-9116.

[8] Yang, M., Cao, K., Sui, L., Qi, Y., Zhu, J., Waas, A., Arruda, E.M., Kieffer, J., Thouless, M. D. & Kotov, N. A. (2011). Dispersions of aramid nanofibers: a new nanoscale building block. *ACS Nano, 5*(9), 6945-6954.

[9] Cabrera, P. J., Yang, X., Suttil, J. A., Hawthorne, K. L., Brooner, R. E., Sanford, M. S., & Thompson, L. T. (2015). Complexes containing redox noninnocent ligands for symmetric, multielectron transfer nonaqueous redox flow batteries. *J. Phys. Chem. C*, 119 (28), 15882–15889

[10] Tung, S. O., Ho, S., Yang, M., Zhang, R., & Kotov, N. A. (2015). A dendrite-suppressing composite ion conductor from aramid nanofibres. *Nature Communications, 6,* 6152.

[11] Zawodzinski, T. A., Derouin, C., Radzinski, S., Sherman, R. J., Smith, V. T., Springer, T. E., & Gottesfeld, S. (1993). Water uptake by and transport through Nafion® 117 membranes. *Journal of the electrochemical society*, *140*(4), 1041-1047.

[12] Tung, S.O. (2017). Aramid Nanofiber Composites for Energy Storage Applications, Doctoral dissertation. University of Michigan – Ann Arbor.

[13] Su, L., Darling, R. M., Gallagher, K. G., Xie, W., Thelen, J. L., Badel, A. F., Barton, J.L., Cheng, K.J., Balsara, N.P., Moore, J.S. & Brushett, F. R. (2016). An Investigation of the Ionic Conductivity and Species Crossover of Lithiated Nafion 117 in Nonaqueous Electrolytes. *Journal of The Electrochemical Society*, *163*(1), A5253-A5262.

[14] Himeno, S., Takamoto, M., Ueda, T., Santo, R., & Ichimura, A. (2004). Solvation Effect of Li+ on the Voltammetric Properties of [PMo12O40] 3−. Part 2: Comparative Studies on the Preferential Solvation in Acetonitrile+ S and Acetone+ S Mixtures. *Electroanalysis*, *16*(8), 656-660.

[15] Wang, Y., Rogers, E. I., & Compton, R. G. (2010). The measurement of the diffusion coefficients of ferrocene and ferrocenium and their temperature dependence in acetonitrile using double potential step microdisk electrode chronoamperometry. *Journal of Electroanalytical Chemistry*, *648*(1), 15-19.

[16] Tessonnier, J. P., Goubert-Renaudin, S., Alia, S., Yan, Y., & Barteau, M. A. (2012). Structure, stability, and electronic interactions of polyoxometalates on functionalized graphene sheets. *Langmuir*, *29*(1), 393-402.

[17] Pratt, H. D., Hudak, N. S., Fang, X., & Anderson, T. M. (2013). A polyoxometalate flow battery. *Journal of Power Sources*, *236*, 259-264.

[18] Pratt, H. D., Pratt, W. R., Fang, X., Hudak, N. S., & Anderson, T. M. (2014). Mixed-metal, structural, and substitution effects of polyoxometalates on electrochemical behavior in a redox flow battery. *Electrochimica Acta*, *138*, 210-214.

Chapter 5

Polyoxometalate Performance In Non-Aqueous Redox Flow Batteries

5.1 Background and Approach

While some research investigating POM RFBs has appeared in recent years [1-3], surprisingly little attention has been dedicated to this topic. Pratt and Anderson examined several different POMs in either aqueous or non-aqueous media, with $[SiV_3W_9O_{40}]^{7-}$ in an aqueous RFB showing 95% coulombic efficiency in charge/discharge cycling. The POMs in aqueous systems generally exhibited coulombic efficiencies of 50% ~ 95% in charge/discharge tests. However, the use of POMs in non-aqueous systems for RFB applications has not been discussed in detail. The present work examines the performance of POMs in acetonitrile. It builds on previous studies [4,5] of the electrochemical properties of polyoxometalates in acetonitrile.

5.2 Material and Methods

In this work, two different types of flow batteries were used for a comparison in function. The Gen 1 redox flow battery followed the same battery design as in the literature [6]. It was constructed of 316 stainless steel connected with Tygon tubing (Saint-Gobain, 1.6 mm inner diameter) as shown in Figure 5-1. An ANF membrane with 4.63 cm^2 active area was used as separator; two pieces of Goretex tape (0.01inch thick, Gallagher Fluid Seals) were placed on the bare portions of the 316 stainless steel housing between the cathode and anode for electrical isolation, and the pumps (Masterflex L/S Digital Drive) provided a 14 mL/min flow rate. Electrodes were cut from 6 mm thick carbon felt (GFA6, SGL Group) and the charge/discharge experiment was performed with a Maccor Series 4000 battery tester (Maccor, U.S.). The cell was assembled outside the glovebox, and then operated in the glovebox. The catholyte and anolyte reservoirs were both filled with 15 mL of a solution of 0.01 M $Li_3PMo_{12}O_{40}$ with 0.1 M LiTf in acetonitrile that had previously undergone bulk electrolysis to produce an open circuit potential of -0.4 E/V Ag/Ag^+. Before the charge/discharge experiment, the pretreated POM solution was pumped through the system for 1 hour in order to soak the electrode and membrane. During charge/discharge experiments, the current was fixed at 0.9 mA (~0.2 mA/cm^2).

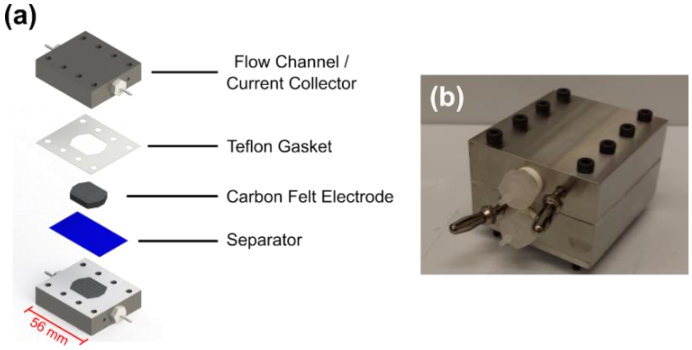

Figure 5-1 Gen 1 316 stainless steel redox flow battery [6]

The Gen 2 redox flow battery used in this work was identical to that previously described in the literature [7], while using the same pumps (Masterflex L/S Digital Drive) and flow rate as the experiments in the Gen 1 redox flow battery. The flow cell was machined from polypropylene for chemical compatibility with ACN. The flow fields were made from 3.18 mm-thick graphite (G347B graphite, MWI, Inc.) and the electrodes were (16.1 mm × 14.1 mm) carbon paper (25 AA, SGL Group). The geometric active area was 2.55 cm and ANF was used as the separator. The two sides of the cell were filled with 5 or 7.5 mL bulk electrolyzed pretreated solution. The Gen 2 redox flow battery schematic is shown in Figure 5-2.

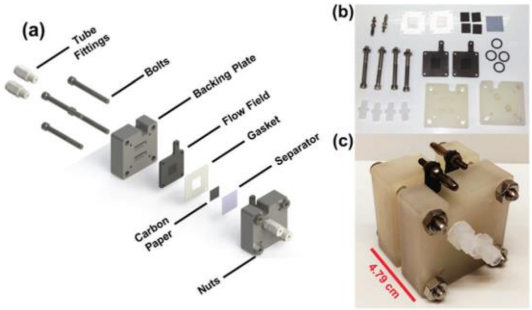

Figure 5-2 Gen 2 redox flow battery [7]

After charge/discharge experiments, the catholyte and anolyte were both diluted to 0.5mM with 0.1M LiTf in acetonitrile and tested with cyclic voltammetry (CV) to examine POM stability. CV experiments were performed at 100mV/s sweep rate, and the data shown in this chapter were obtained for the 5th cycle. CV conditions were the same as section 2.2.2, with a platinum wire auxiliary electrode (MW-4130, BASi) as the counter electrode.

5.3 Symmetric Redox Flow Battery

5.3.1 $Li_3PMo_{12}O_{40}$: Gen 1 Redox Flow Battery Performance

Charge/discharge experiments in the RFB followed the same strategy as static charge/discharge, in which 1-electron charge/discharge cycles were investigated. Results with 0.01M $Li_3PMo_{12}O_{40}$ and 0.1M LiTf in acetonitrile at 50% SoC are shown in Figure 5-3. Performance metrics of 68% columbic efficiency and 40% energy efficiency were obtained at 50% state of charge, which was set as the cut-off. The repetitive pattern of charge/discharge cycles shows the stability of $Li_3PMo_{12}O_{40}$ charge/discharge. The overall potential observed was 0.35 V, which is similar to the H-cell results at a similar current density, 0.2 mA/cm^2. The redox flow battery used has a smaller distance between the electrodes and separator compared to the H-cell. In the flow battery, the electrodes are adjacent to the separator, while in our H-cell the distance is 1.8 cm. The larger the separation, the higher the resistance, and thus the higher the overpotential. The CV results in Figure 5-3c show that the $Li_3PMo_{12}O_{40}$ was intact after the charge/discharge experiment. The 68% coulombic efficiency in the redox flow battery is lower than that in the H-cell (90~95%). This may result from the slow crossover of the POM solution, accompanying small amounts of solvent loss in long-term cycling experiments. Nevertheless, these results show the translation of non-aqueous POM-based electrochemistry examined in static configurations to flow battery operation.

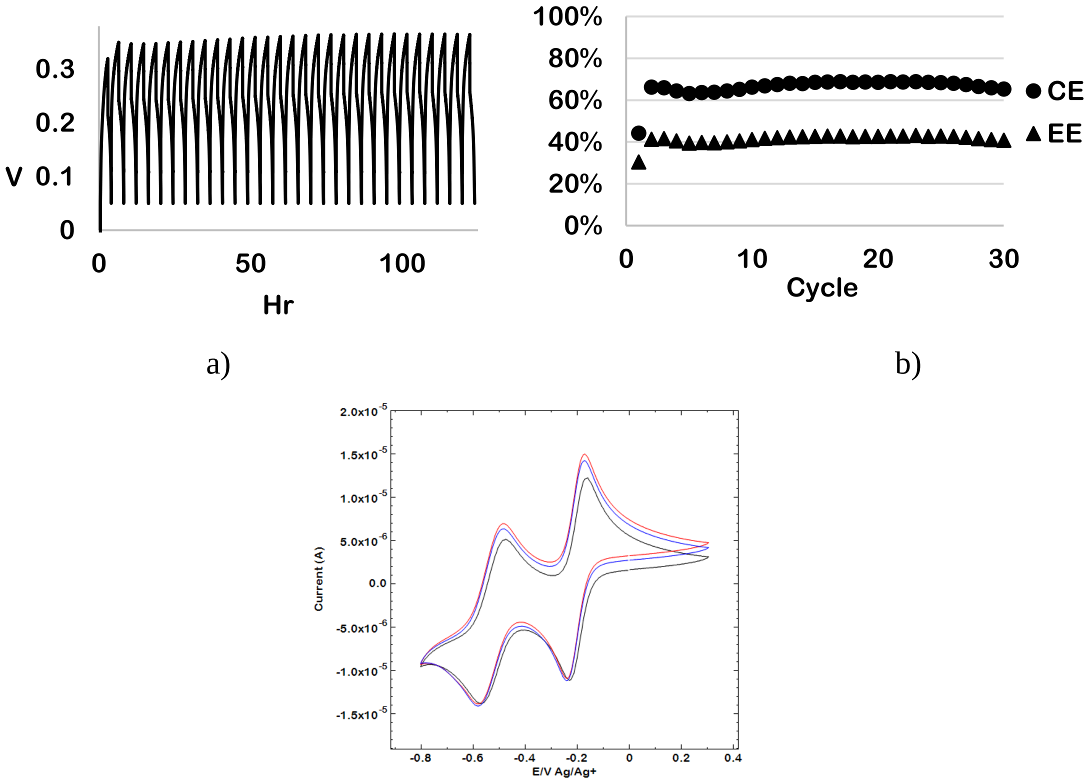

a) b)

c)

Figure 5-3 Redox Flow Battery performance for 30 cycles with the Gen 1 Flow Battery [8] containing 0.01 M $Li_3PMo_{12}O_{40}$ with 0.1 M LiTf. a) 0.2 mA/cm^2 charge/discharge plot, b) coulombic efficiency (CE), energy efficiency (EE) at 50% state of charge at 0.2 mA/cm^2, c) CVs of the POM CD solution diluted to 0.5mM, black: before CD; red: catholyte after CD; blue: anolyte after CD

5.3.2 $Li_3PMo_{12}O_{40}$: Gen 2 Redox Flow Battery Performance

The Gen 2 redox flow battery was tested with 0.01M $Li_3PMo_{12}O_{40}$ and 0.1M LiTf in acetonitrile at 0.2mA/cm^2 current density. Results in Figure 5-4 showed a stable result for 30 cycles. After the charge/discharge experiment, the resistance was measured as 7.28 Ω by EIS. The high (95~99.9%) coulombic efficiency at 80% state of charge showed the stability of the non-aqueous POM RFB. The energy efficiency around 70% also showed better performance compared to the Gen 1 redox flow battery. Analysis of the POMs by CV after the C/D experiment indicated that the POM structure was intact.

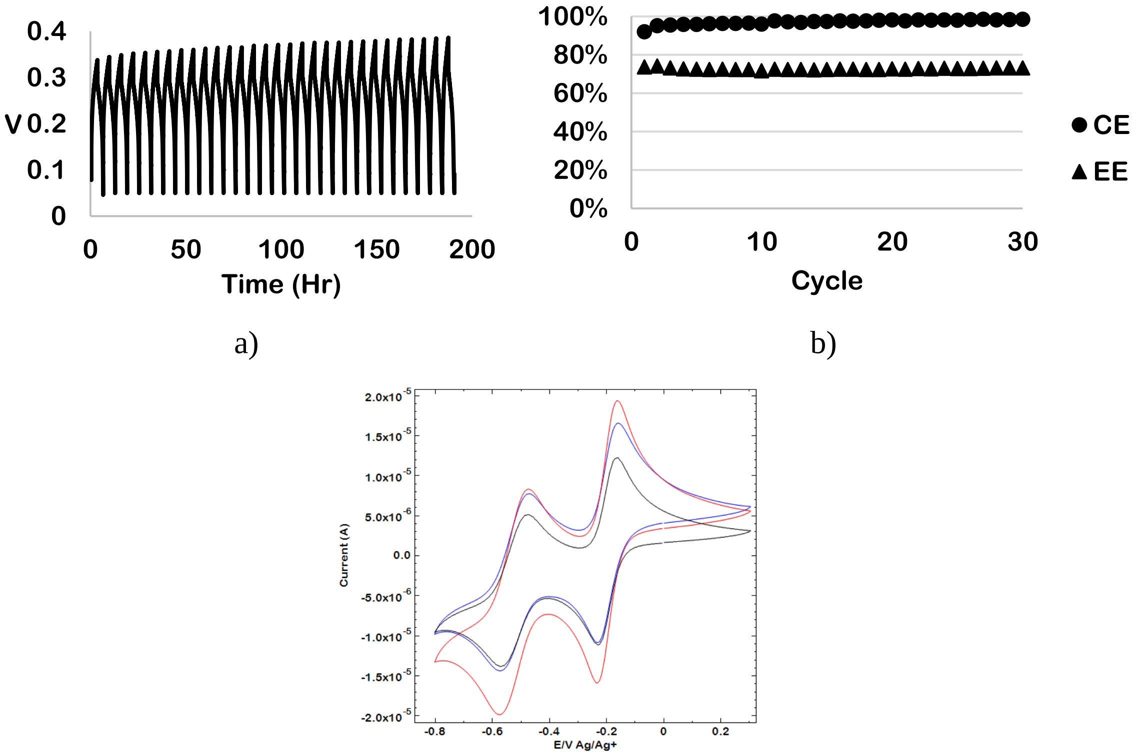

a)

b)

c)

Figure 5-4 Redox Flow Battery performance for 30 cycles with the Gen 2 Flow Battery [8] containing 0.01 M $Li_3PMo_{12}O_{40}$ with 0.1 M LiTf. a) 0.2 mA/cm^2 charge/discharge plot, b) coulombic efficiency (CE), energy efficiency (EE) at 80% state of charge at 0.2 mA/cm^2, c) CVs of the POM CD solution diluted to 0.5mM, black: before CD; red: catholyte after CD; blue: anolyte after CD

5.3.3 Comparison of two different Redox Flow Batteries (Gen 1, Gen 2)

$Li_3PMo_{12}O_{40}$ exhibited stable charge/discharge in both flow batteries. However, the Gen 2 redox flow battery achieved higher coulombic efficiencies (> 90% in Gen 2 RFB and 70% in Gen 1 RFB). Greater crossover or leakage around the membrane may have limited the coulombic efficiency in the Gen 1 RFB. In the Gen 1 RFB, a liquid level difference between catholyte and anolyte reservoirs was observed over time. Similarly, lower efficiencies were reported in previous Gen 1 RFB work [6]. The stainless steel design of the Gen 1 RFB also increases the possibility of an electrical short, unlike Gen 2 which was machined from polypropylene. The lower EE observed with the Gen 1 RFB may also be due the flow field. The Gen 2 has a more compact design of the electrode and the carbon paper, and thus lower resistance arising from the electrolyte conduction path. Therefore, subsequent experiments were carried out with the Gen 2 RFB.

5.3.4 RFB operation at higher POM concentration

To evaluate performance at higher energy densities, higher concentration (0.1 M $Li_3PMo_{12}O_{40}$ with 1 M LiTf) solutions were tested in the Gen 2 RFB. The state of charge in charge/discharge experiments was increased to 80%, and the CD current was increased to 2 mA/cm^2 in order to maintain feasible cycle times. Results in Figure 5-5 showed very high coulombic efficiency (>90%). The energy efficiency (<40%) was lower than that observed for the previous experiment with 0.01 M $Li_3PMo_{12}O_{40}$ (70%). This is likely because the experiment was run at ten times higher current density (2 vs. 0.2 mA/cm^2). The RFB experiment showed stable performance with no significant loss in coulombic efficiency over the course of 30 cycles, in contrast to the limited stability observed during H-cell experiments. One possible explanation may be the low diffusion rate for POMs. The diffusivity of the POM was 10 times lower than that of ferrocene, as discussed in section 4.3.2. While this did not appear to be an issue at lower POM concentrations and currents, at higher POM concentrations and currents diffusivity may have limited POM oxidation and reduction in the longer path-length static cell vs. the much shorter path in the RFB cell. In addition, CV analysis of the anolyte and catholyte after the C/D experiment in the RFB indicated that the POM structure remained intact. Both redox couples in the anolyte and catholyte remained reversible. It is worth noting the 0.1M POM RFB experiment represents the highest concentration POM CD experiment reported to date. This experiment demonstrates a proof-of-concept application of POMs in non-aqueous RFBs, and demonstrates the stability of the POM materials at concentrations higher than previously reported. Since the solubility of $Li_3PMo_{12}O_{40}$ in acetonitrile is nearly an order of magnitude greater than the highest concentration considered here, the opportunity remains to reach higher energy densities by increasing POM concentration. During the first 5 cycles, an increase of CE was observed. Such increases are typically attributed to the “break-in” or formation period of the battery. In this period, the charge/discharge conditions are stabilized and trace impurities may be consumed. Therefore, it took several cycles to reach stable operation. For lower POM concentrations this break-in period was less evident, consistent with its attribution to impurities added with the POMs.

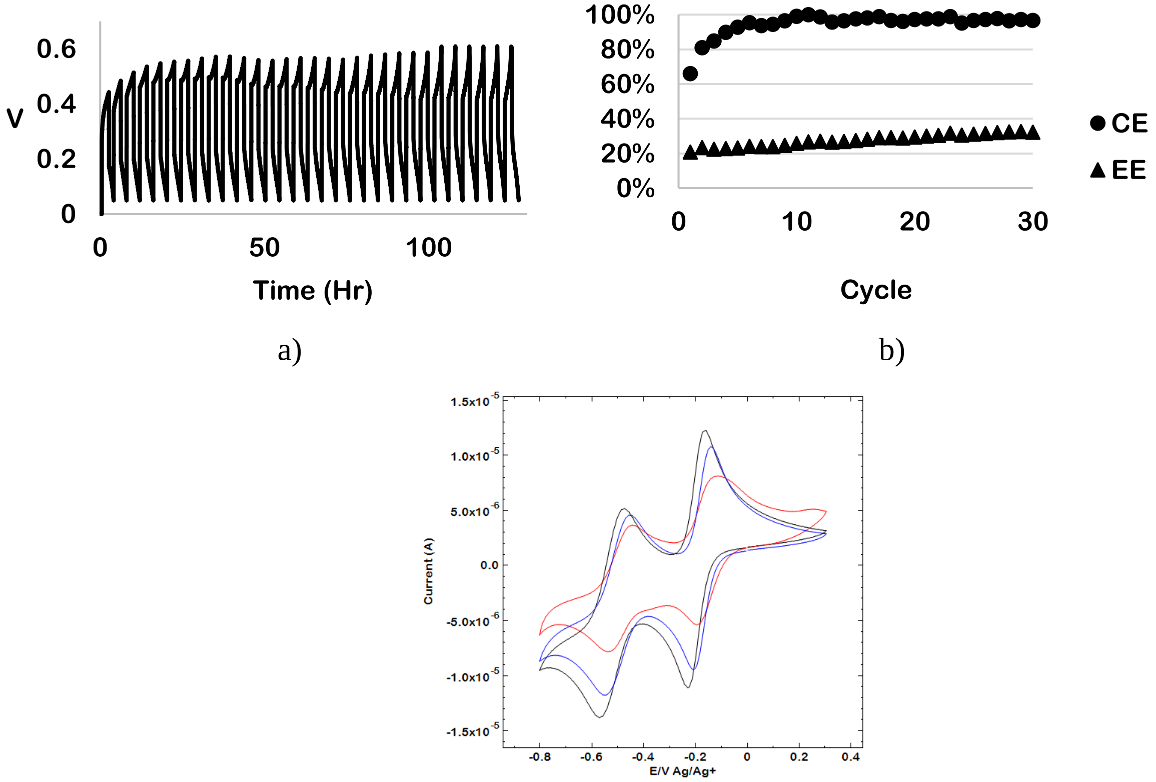

a)

b)

c)

Figure 5-5 Redox Flow Battery performance for 30 cycles with the Gen 2 Flow Battery containing 0.1 M $Li_3PMo_{12}O_{40}$ with 1 M LiTf. a) 2 mA/cm^2 charge/discharge plot, b) coulombic efficiency (CE), energy efficiency (EE) at 80% state of charge at 2 mA/cm^2, c) CVs of the POM CD solution diluted to 0.5mM, black: before CD; red: catholyte after CD; blue: anolyte after CD

5.4 Asymmetric Redox Flow Battery

The performance of an asymmetric RFB with separate $Li_3PMo_{12}O_{40}$ and $Li_6P_2W_{18}O_{62}$ solutions was also examined. Bulk electrolysis was performed prior to charge/discharge cycling experiments. The $Li_6P_2W_{18}O_{62}$ solution was bulk electrolyzed to -0.6 E/V Ag/Ag$^+$ and the couple at -0.85 E/V Ag/Ag$^+$ was used as the anolyte one electron couple. The $Li_3PMo_{12}O_{40}$ solution was bulk electrolyzed to -0.4 E/V Ag/Ag$^+$ for the catholyte, as in the symmetric $Li_3PMo_{12}O_{40}$ charge/discharge experiments.

Operation of an asymmetric RFB with 0.01M $Li_6P_2W_{18}O_{62}$ and $Li_3PMo_{12}O_{40}$ at 50% state of charge was stable for more than 20 cycles, as shown in Figure 5-6. High (95~99.9%) coulombic efficiencies with energy efficiencies around 60% were obtained, demonstrating the feasibility of an asymmetric POM-based RFB. After the charge/discharge experiment, CVs were carried out to examine POM stability, as shown in Figure 5-6d. The catholyte side $Li_3PMo_{12}O_{40}$ remained unchanged, but huge decreases in the characteristic peaks for $Li_6P_2W_{18}O_{62}$ could be seen in the anolyte. This raises stability concerns about the anolyte $Li_6P_2W_{18}O_{62}$.

The static cell crossover test shown in chapter 4.3.1 demonstrated that less than 6% of the POM will cross the membrane over five days, highlighting the resistance to crossover that allows the POM RFB to maintain a high coulombic efficiency. In principle, by increasing the POM concentrations, this asymmetric RFB could achieve higher energy densities, accessing two redox couples for both the anolyte and catholyte, allowing for a 1.3 V cell with two electron transfers.

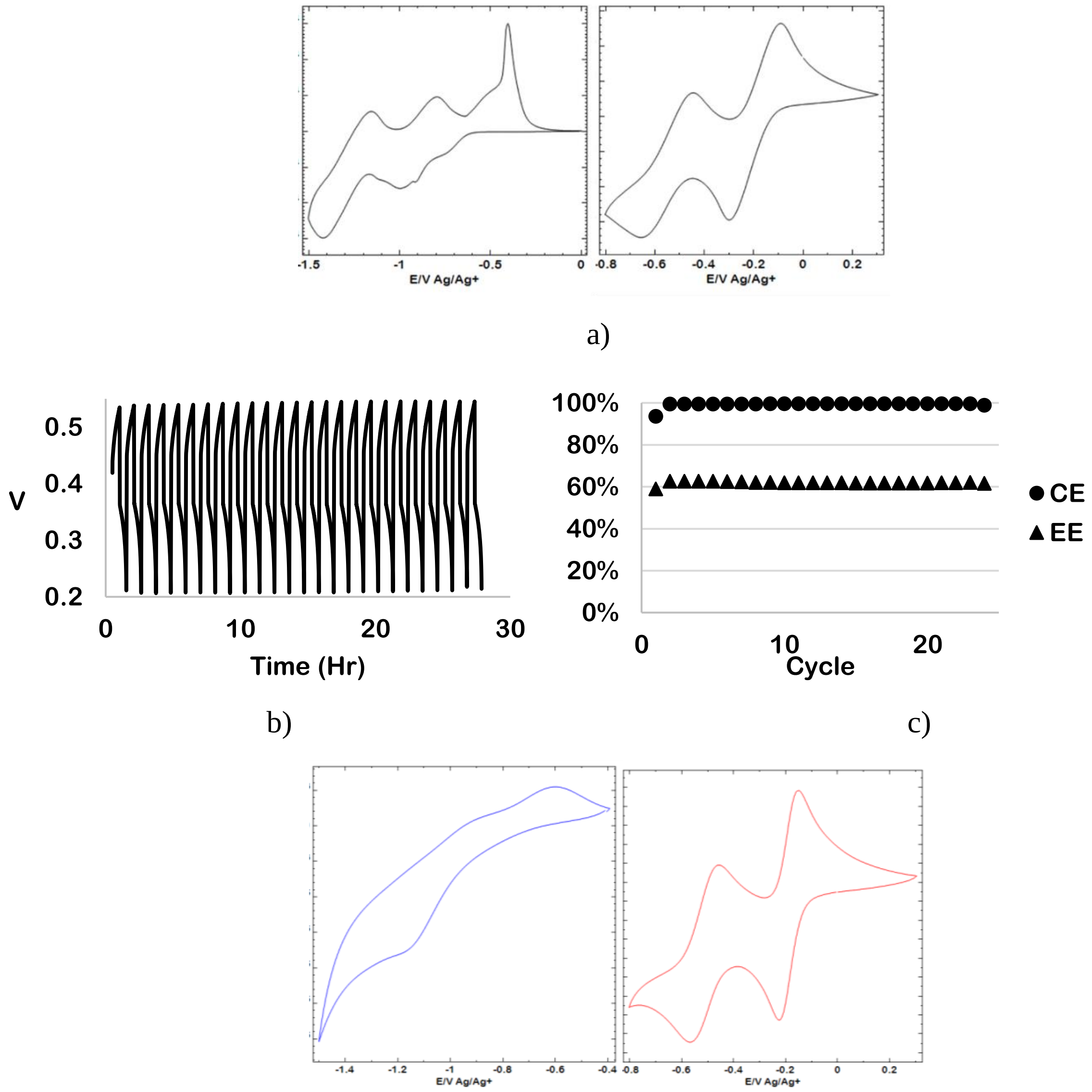

a)

b)

c)

d)

Figure 5-6 Redox Flow Battery performance for 24 cycles with the Gen 2 Flow Battery containing $Li_6P_2W_{18}O_{62}/Li_3PMo_{12}O_{40}$ with 0.1 M LiTf. a) CVs before charge/discharge, 0.01 M $Li_6P_2W_{18}O_{62}$ (left) and $Li_3PMo_{12}O_{40}$ (right) with 0.1 M LiTf in acetonitrile, b) 0.2 mA/cm^2 charge/discharge plot, c) coulombic efficiency (CE), energy efficiency (EE) at 50% state of charge at 0.2 mA/cm^2, d) CVs of the POM CD solutions diluted to 0.5mM, blue: $Li_6P_2W_{18}O_{62}$ anolyte after CD; red: $Li_3PMo_{12}O_{40}$ catholyte after CD

5.5 Conclusions

The experiments performed in this chapter examined POMs as the active materials in non-aqueous RFBs using different RFB cell designs, varying concentrations, and in asymmetric cells to increase energy density. The results showed promising results with the high stability and higher energy designs (higher concentration 0.1M $Li_3PMo_{12}O_{40}$ RFB and asymmetric RFB.) Proceeding from this proof of concept toward more practical operating performance will require accessing a wider voltage window, multiple electron transfers per POM, and higher concentrations, thereby further increasing the accessible energy density with these materials.

5.6 References

[1] Pratt, H. D., Hudak, N. S., Fang, X., & Anderson, T. M. (2013). A polyoxometalate flow battery. *Journal of Power Sources*, *236*, 259-264.

[2] Pratt, H. D., Pratt, W. R., Fang, X., Hudak, N. S., & Anderson, T. M. (2014). Mixed-metal, structural, and substitution effects of polyoxometalates on electrochemical behavior in a redox flow battery. *Electrochimica Acta*, *138*, 210-214.

[3] Pratt III, H. D., & Anderson, T. M. (2013). Mixed addenda polyoxometalate "solutions" for stationary energy storage. *Dalton Transactions*, *42*(44), 15650-15655.

[4] Maeda, K., Himeno, S., Osakai, T., Saito, A., & Hori, T. (1994). A voltammetric study of Keggin-type heteropolymolybdate anions. *Journal of Electroanalytical Chemistry*, *364*(1-2), 149-154.

[5] Chen, J. J. J., & Barteau, M. A. (2016). Electrochemical Properties of Keggin-Structure Polyoxometalates in Acetonitrile: Effects of Countercation, Heteroatom, and Framework Metal Exchange. *Industrial & Engineering Chemistry Research*, *55*(37), 9857-9864.

[6] Laramie, S. M., Milshtein, J. D., Breault, T. M., Brushett, F. R., & Thompson, L. T. (2016). Performance and cost characteristics of multi-electron transfer, common ion exchange non-aqueous redox flow batteries. *Journal of Power Sources*, *327*, 681-692.

[7] Milshtein, J. D., Kaur, A. P., Casselman, M. D., Kowalski, J. A., Modekrutti, S., Zhang, P. L., Attanayake, N.H., Elliott, C.F., Parkin, S.R., Risko, C & Brushett, F. R. (2016). High current density, long duration cycling of soluble organic active species for non-aqueous redox flow batteries. *Energy & Environmental Science*, *9*(11), 3531-3543.

[8] Laramie, S. M., Milshtein, J. D., Breault, T. M., Brushett, F. R., & Thompson, L. T. (2016). Performance and cost characteristics of multi-electron transfer, common ion exchange non-aqueous redox flow batteries. *Journal of Power Sources*, *327*, 681-692.

Chapter 6

Summary, Limitations and Future Work

6.1 Conclusion and Summary

In this work, the polyoxometalate-based non-aqueous redox flow batteries have been demonstrated. The fundamental investigation of Keggin POMs in acetonitrile and the influence of the counter cations, heteroatoms, and frame work transition metal atoms on electrochemical behavior were examined. The principal focus was on the phosphomolybdate, $PMo_{12}O_{40}^{3-}$. The IA and IIA group counter cations (H^+, Li^+, Na^+, K^+, Mg^{2+}, Ca^{2+}) had minor effects on the peak potential and the overall electron transfer processes for cyclic voltammetry experiments in acetonitrile. The solubility of the POM salts decreases down the IA group counter cation column (H^+ to K^+). Therefore, in order to prevent H_2 generation, lithium salts were used in subsequent work. Heteroatom elements considered were P, As, and Si. The P POM and Si POM showed similar CV properties; however, incorporation of Si makes the POM more negative, causing a shift in the position of its first and second redox couples to more negative voltages. This observation mirrors results for Keggin species with different charges in aqueous solution previously reported in the literature [1]. Framework transition metal exchanged POMs were also tested. The Mo, W, and V exchanged POMs showed different electrochemical behavior, which indicated that the framework transition metal had the greatest influence on POM redox properties, as expected. The relationship between the redox behavior of heteropolyacids in aqueous solution and their lithium salts in acetonitrile were compared. The strong correlation between the two suggests that the large library of POM electrochemistry in aqueous solution may provide a guide to POM redox behavior in non-aqueous applications, including redox flow batteries.

Physical and chemical characteristics of POMs were obtained by using solubility measurements, TGA, XRD, FTIR, and bulk electrolysis. $H_3PMo_{12}O_{40}$ showed the highest solubility followed by $Li_3PMo_{12}O_{40}$ among the IA and IIA $PMo_{12}O_{40}^{3-}$ salt. Bulk electrolysis showed the number of electrons transferred in each redox peak couple, as well as providing information about the stability of the reduced POMs. Before charge/discharge tests, membrane crossover tests were performed to aid in membrane selection. Nafion® 117 and ANF both showed high separation ability (low POM crossover), but the Nafion® 117 had a higher resistance in acetonitrile compared to ANF. in static cycling experiments, $Li_3PMo_{12}O_{40}$ showed high coulombic efficiency (~90%) and stability was maintained after 1000 hours of testing. However, the energy efficiency decreased as the charge current increased because of I^2R losses. Additional POMs were also examined via charge/discharge in order to explore opportunities for higher energy efficiency, including both symmetric and asymmetric configurations. For the other POMs examined, the charge/discharge results showed a lower coulombic efficiency or lower state of charge, indicating issues with stability and/or slow kinetics.

$Li_3PMo_{12}O_{40}$ was selected for the symmetric POM redox flow battery (RFB) because of its stability and the high solubility in acetonitrile. The Gen 1 and Gen 2 flow batteries were both tested. The Gen 1 redox flow cell produced a coulombic efficiency of 70%, which is lower than in the H cell test. The reason for the low coulombic efficiency might be due to the crossover between the catholyte and anolyte. For the Gen 2 redox flow cell, a high coulombic efficiency (> 90%) and energy efficiency (> 80%) under a current density of $0.2 mA/cm^2$ were observed. A higher concentration 0.1M $Li_3PMo_{12}O_{40}$ with 1M LiTf were also tested with the current density of $2 mA/cm^2$ selected as the charge rate. The high coulombic efficiency (> 90%) showed that the higher concentration of $Li_3PMo_{12}O_{40}$, which results in a more viscous solution, could still be oxidized and reduced well wiin a flow battery mode compared to the static cell.

Asymmetric charge/discharge experiments were performed with 0.01M $Li_3PMo_{12}O_{40}$ as the catholyte and $Li_6P_2W_{18}O_{62}$ as the anolyte with 0.1M LiTf in acetonitrile. The result showed a high coulombic efficiency (> 90%) and energy efficiency (> 80%) which provides proof of concept for asymmetric POM RFBs, and suggests further strategies for higher energy densities with wider cell voltage ranges.

6.2 Limitations of current work, recommendation, and feasible future work discussion

Previous polyoxometalate redox flow batteries published in the literature [2-4] are compared with other organic redox flow batteries in Figure 6-1. Previous POM RFBs have used concentrations between 10 and 20mM for the prototypes shown as the yellow bar. Green stars shown in Figure 6-1 are the POM RFBs in this dissertation. The differences of the present work compared with the previous POM RFBs include the POM concentration (5 – 100 mM in this work) and the organic solvent for POM RFBs at higher concentrations. More investigations of POM RFBs are still need in order to improve performance. Some POM RFBs have shown high reversibility with high coulombic efficiency (>90%). However, reaching higher energy densittes should be an important goal of future work.

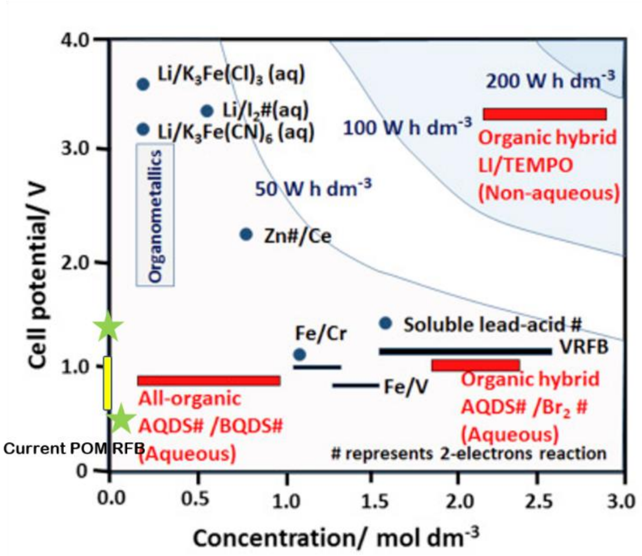

Figure 6-1 Overview of organic redox flow batteries [5] with yellow bar (previously published POM RFBs) and stars (current progress in this dissertation) edited by the dissertation author

6.2.1 Energy Density

As mentioned in the previous chapter, the energy density is proportional to the number of electrons transferred in redox process, the voltage window, and the concentration of the active species.

6.2.1.1 Number of electrons transferred in redox process

Polyoxometalates are known for performing multiple electron redox processes. One approach to achieving higher energy densities is to utilize those that exhibit multiple-electron redox couples. As shown in Chapter 2, the character of the redox couples is most strongly related to the transition metals in the POM framework, suggesting that POMs with different combinations of framework metals may be fruitful. The most common polyoxometalate transition metal elements are Mo, W, and V. In some cases, combinations with other metals have also been reported, e. g., $PMo_{11}M$ (M = Co, Mn, Ni) [6]. Different structures of polyoxometalates also show different patterns of redox process [7,8]. The redox behavior of different POM structures was not discussed in detail in this research.

6.2.1.2 Voltage window of the POM RFBs

Acetonitrile was used in this work because it showed a wider stability voltage window compared to water, so that redox couples beyond the voltage range permitted in water could be examined. For example, it has been shown that $[S_2Mo_{18}O_{62}]^{4-}$ in ACN gives rise to couples over a V range [9]. Beyond structural modification, functional group modification is another possible strategy. The effect of some functional groups on other RFB active species had been studied [10]. For example, functionalized POMs have been investigated for solar cell applications [11] as well as catalysts. By applying functionalized POMs, the energy density of RFBs could be potentially be increased. Functionalized POMs have been studied in a systematic way which were mentioned in the review by Proust et al. [12]. Multiple aspects of hybrid POM, tailor-made hybrid POM, organic–inorganic POM-based hybrid were discussed in the review, and may provide further guidance for selection of POMs for RFB applications.

A key issue with any change of structure, composition, functional groups, etc., is the stability of the POMs under electrochemical cycling. Thus, far stability issues have limited the use of POMs that might otherwise appear to be suitable for battery applications.

6.2.1.3 Solubility of the POMs RFBs

In Chapter 3, the effect of counter cations on POM solubility was shown. For IA and IIA group salts, the solubility decreases as the ion gets larger within the same group. In order to further increase POM solubility, functionalization of the POMs may provide a way to improve the solubility. With other active species such as organics and organometallics, functional groups have been shown to increase active species solubility [10]. While functionalized POMs have been studied previously, there have been few studies of solubility.

6.2.2 Membranes

The membrane is a very active area of investigation, especially for non-aqueous systems. The large size of polyoxometalates (1 nm diameter for the Keggin structure) gives rise low crossover; however, the extent of crossover was around 4% after five days for the ANF membranes in this study. This extent of crossover may be more problematic for asymmetric POM RFBs. Therefore, a smaller pore size membrane is needed for the pore size selection membrane. For example, a different material or more layers in the LBL membrane are some methods on achieving a smaller pore size membrane. More LBL layers could increase the selectivity of the membrane but would increase the resistance of the membrane. Otherwise, a cation selection membrane could be used if the high resistance of the membrane could be solved.

6.2.3 Solvent and support electrolyte

Different solvents have different polarity; for example, water has the highest polarity. Solvent polarity influences the solubility of the solutes. The maximum stable window also varies among different solvents. Additional solvent-related challenges for non-aqueous redox flow batteries are high cost, low conductivity, low solubility, and high viscosity [16]. The supporting electrolyte also needs to be improved. The LiTf conductivity (4 mS/cm) is lower than the common support electrolyte in acetonitrile shown in Figure 6-2 [17], so other kinds of support electrolyte should be considered. Tetraethylammonium (TEA) and tetrabutylammonium (TBA) supports have been shown in Chapter 3 to form low solubility salts with Keggin POMs. $LiBF_4$, $LiPF_6$ or LiTFSI may be feasible as support electrolytes for higher conductivity.

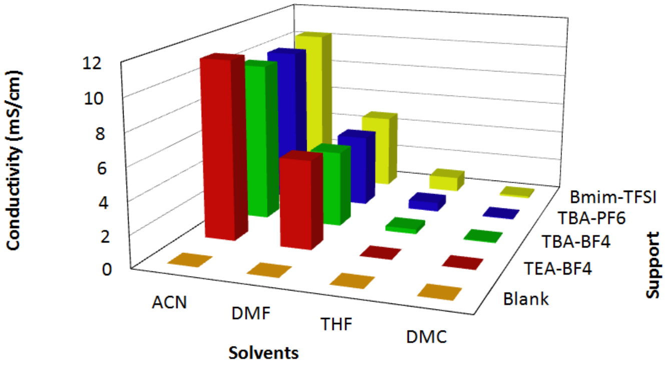

Figure 6-2 0.1M support electrolyte conductivity in different solvents [17]

6.3 References

[1] Sadakane, M., & Steckhan, E. (1998). Electrochemical properties of polyoxometalates as electrocatalysts. *Chemical Reviews*, *98*(1), 219-238.

[2] Pratt, H. D., Hudak, N. S., Fang, X., & Anderson, T. M. (2013). A polyoxometalate flow battery. *Journal of Power Sources*, *236*, 259-264.

[3] Pratt III, H. D., & Anderson, T. M. (2013). Mixed addenda polyoxometalate “solutions” for stationary energy storage. *Dalton Transactions*, *42*(44), 15650-15655.

[4] Pratt, H. D., Pratt, W. R., Fang, X., Hudak, N. S., & Anderson, T. M. (2014). Mixed-metal, structural, and substitution effects of polyoxometalates on electrochemical behavior in a redox flow battery. *Electrochimica Acta*, *138*, 210-214.

[5] Leung, P., Shah, A.A., Sanz, L., Flox, C., Morante, J.R., Xu, Q., Mohamed, M.R., de León, C.P. and Walsh, F.C. (2017). Recent developments in organic redox flow batteries: A critical review. *Journal of Power Sources, 360*, 243-283.

[6] Pathan, S., & Patel, A. (2013). Transition-Metal-Substituted Phosphomolybdates: Catalytic and Kinetic Study for Liquid-Phase Oxidation of Styrene. *Industrial & Engineering Chemistry Research*, *52*(34), 11913-11919.

[7] Keita, B., & Nadjo, L. (1987). New aspects of the electrochemistry of heteropolyacids: part IV. Acidity dependent cyclic voltammetric behaviour of phosphotungstic and silicotungstic heteropolyanions in water and N, N-dimethylformamide. *Journal of electroanalytical chemistry and interfacial electrochemistry*, *227*(1-2), 77-98.

[8] Zhang, J., Bond, A. M., Richardt, P. J., & Wedd, A. G. (2004). Voltammetric Reduction of α-and γ*-[S2W18O62] 4-and α-, β-, and γ-[SiW12O40] 4-: Isomeric Dependence of Reversible Potentials of Polyoxometalate Anions Using Data Obtained by Novel Dissolution and Conventional Solution-Phase Processes. *Inorganic chemistry*, *43*(26), 8263-8271.

[9] Way, D. M., Bond, A. M., & Wedd, A. G. (1997). Multielectron Reduction of α-[S2Mo18O62] 4-in Aprotic and Protic Media: Voltammetric Studies. *Inorganic chemistry*, *36*(13), 2826-2833.

[10] Suttil, J.A., Kucharyson, J.F., Escalante-Garcia, I.L., Cabrera, P.J., James, B.R., Savinell, R.F., Sanford, M.S. and Thompson, L.T. (2015). Metal acetylacetonate complexes for high energy density non-aqueous redox flow batteries. *Journal of Materials Chemistry A*, *3*(15), 7929-7938.

[11] Sang, X.J., Li, J.S., Zhang, L.C., Zhu, Z.M., Chen, W.L., Li, Y.G., Su, Z.M. and Wang, E.B. (2014). Two carboxyethyltin functionalized polyoxometalates for assembly on carbon nanotubes as efficient counter electrode materials in dye-sensitized solar cells. *Chemical Communications*, *50*(93), 14678-14681.

[12] Proust, A., Matt, B., Villanneau, R., Guillemot, G., Gouzerh, P., & Izzet, G. (2012).

Functionalization and post-functionalization: a step towards polyoxometalate-based materials. *Chemical Society Reviews*, *41*(22), 7605-7622.

[13] Sonoyama, N., Suganuma, Y., Kume, T., & Quan, Z. (2011). Lithium intercalation reaction into the Keggin type polyoxomolybdates. *Journal of Power Sources*, *196*(16), 6822-6827.

[14] Müller, A., Peters, F., Pope, M. T., & Gatteschi, D. (1998). Polyoxometalates: very large clusters nanoscale magnets. *Chemical reviews*, *98*(1), 239-272.

[15] Reinoso, S., Dickman, M. H., Matei, M. F., & Kortz, U. (2007). 13-Tungstoborate stabilized by an organostannoxane hexamer. *Inorganic chemistry*, *46*(11), 4383-4385.

[16] Perry, M. L., & Weber, A. Z. (2016). Advanced redox-flow batteries: a perspective. *Journal of The Electrochemical Society*, *163*(1), A5064-A5067.

[17] Shinkle, A. A. (2013). *Non-Aqueous single-metal redox flow batteries*, Doctoral dissertation, University of Michigan - Ann Arbor.